ISTANBUL TECHNICAL UNIVERSITY ★ GRADUATE SCHOOL OF SCIENCE ENGINEERING AND TECHNOLOGY

AERODYNAMIC TOPOLOGY OPTIMIZATION OF A RADOME USING THE GENETIC ALGORITHM

M.Sc. THESIS

İlhanberk DAYLAN

Department of Aeronautics and Astronautics

Aeronautical and Astronautical Engineering Programme

NOVEMBER 2020

ISTANBUL TECHNICAL UNIVERSITY ★ GRADUATE SCHOOL OF SCIENCE ENGINEERING AND TECHNOLOGY

AERODYNAMIC TOPOLOGY OPTIMIZATION OF A RADOME USING THE GENETIC ALGORITHM

M.Sc. THESIS

İlhanberk DAYLAN
(511171157)

Department of Aeronautics and Astronautics

Aeronautical and Astronautical Engineering Programme

Thesis Advisor: Prof. M. Adil YÜKSELEN

NOVEMBER 2020

ISTANBUL TEKNİK ÜNİVERSİTESİ ★ FEN BİLİMLERİ ENSTİTÜSÜ

BİR RADOMUN GENETİK ALGORİTMA İLE AERODİNAMİK TOPOLOJİ OPTİMİZASYONU

YÜKSEK LİSANS TEZİ

İlhanberk DAYLAN
(511171157)

Uçak ve Uzay Mühendisliği Anabilim Dalı

Uçak ve Uzay Mühendisliği Programı

Tez Danışmanı: Prof. Dr. M. Adil YÜKSELEN

NOVEMBER 2020

İlhanberk DAYLAN, a M.Sc. student of ITU Graduate School of Science Engineering and Technology student ID 511171157, successfully defended the thesis/dissertation entitled "AERODYNAMIC TOPOLOGY OPTIMISATION OF A RADOME USING THE GENETIC ALGORITHM", which he prepared after fulfilling the requirements specified in the associated legislations, before the jury whose signatures are below.

Thesis Advisor :	**Prof. Dr. M. Adil YÜKSELEN** İstanbul Technical University	....
Jury Members :	**Prof. Dr. M. Adil YÜKSELEN** Istanbul Technical University	....
	Asst. Prof. Dr. Hayri Acar Istanbul Technical University	....
	Prof. Dr. O. Ergüven Vatandaş İstanbul Gelişim University	....

Date of Submission : 13 November 2020
Date of Defense : 18 November 2020

To my spouse and my family,

FOREWORD

This thesis is prepared as a completion for Aeronautical & Astronautical Engineering Master Program. The motivation of this thesis stemmed from the appetence to get more quick and packaged information for the aerodynamically optimized surfaces. It is believed that, this thesis led to the delivery of necessary tools to an engineer working as Aerodynamic Designer in parallel. This thesis serves a different approach to 3D topology optimization via written, combined codes and co-work operations between the different programs/modules and methods.

While extracting this thesis, there are valuable people who contribute deeply. I would like to thank to these people, because I believe, I could not complete my thesis without their supports. It is surely beyond doubt that, the first helper is my spouse Seda DAYLAN. As another aeronautical engineer of my home, she always tolerated my time allocation with great respect. Of course, my parents and my brother never avoid being spiritual supporters.

There are also important people who do not technically hide their support, first of all is my supervisor Prof. Dr. M. Adil YÜKSELEN. He guided and shed light on my thesis. Also, I would like to express my special thanks to my work mates Tuğcan SELİMHOCAOĞLU and Görkem ATAY.

November 2020 İlhanberk DAYLAN
(Aeronautical Engineer)

TABLE OF CONTENTS

Page

ABBREVIATIONS

AC	: Aircraft
AG	: Adjoint Gradient
AoA	: Angle of Attack
BC	: Boundary Condition
CAD	: Computer-Aided Drafting
CFD	: Computational Fluid Dynamics
CNC	: Computer Numerical Control
CoG	: Center of Gravity
DNS	: Direct Numerical Simulation
ELINT	: Electronic Intelligence
EM	: Electromagnetic
EMC	: Electromagnetic Compatibility
EMI	: Electromagnetic Interference
ERR	: Error
FDM	: Finite Difference Method
FEM	: Finite Element Method
FFF	: Form-Fit-Function
FVM	: Finite Volume Method
GA	: Genetic Algorithm
GM	: Gradient-Based Method
LE	: Leading Edge
LES	: Large Eddy Simulations
LHS	: Left Hand Side
MDO	: Multidisciplinary Optimization
NACA	: National Advisory Committee for Aeronautics
NDI	: Non-Destructive Inspection
NURB	: Non-Uniform Rational B-Splines
OML	: Outside Mold Line
RANS	: Reynold Averaged Navier Stokes Equations
RHS	: Right Hand Side

RTM : Resin Transfer Molding
RWR : Radar Warning Receiver
SA : Simulated Annealing
SATCOM : Satellite Communication
SIGNT : Signal Intelligence
TE : Trailing Edge
USA : United States of America
VBA : Visual Basic
VHF : Very High Frequency
VLM : Vortex Lattice Method

SYMBOLS

A	: Area
AR	: Aspect Ratio
B	: Bernstein Polynomial
$\mathbf{C_D}$, $\mathbf{C_L}$	: Drag and Lift Coefficients
$\mathbf{C_f}$	: Skin Friction Coefficient
Cp	: Pressure Coefficient
D, L	: Drag and Lift Forces
dB	: Decibel
eval	: Evaluation Parameter
$\mathbf{f_x}$, $\mathbf{f_y}$, $\mathbf{f_z}$	: Body Forces
h	: Altitude
H	: Sphere Height
k	: Turbulence Kinetic Energy
$\mathbf{k_1}$, $\mathbf{k_2}$	: Coefficient of Importance
Ma, M	: Mach Number
P	: Pressure
Pa	: Pascal
q	: Source Strength
R	: Sphere Radius
Re	: Reynolds Number
$\mathbf{R_{ij}}$	: Transport Equations
S	: Reference Area
t	: Time
T	: Temperature
u, v, w	: Velocities
$\overline{u}$, $\overline{v}$, $\overline{w}$	: Time-Averaged Velocities
$\mathbf{U_\tau}$	: Velocity (Shear)
$\mathbf{V}$, $\mathbf{V_\infty}$, $\mathbf{U_\infty}$, $\mathbf{U_0}$	: Velocity (Freestream)
W	: Weight
x,y,z	: Coordinates

y	**:** Wall Distance
y^+	**:** Distance Between Wall and First Mesh Node
α	**:** Angle of Attack
γ	**:** Specific Heat
ϵ	**:** Dissipation Rate
μ	**:** Dynamic Viscosity
υ	**:** Kinematic Viscosity
ρ	**:** Density
Γ	**:** Vortex Strength
ϕ	**:** Velocity Potential

LIST OF TABLES

LIST OF FIGURES

Page

AERODYNAMIC TOPOLOGY OPTIMIZATION OF A RADOME USING THE GENETIC ALGORITHM

SUMMARY

Genetic algorithm is one of the ideal ways of topology optimization, especially in the aerodynamic performance area, which is an excellent part of the evolutionary algorithms. In Aerospace Engineering, there are many applications to solve design problems with this method. The genetic algorithm can open up an opportunity to solve complex equation systems or equations that have multi parameters.

From the literature, the general solution usage of a genetic algorithm is the two-dimensional airfoils. However, in this thesis, there is another approach to be able to optimize three-dimensional semi-dome surfaces with two main sections. The sections of the radome also include three lateral guide sections too. These are transmitted to the CATIA V5 program to handle a surface from all generated splines. All these surfaces of each population element are called as Radome. The name is coming from Ra and Dome. Here, while Ra represents the radar equipment, Dome is the cover composite that protects this equipment or unit against environmental influences.

On the other hand, this inside unit volume is regarded carefully and used as a limitation in the genetic algorithm code. Not only the inside unit limitation but also the absurd geometrical detections and size constraints are available in the created custom genetic algorithm code. To perform these limitations, some parameters are accepted as constant or zero. Because they lead to the ribbon and topological errors on the surface. Thus, this is also known that surfaces with these problems are not possible to produce and this makes the problem as multidisciplinary.

In this study, the genetic algorithm code drives the Bernstein Polynomials to get different shapes. After that, their dictionaries show the initial population and the code enables them to show fitness values of them with respect to the defined evaluation criteria. The process of finding fitness values is provided by the values of lift and drag force obtained by the computational fluid dynamics solver. Therefore, the solver must understand the flow condition and the code must serve Reynolds number, velocities and density information, etc. according to the standard atmosphere table and given inputs by the user.

Like the CATIA V5 operation, the ANSA program helps to build the mesh that mostly includes the pyramids and boundary layer tetras. In addition to them, the validation of the solver, viscous model and the boundary layer mesh properties are mentioned as a subject in this thesis. Solver's validation procedure includes the two dimensional, NACA 63-430 airfoil and NACA 63A-015 airfoil verifications in a different angle of attack values to validate c_L, c_D variables. They have similar sections with the general population elements or Radomes, especially in high angle of attack values. Before all analyses were done, the three-dimensional domain and grid convergence study are performed; their results are given in the related section. Hence, many grid parameters of the solution are fixed.

After defining the fitness values, crossover and mutation operations are carried out per previously defined and elected parents. These parents are mutated randomly and the crossover operation has proceeded for all. If this part is regenerated as many times, the

fitness values are going to be desired value over iterations. In this way, the final results comprise of the parents of the last fitness values.

In conclusion, when the genetic algorithm is compared in terms of efficiency, the time to find the right result can be slower than other methods. But as a feature added to this method, the method has removed all unnecessary population elements and again remove all elements that intersect with the volume of the inside unit from the solution set along with the screening properties. For this reason, the number of analyses performed was minimized and the analyses' time was considerably shortened and controlled. With all these modifications, the genetic algorithm code has been turned into a useful one, unlike other standard genetic algorithm programs. At the same time, the code had the opportunity to examine the solution range in a certain part by eliminating many parameters within the scope of the genetic algorithm and this code offers a parallel computing option with Fluent solver, which provides an additional speed to the modified genetic algorithm code infrastructure.

BİR RADOMUN GENETİK ALGORİTMA İLE AERODİNAMİK TOPOLOJİ OPTİMİZASYONU

ÖZET

Evrimsel algoritmaların en yaygın türü olan genetik algoritma, özellikle aerodinamik performans alanında topoloji optimizasyonunun klasik yollarından biridir. Evrimsel algoritmaların büyük bir kısmı bu yöntemi farklı amaçlarda kullanmaktadır. Örnek olarak Havacılık ve Uzay Mühendisliği'nde, tasarım yöntemlerini bu yöntemle çözmek için birçok uygulama göze çarpmaktadır. Genetik algoritma, karmaşık denklem sistemlerini veya çoklu parametrelere sahip denklemleri çözmek için bir fırsat niteliğindedir ve popülerliğini yitirmiş olmasından sonra artan bilgisayar hızlarıyla yeniden çok fazla araştırmada ve çalışmalarda gündeme gelmiştir.

Literatürden elde edinilen bilgilere göre, genetik algoritmanın genel çözüm kullanımı iki boyutlu kanat profilleridir. Bununla birlikte, bu tezde üç boyutlu yarı kubbe yüzeylerini iki ana kesitte optimize edebilmek için başka bir yaklaşıma gidilmiştir. Radomun bölümleri ayrıca üç adet yan kılavuz kesitlerini de içerir. Bunlar üretilen tüm eğrilerden bir yüzeyi oluşturmak için CATIA V5 programına iletilir. Her popülasyon elemanının tüm bu yüzeylerine, Radom denir. Adı temel olarak Ra ve Dome kelimelerinden gelmektedir. Burada Ra, radar ekipmanını temsil ederken, Dome bu ekipmanı veya birimi çevresel etkilere karşı koruyan kompozit kapaktır.

Öte yandan, bu iç birim hacmi önemle dikkate alınır ve genetik algoritma kodunda bir sınırlama olarak kullanılmaktadır. Oluşturulan genetik algoritma kodunda sadece iç birimden gelen sınırlamalar değil, aynı zamanda uygunsuz geometrik tespitler ve boyut kısıtlamaları da mevcuttur. Bu sınırlamaları gerçekleştirmek için bazı parametreler sabit veya sıfır olarak kabul edilmektedir. Çünkü bu detayların farklı değerlerde, yüzeyde şerit şeklinde hatalara ve topolojik açıdan problemlere yol açacağı ortadadır. Bu nedenle, bu problemlere sahip yüzeylerin üretilmesinin mümkün olmadığı da bilinmektedir ve bu da problemi çok disiplinli bir noktaya ulaştırır.

Bu çalışmada, genetik algoritma kodu, Bernstein Polinomlarını kullanarak farklı şekiller elde etmeyi sağlar. Şekil oluşumu sonrası, populasyon ortaya çıkmış olur ve kod, tanımlanan değerlendirme kriterlerine göre bunların uygunluk değerlerini göstermeyi sağlar. Uygunluk değerlerini bulma işlemi, hesaplamalı akışkanlar dinamiği çözücüsü tarafından elde edilen kaldırma kuvveti ve sürükleme kuvveti değerleri ile sağlanır. Bu nedenle, yazılan kod akış koşulunu anlamalı ve bu kod, standart atmosfer tablosuna ve kullanıcı tarafından verilen girdilere göre Reynolds sayısı, hızları ve yoğunluk bilgileri vb. çözücüye sunmalıdır.

CATIA V5 programı üzerinden yapılan işleme benzer bir şekilde, ANSA programı da çoğunlukla piramit şeklindeki ağları ve sınır tabakası tetralarını içeren ağın oluşturulmasına yardımcı olur. Ağ yapısına ait kontroller ve kalitesi uygun olmayan elemanların kontrolü ANSA tarafından yazılan script vasıtasıyla yapılır. Uygun olmayan elemanların silinip, yerine yenisinin düzeltilmiş olarak uygulanması 3 boyuttaki ağ yapısında sağlanır. Nihai durumda ise ağ yapısının son hali msh dosyası olarak çözücü ANSYS Fluent programına otomatik olarak iletilmiş olur. Bunlara ek olarak çözücü, viskoz model ve sınır tabakası ağ özelliklerinin doğrulanması işlemi de bu tezde bir konu olarak belirtilmiştir. Çözücünün tasdiklenmesi prosedürü, farklı hücum açısı değerlerinde iki boyutlu, NACA 63-430 kanat profili ve NACA 63A-015 kanat profili yapılarını, c_L ve c_D değerlerini doğrulama aşamasında gerçekleştirilir ve

özellikle yüksek hücum açısındaki kesitleri radomların genel popülasyonunda yer alan elemanları veya buradaki radomlar ile benzer kesit yapısına sahiptir. Tüm analizler yapılmadan önce üç boyutlu çözüm hacmi ve çözüm ağı yakınsaması işlemi gerçekleştirilir, sonuçları bu tez içerisinde ilgili bölümde yer almaktadır. Böylece çözüme ait pek çok parametre belirlenmiş olur.

Uygunluk değerlerinin tanımlanmasından sonra, daha önce tanımlanmış ve seçilmiş ebeveynler başına çaprazlama ve mutasyon işlemleri gerçekleştirilir. Bu ebeveynler rastgele mutasyona uğrar ve tümü için çapraz operasyona devam edilir. Eğer bu kısım defalarca yeniden tekrarlanırsa, uygunluk değerleri iterasyonlar üzerinden istenen değere ulaşabilecektir. Böylece nihai sonuçlar, son uygunluk değerlerinin ebeveynlerinden oluşur. Buradaki çalışma kapsamında gerekli parametrelerin değiştirilerek veya modifiye edilerek çaprazlama vasıtasıyla farklı genetik yapıdaki bireylerin oluşturulması sağlanmış olur. Her iterasyon için farklı jenerasyonların en iyi bireylerine aerodinamik analizler ve gerekli geometrik eleme alt işlemleriyle ulaşılması hedeflenmiştir. Globalde ve gerçek anlamda en geniş arama kümesine sahip olmak için uygun mutasyon oranında bir katkı daha gerekli olmaktadır. Bu oranın bulunması için duruma özel denemeler ve tıpkı algoritma tipinin belirlenmesi gibi çeşitli literatür çalışmalarından geniş oranda yararlanma ihtiyacı duyulmuştur. Tüm bu gerekliliklerin, olayın bütünü düşünülerek sağlanması her amaç fonskiyonu kapsamında Python kodu tarafından sağlanmaktadır. Her bir aşamadaki her bireye ait çözümdeki programların açılıp kapatılması ve gerekli bilginin yazılması da yine bu kod yapısı tarafından her aşamada kontrol edilmektedir.

Nihai olarak, genetik algoritma verimlilik açısından karşılaştırıldığında, doğru sonucu bulma süresi diğer yöntemlerden daha yavaş olabilir. Günümüzdeki bilgisayarların hızlı oluşu ve daha da hızlı olmasına yönelik eğilimlerin bir sonucu olarak bu yöntemin kullanımının gelecek yıllarda hiç olmadığı kadar çok olacağı beklenmektedir. Günümüzde bu uzun süredeki çözüm arayışına ek olarak bu yönteme eklenen bir özellik ile yöntem, tüm gereksiz popülasyon elemanlarını ve iç birimin hacmiyle kesişen tüm unsurları, tarama özellikleriyle birlikte çözelti kümesinden çıkarmıştır. Bu nedenle, gerçekleştirilen analizlerin sayısı en aza indirilmiş ve analizlerin süresi önemli ölçüde kısaltılmış ve kontrol edilmiştir. Tüm bu değişikliklerle, genetik algoritma kodu diğerlerinden farklı olarak kullanışlı bir kod haline getirilmiş olur. Aynı zamanda, kod genetik algoritma kapsamında birçok parametreyi ortadan kaldırarak çözüm aralığını belirli bir bölümde inceleme fırsatı bulmuş olur ve yine bu kod ANSYS Fluent çözücüsü içerisinde paralel hesaplama seçeneği sunar ki bu da modifiye edilmiş genetik algoritma kod altapısında hızlandırıcı bir etki sağlar.

Yapı olarak bir bütün olarak hazırlanan kod sistemi, tüm bu aktarılan işlemlerin sırasıyla gerçekleştirilip uygun ebeveynlerin sağlanmadığı durumda kullanıcıyı uyaracak ve otomatik olarak çözümlerin durmasını sağlayacaktır. Bu aşama sadece genetik algoritmanın ilk iterasyonuna ait olacağı için bu kısımda zaman kaybı açısından kullanıcıya minimum kayıp yaratacak bir örgü oluşturulması hedeflenmiştir. Tüm bu çözüm sistemi iki farklı koşulda denenmiş ve sonuçları bu tez kapsamında aktarılmıştır. İlk koşulda görülmek istenen detay çözüm süreleri (maksimum küme boyutları kaynaklı) ve kullanıcı tarafından sağlanan sınırlı alanın düzgün bir şekilde verimli olarak kullanılıp kullanılmadığının kontrolüdür. Bu koşul kaldırma kuvveti katsayısının sürüklemeye olan oranının maksimum tutulduğu koşuldur. Diğer koşulda ise her iki değerin de minize edilmesi istenecektir. Beklenen şekil ilk koşul için kesiti kanat profilini andıran, yüksek c_L değerine sahip ve düşük c_D değerine sahip yayvan, silindiri oldukça sıkı kapsayan bir geometridir. Diğerinde ise bu şekilde gerçek optimizasyon ihtiyacı ortaya koyulmuş ve her iki koşulun da minimize edilmesi ile hatchback bir arabanın görünüşünü andıran arkası daha keskin ve ani bitişe sahip ilkine göre daha oval yapıdaki bir geometri olacaktır ve nitekim bu geometrilerin elde edilmesi sonuç kımında belirtildiği gibi sağlanmış olur.

1. INTRODUCTION

Today, aerospace companies developing products for aviation are spreading their projects more planned and for longer periods, and they have to overlook the additional costs of all these conditions. The most important reason for this is that this sector, which directly affects human life, needs works that are carried out with more care and attention day by day. Besides, research and development activities that will prevent increasing costs and periods are actively carried out by the engineers, an example of this can be seen in this thesis. In this context, projects in the aviation industry are divided into certain titles within a planned system and studies are carried out within this scope.

While the same is right for aviation radomes, some conditions for these protective elements are examined more carefully. From these conditions, the title of aerodynamic effects is discussed in this thesis and in accordance with the development layout given in Figure 1.1, a faster and unmanned version of this system is tried to be created. In the system created here, at the first stage, a project based on different ideas and demands is put forward. The following steps were platform inspection activities, with the provision of a system and design requirements like red labeled in Figure 1.1. In parallel, researches for similar studies are considered and the technological level of the company plays an important role in the structuring of the final product at this point.

When all these studies are carried out, the obtained concept designs are eliminated with several analyses, test studies and design items by the contribution of the customer feedbacks, and with these steps, the conceptual design phase will be passed. However, it is a very time-consuming process for these steps to reach a detailed design phase. The detailed design, which undergoes many iterations and suitable products according to the test and analysis results, becomes apparent after all these processes. Later on, production activities and deliveries are provided.

In this thesis, which mainly covers analysis processes, decision making and design phases, some parameters coming from the new ideas and project demands are accepted as input values of the problem. And, preliminary design product is obtained as output after intermediate processes that lead to product formation. These details are included in Section 1.3.

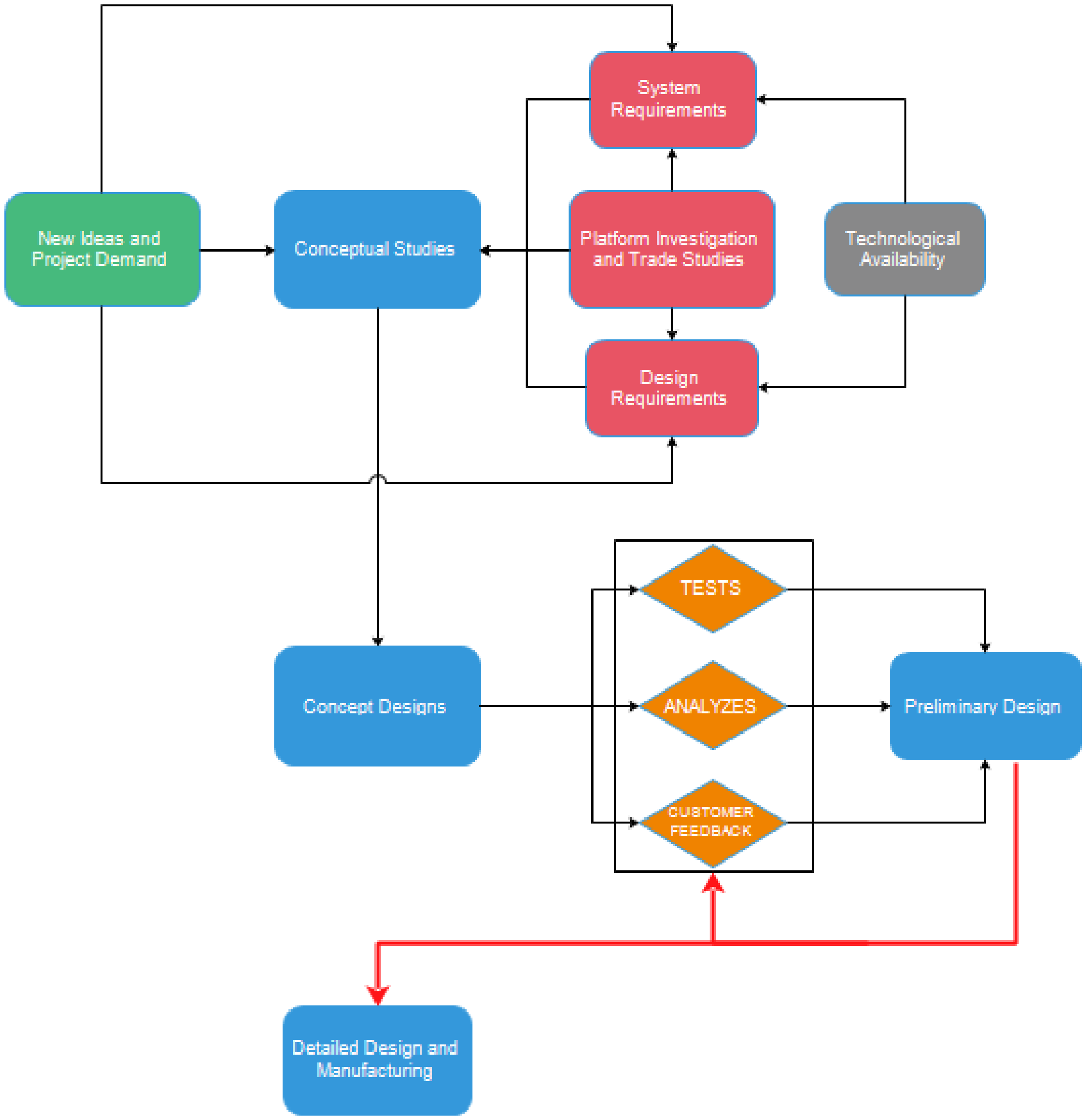

Figure 1.1 : Aerospace Product Development Layout.

The starting point of this study is undoubtedly the need to reveal a 3D surface that can yield the closest results to the desired behavior under specific aerodynamic conditions. Certain methods are followed to meet these requirements. In the literature, these methods are used for various purposes, but in this thesis, the behavior of the methods was examined by modifying an existing algorithm in Python for this specific purpose and a unique 3D Radome structure was obtained under the desired condition by passing through this modified optimization process.

In this section, it is planned to give information about the conditions related to the radomes integrated on the aircraft, which stages are applied while the production and design processes are going on.

1.1 Aircraft Radomes

At the beginning of the Second World War, aircrafts carried VHF radars and various antennas without protective structures such as radome on them. Increasing air vehicle speeds enforced cover the antenna or radar equipment from the physical environment with radomes. In 1940, the first microwave radar was produced in the USA. After a little while, the first radome is used in B-18 aircraft as a nose radome in a missile-like structure under the wing. (Kozakoff, 2010)

Radomes act as protectors not only for electronic equipment but also for the mechanical support parts inside. However, the position of the aircraft radomes on the aircraft is determined according to the EMI/EMC problems, operability conditions of the equipment integrated on it, aerodynamics, stability, vibration effects and bird striking conditions on the aircraft.

Stability and Aerodynamic effects are expressed as follows and closely related to the thesis subject; the aerodynamic behavior of the air vehicle is changed by the additional forces that come from the radome structure as known. Therefore, the lift, drag and moment coefficients are determinant for this situation and the shape of the radome surface is of great importance in determining the aerodynamic coefficients. At the same time, radomes must survive under specific environmental conditions such as rain, snow, dust and salty water (especially for maritime patrol aircraft) that are defined in certain aerospace standards.

The expectations from the properly designed radomes are listed in general form; (Table 1.1) (L3HARRIS, n.d.)

Table 1.1 Perfectly Designed Radomes and Effects of Them.

Area of Study	Effects (+ve)
EM	Improving Functional Capability and Accuracy
EM/Heating	Reducing the Downtime of the Equipment
EM	High Field of View Design (Sensor or Antenna)
EM	Preventing the EMI/EMC Problems
Structural	Increasing Fatigue Life and Component Strength with Minimum Weight
Structural	Low probability of the debris impact (i.e., Bird Strike Results)
Structural	Easy Inspectable and Repairable Design
Structural/Electrical Resistance	Lightning and Anti-Static Protection
Aero	Low Contribution to the Load Distribution
Stability	Low Moment Changes Around the AC
Assembly	Interchangeability and Available Design Space
Assembly/Structural	Properly Defined Structural Bolt/Screw or Bonding Interfaces

As an example of radome found on almost all aircrafts, weather radars can be shown. These radomes are often located on the nose of the aircraft, and the most critical problems of them are bird strikes and lightning strike problems. To prevent lightning effects, a connection to a metal area is created over these radomes with lightning strips. On the other hand, the effect of the bird strike example of Boeing 737-800 aircraft's nose cone is demonstrated in Figure 1.2. Here also, the lightning strips that reach to frames can be distinguished at the sides of the radome.

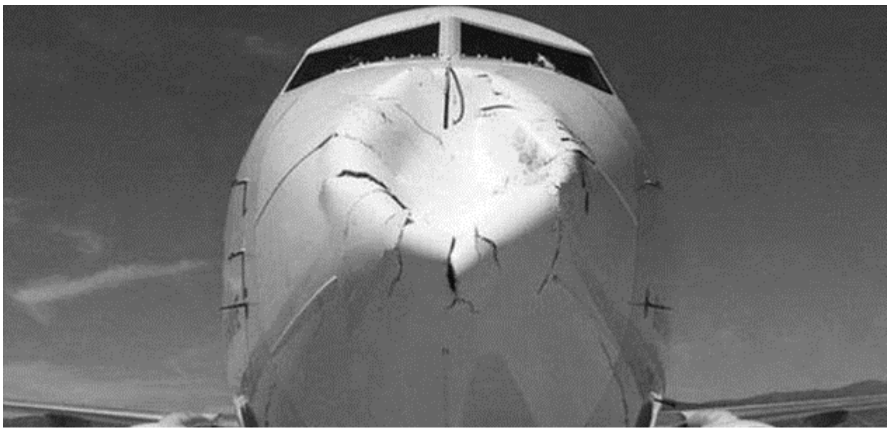

Figure 1.2 : Nose Radome Damage, Flight TK2004 (Flight-Report, 2015).

Apart from the basic radomes, ELINT, RWR, SATCOM and SIGNT radomes are integrated for special functions. Figure 1.3 illustrates the example of the radome that is strengthened by the metal brackets and skirts.

Figure 1.3 : Radome Allocation Example Near the Empennage (Plassard & Abdulhamid, 2017).

Due to the adverse effects of the metal outer skin of aircraft on the electronic equipment, they must be located on the outer placement of aircraft generally. Thus, mostly, the glass fiber reinforced composite radome structures are used as the cover of these electronic devices or equipment.

As the most suitable electromagnetic material, composites have strong capabilities in structural mechanics and electromagnetic transmittance. For instance, strength to weight ratio (specific strength) of the glass fiber reinforced composite radomes are generally double time better than the aluminum assemblies. The composite structures are more invulnerable than the metals too, the impact strength is one of the most important parameters for radomes and these can explain the heavy usage of the composites as a radome material. One other dominant feature is about the corrosion; composite materials also promise a much longer life in terms of the corrosion.

On the other hand, the use of the surface protector and filler materials are common in this industry because of the handling the radome parts with minimum surface roughness. These materials can easily fill the small dents and pit areas. Anti-static coating, primary paint, waterproof sheets and final paints are also applied outside of the radome surface against corrosion and sealing problems.

All these requirements need planned efforts for the design and maintenance of the radomes. Here, the design phases and manufacturing operations of the radomes are summarized in subsections.

1.1.1 Design phases

The design processes of the radomes are examined in three stages, up to the production stage. The first is to reveal the concept design of the radome, just like airplane design. In this conceptual design phase, there are successive analysis processes and characterization processes in addition to the basic design. The aim is to present a radome per certain aviation rules and to present it with the mission. It is the second stage that requires the longest time and cost, which is a big part of the research and development side of the design phase. Finally, the last process is the preparation of the detailed design of the radome, with the well-determined boundaries and identifying conditions of the radome appropriately. While the work cluster in the thesis aims to bring together the works of these second and last stages, it also aims to reveal an optimization algorithm that can fulfill the requirements for production easily. The requirement constraints of the radomes are consists of the aerodynamic and structural issues. Therefore, this multidisciplinary area is split into the design and aerodynamic phases from the beginning of this cluster.

When revealing the concept design of a radome, it is a priority to turn to the problem with three design perspectives and all these are called interchangeability rules of the design. (Peterman, 2011) The radome to be integrated must meet the Form-Fit-Function (FFF) requirements. This section is an issue for designers that must be followed in new part designs or revisions. Here, the Form describes the shape, CoG, mass properties and visual character of the component including the aerodynamic shapes of them, the Fit is related with the connection type and integration location, the physical interface is the most important notion for the Fit term like the boundary effect of that interface on aerodynamic loads. For example, consider a radome structure, the Fit term is associated with the defining and controlling the surface roughness tolerance to ensure proper assembly with the skirt parts. The last term, Function, is about all the actions to conduct the installation aim or task of the part in the whole product.

Therefore, these design concepts have to be examined into both structural, aerodynamic and electromagnetic topics.

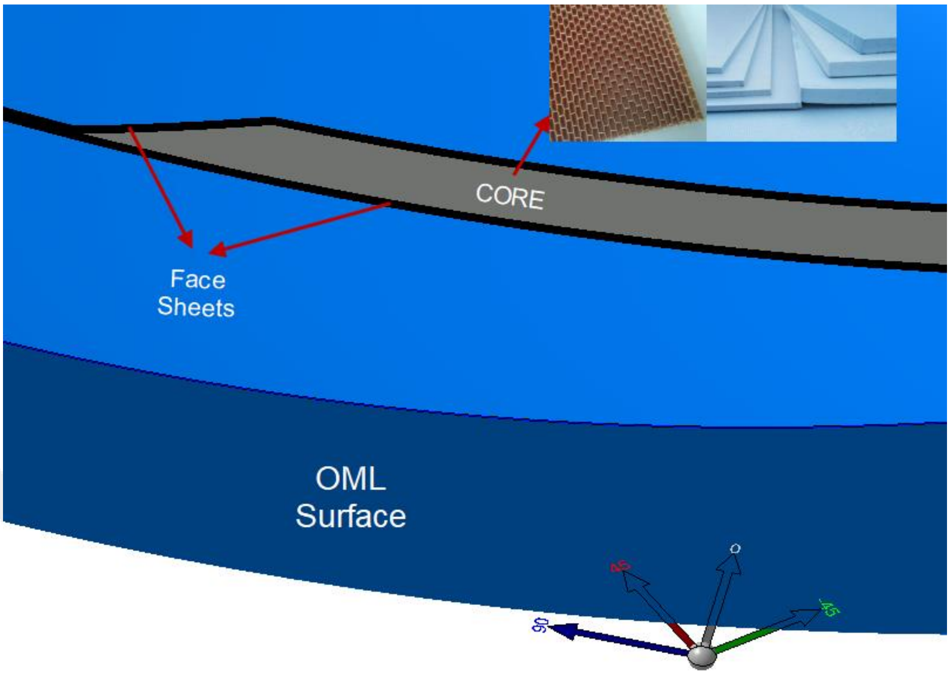

Figure 1.4 : Design Model Example For A Composite Radome.

The most important contribution in composite Radome structures to be electromagnetically and structurally useful comes from the core materials. (Figure 1.4) (Maria, 2016) These materials are chosen from polymeric honeycomb products such as aramid or special foam materials, reducing electromagnetic dB losses and providing structural strength in the direction of compression without making the radome structure too heavy. The link between the aerodynamic shape production can be established on the thickness change because increasing the thickness value can cause different results in aerodynamic coefficients. Therefore, there will be a comfy clearance parameter in code structure when the offset margins are already imagined.

After determining the aerodynamic shell geometry, composite detail design of radome structures is determined by CAD tools. This design has two purposes. The first is to create a detailed nesting model that will be used by static structural analyses, and the other is to create cut pieces and flatten geometries in a CAD model to be used in manufacturing processes that produced radomes rely on that processes can give well manufactured or surfaces without defects or incidentally occurred delaminations.

1.1.2 Manufacturing basics

The radome structure, which is planned to be integrated, is transferred to the production stage after it passes the design stages and after the documentations of them are prepared. Unlike metal parts, the production of composite parts requires complex design models, high cost and mold production. Molds contain different materials depending on the number of composite materials to be produced and surface quality, after the removal of the model structures produced by CNC machining before the mold production process. By using this model structure, the mold that will be produced by using composite materials in the same fiber-matrix structure as the radome will not behave differently from the real part production in terms of thermal expansion, so the product is obtained with higher quality.

Figure 1.5 : Carbon Composite Radome Mould.

Also, adding a flexible material between the carcass structure is made of steel or carbon composite and the mold or making carcass directly from the mold material is an important measure to prevent scraps that may occur during the curing process. (Figure 1.5)

Just like the other composites, composite productions of the radome parts can be done by hand lay-up, automatic fiber placement and RTM methods. These methods are determined by evaluations of items such as surface quality, electromagnetic requirements and cost.

For the most commonly used, hand lay-up method and RTM, ready-made resin-impregnated prepreg structures are used very often. The types of these materials commonly used in aircraft radomes are fabric type prepregs rather than the unidirectional ones. The most important reason for this is that fabric prepregs have a bi-directional fiber structure and their lay-up process is straightforward because of the drapability of them when compared with unidirectional prepregs. Another important reason comes from its mechanical strengths; these materials are advantageous products for complex and oval surfaces such as radome since they have similar strengths in warp and weft directions.

A few methods can be applied to facilitate hand-layup productions during the realization of the production from the prepared mold. Draping with the laser method is one of these methods and makes an important contribution to the operator to put the correct piece to the correct area in a short time. (Figure 1.6)

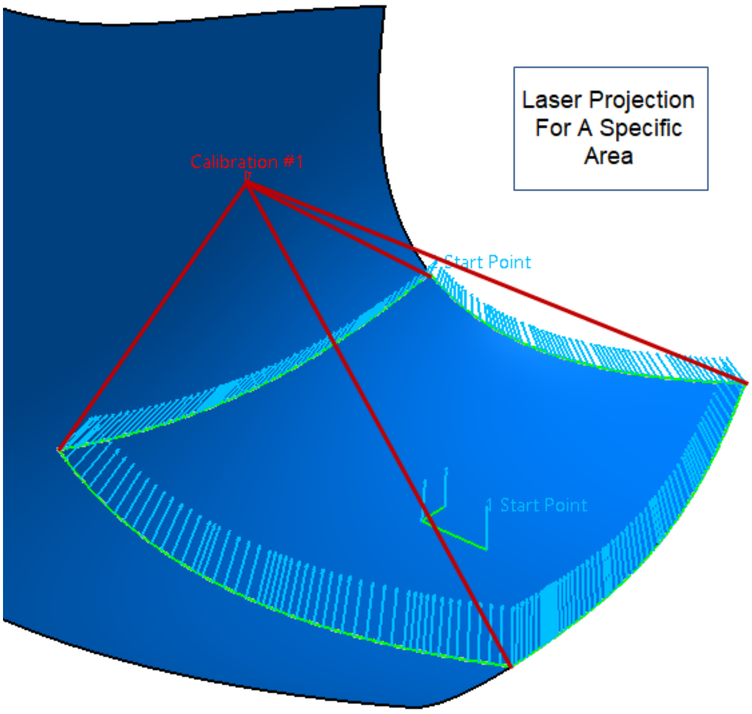

Figure 1.6 : Laser Projection Operation of a Sample Cut Piece.

The cured and produced parts are subjected to quality processes in terms of whether they meet the current technical requirements or not. Composite radomes, which pass the quality processes successfully, become ready for integration following the assembly documents. The NDI methods are applied for in-service damage investigation and the methods vary according to the structure types of composite, for a sandwich structure, tap test can be applied for the understanding of the delamination locations or foreign object detection if there exists. But more complicated techniques are applied to solid laminate parts and are named as A, C scan testing. Also, the in-process tests are applied for examining the stiffness reductions or other negative structural effects from the manufacturing operations.

1.1.3 Aerodynamic concept and requirements

The development of the surface shapes of composite radomes in the design process is mainly based on the aerodynamic and stability effects on the aircraft body. Unless specific constraints are specified structurally and electromagnetically, a minimum contribution to lift and drag forces is usually expected for integrated radome. For example, for a standard cargo plane in the conventional wing and tail structure, as the integration zone moves away from the wing aerodynamic center, the lift force generated by the radome structure around this line, causes undesired moment changes and effects the stability of the aircraft in cruise flight of the aircraft. Because, this object is remarkable for the thesis context with the moment effect. However, the moment contribution is not attached to the results, because the modified algorithm is aimed to work with multiple cases in a coordinated manner and the line location to calculate moment value is varying for these cases. In addition to that, the negative effect of friction force on performance creates an undesirable situation and minimizing them has been the main subject for this thesis.

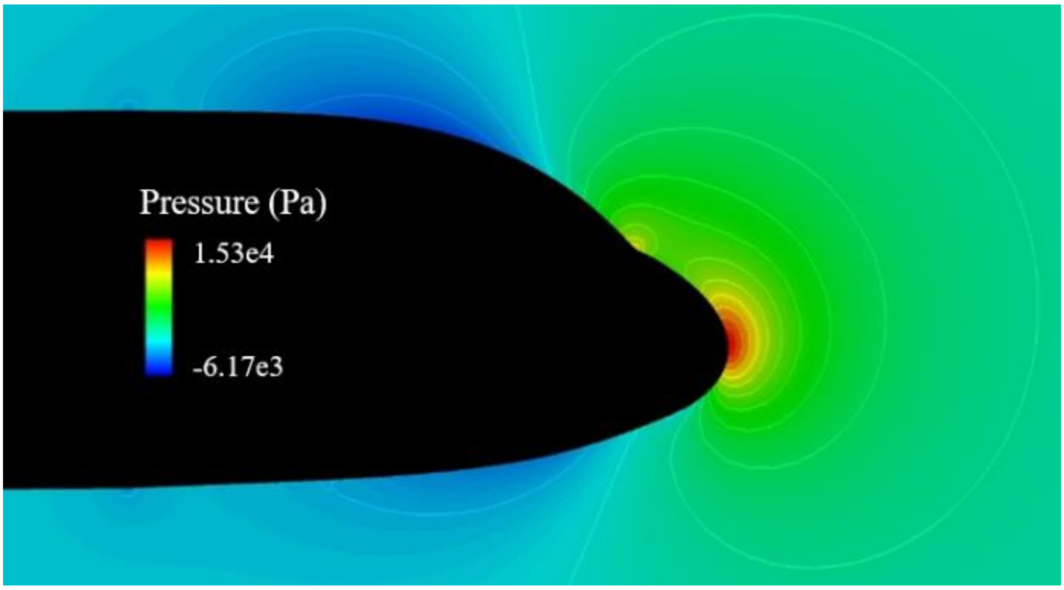

Figure 1.7 : Pressure Distribution Around Nose Radome of An Aircraft (Whalen, 2018).

One of the critical factors in the aerodynamic evaluation of these axisymmetric structures is the position of the radome area on the aircraft regardless of the surface geometry. The significance of this position is not only to shorten the momentum arm originating from the mentioned lift force but also causes the different aerodynamic coefficients by the changing boundary layer thickness. Different thicknesses in the structure determined to increase structural strength or decrease electromagnetic signal losses do not influence the aerodynamic analyses here. The reason for this is the production of radomes from the female mould in Figure 1.5. That is, the surface to be determined by aerodynamic analysis is directly the mould surface. Therefore, the altering in thickness value, especially for the strengthened zones, affects the inner skirt, swept volume clearance and flange designs, but the aerodynamic surface is already frozen. Thus, roughness and production tolerances along the surface of the mold move engineers to a different point than the one calculated in theory within the scope of the deterioration in the boundary layer. As an example, the surface roughness effect on the NACA0012 airfoil is given in Table 1.2. In the same conditions, it is expected to observe a table-like behavior at a different angle of attacks in radome applications. It is seen in the table that the wire roughness area applied is inversely proportional to the minimum drag and maximum lift values.

Table 1.2 : Experimental Aerodynamic Characteristics of NACA0012 Airfoil with Different Roughness Applications (Re=1.5x10^5) (Chakroun et al., 2004).

Application	Min Drag	Max Lift	Stall Angle of Attack	$(L/D)_{max}$	Angle of Attack at $(L/D)_{max}$
25% Wire Roughness at LE	0.04656	0.09825	14	9.07	6
50% Wire Roughness at LE	0.0613	0.9422	14	6.63	8
25% Wire Roughness at ¼ chord from LE	0.0419	0.8585	12	10.17	6
50% Wire Roughness at ¼ chord from LE	0.0506	0.8556	12	8.78	8
25% Wire Roughness at TE	0.0259	0.9247	12	21.45	6

Here, CFD analyses were performed by sieving the geometries created by the genetic algorithm to find the mentioned coefficients. To obtain these coefficients accurately, the methods must be changed according to the flow regime. This depends on some parameters, like air velocity and altitude. When these parameters are defined adequately, the Mach, Reynolds number, pressure, dynamic viscosity and density values are already calculated according to the Standart Atmosphere Table (COESA, 1976) and 0. All these required air properties will be prepared to use as the input file of CFD solver.

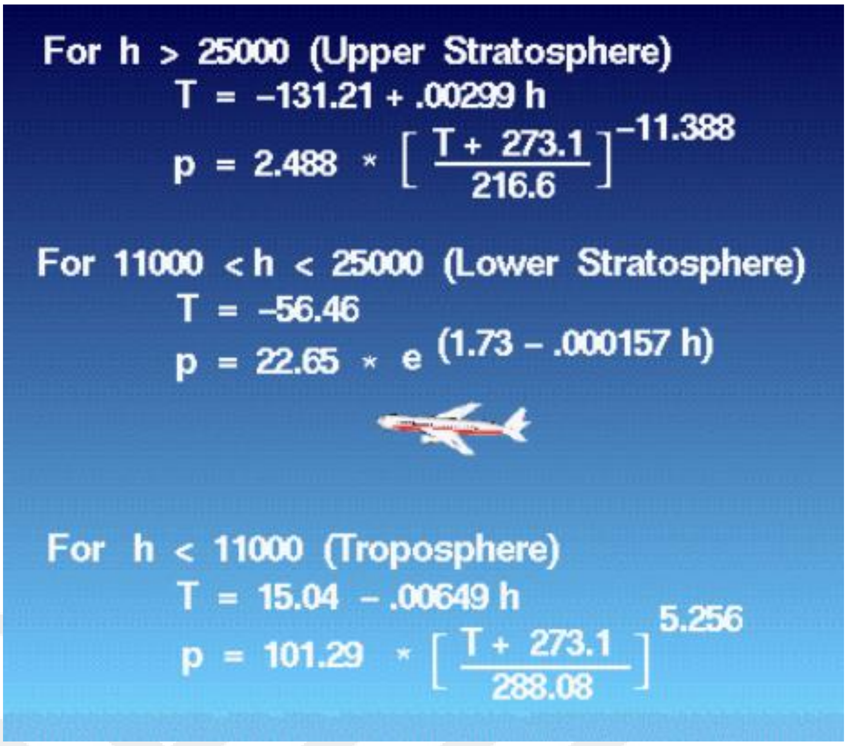

Figure 1.8 : Standard Atmosphere Calculation, Air Properties (NASA, n.d.).

Today, package programs such as Fluent and OpenFoam are preferred to perform parallel solutions and to reach faster solutions to estimate the pressure distribution on the determined artificial radome models. It is often very costly to solve the entire aircraft surface with radomes. With the novel approach of the genetic algorithm developed within the scope of this thesis, simplifications were made in this regard and the domain was created accordingly. However, while making these simplifications, the leading length is taken directly from the real model to represent the truth correctly for the developing boundary layer thickness. Also, during the 3D Geometry creation process, it is necessary to examine the shapes that can occur with too many parameters and the intersections with the payload should be determined. While all these processes are carried out, potentially unproductive surfaces also must be eliminated. All these processes are also covered in this thesis and these restrictions, which will reduce the solution time and prevent the absurd surface formation, have been well evaluated and pre-eliminated with the new genetic algorithm approach. The fine quality of these surfaces was also ensured by the surface modeling commands of the Catia V5 program, and the design, mesh tools and aerodynamic analysis tools, which are among the best in this field, were run together and the complex structures were coordinated with an efficient and properly developed genetic algorithm.

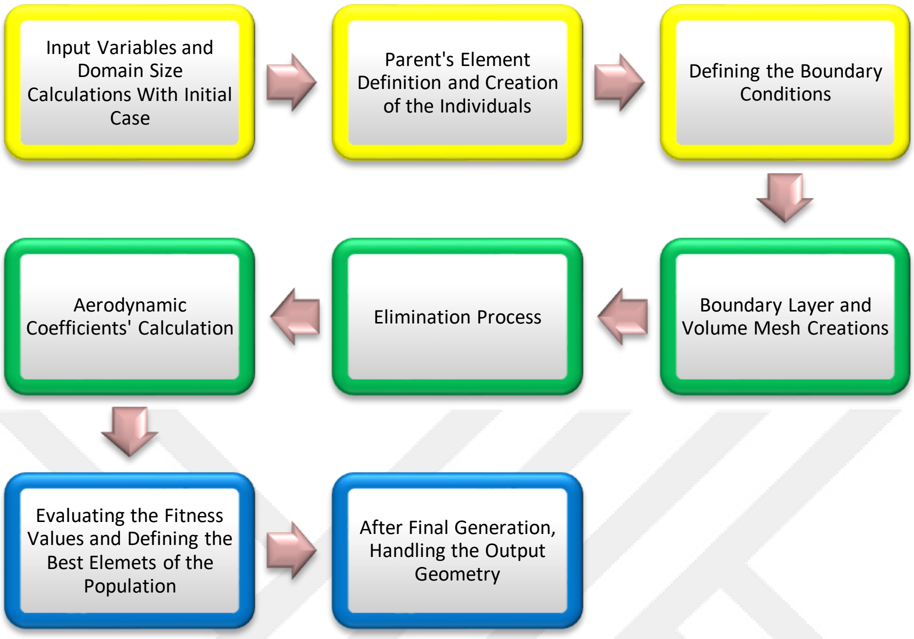

Figure 1.9 : Aerodynamic Shape Creation Chart of this Thesis.

1.2 Literature Review

In this section, aerodynamic studies and design methods of radome structures in the literature are assessed. The monolithic or sandwich stack-up details of these radomes have culminated in the first phase. After that, with the staggered form, the composite radomes also give thickness information for every zone and become convenient for aerodynamic evaluation within the multidisciplinary optimization tools. The sample ply and core sections from these stacking types are visualized in Figure 1.10. (Kozakoff, 2010) The flange regions or fastener locations are designed as solid laminate such that this ensures high mechanical properties for the interface with the platform. However, in some cases, this situation cannot be possible because of the flange length availability.

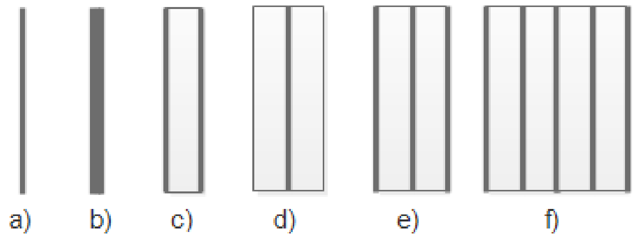

Figure 1.10 : Composite Radome Wall Structures a) Thin Monolithic, b) Half Wavelength, c) A type, d) B type, e) C type, f) Multi-layered sandwich (S.Ilavarasu et al., 2018).

The transition stages of the radomes, whose thicknesses and sequences are already determined, to the aerodynamic analysis process and their evaluation within the optimization are generally done through a two-dimensional section. With the surface generation applications like extrusion or sweep of the curves, the 2D optimized curves may be converted to the radome-like surface in some of the studies about radome aerodynamic surface optimization. (Shankar et al., 2020)

The optimization process is carried out through 2D sections in such sources, and the final 3D analysis of the surface formed by some assumptions associated with the transition to the 3rd dimension is carried out. These processes and assumptions can easily manipulate the desired faces of the radome due to the multiplying the existing parameters with uncontrolled coefficients.

Moreover, these approaches generally are not capable of considering intersections with the inside payload because of the lack of multi-section execution. The one other positive side of the multi-section approach to creating 3D faces is the high surrounding capability for the mentioned payload with aerodynamically efficient fitness values. To achieve all, the radome must contain parameters in many sections under certain limitations (for surface quality), or the representation of the shape with NURB surfaces determined by the movement of the connected control points in the x, y, z axes. In this context, in order to examine the differences between 3D and 2D coefficients, the drag values of circular cylinder and sphere are visualized. (Figure 1.11)

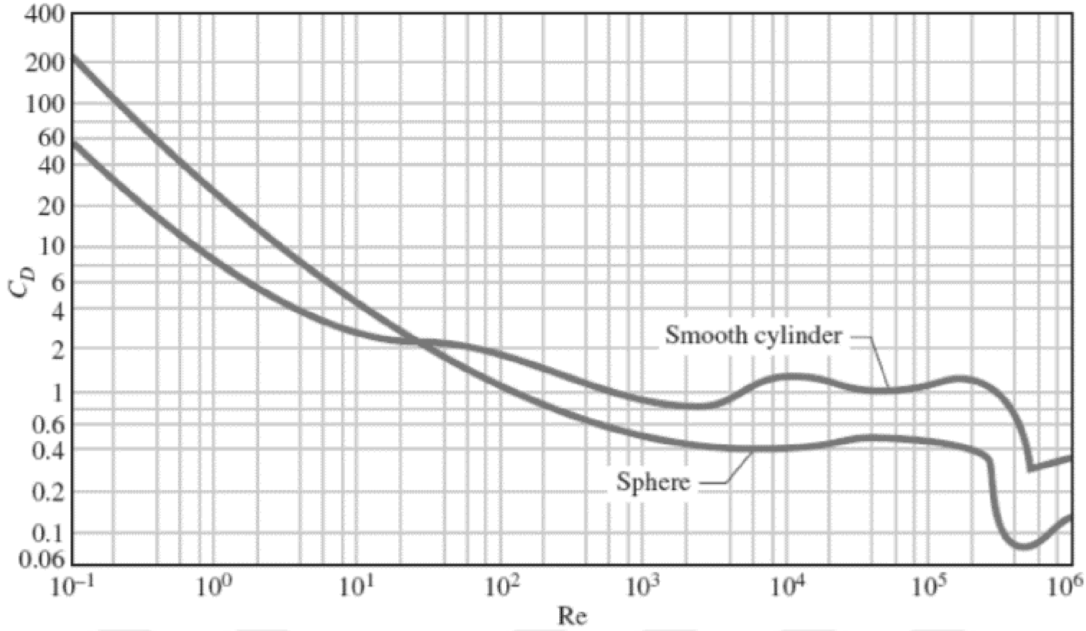

Figure 1.11 : Change in Drag Characteristic of Sphere and Circular Cylinder with Re (Kanoglu, 2007).

In this study, to be heedful of this situation, 3D geometries will be constructed by the pertinent curve groups. Aside from this, the analytic recommendation ways are entreated. For instance, the Breguet Equation tenders a formula to create a range and endurance efficient radome surfaces and this method focuses on the drag sensitive performance healing. For the constant lift coefficient and velocity values, range and endurance equations become like below in terms of the initial and final weight of the air vehicle. (Nygren & Schulz, 1996)

$$Range\ Equation = \frac{V}{c}\frac{C_L}{C_D} ln\frac{W_0}{W_1} \tag{1.2}$$

$$Endurance\ Equation = \frac{Range\ Equation}{V} \tag{1.3}$$

Here, V and c values are pointed out the velocity and specific fuel consumption. SFC can be defined as the fraction of the used fuel per hour and thrust. When both sides of the equation (1.2) are partially derived with the C_D, the relation between the drag change and decrease in a range from the radome is found out. (Loos & Giragosian, n.d.)

$$\frac{\Delta Range}{Range} = -K\frac{\Delta C_D}{C_D} \quad (1.3)$$

K is the semi-empirical constant as a function of the engine and air vehicle structure. (≈ 1)

Another radome design guide is given in Figure 1.12. The geometric parameters of the radomes are simplified in this source. The factors affecting the pressure distribution on the radome are severely comprised of radome location, aspect ratio and cross-section area.

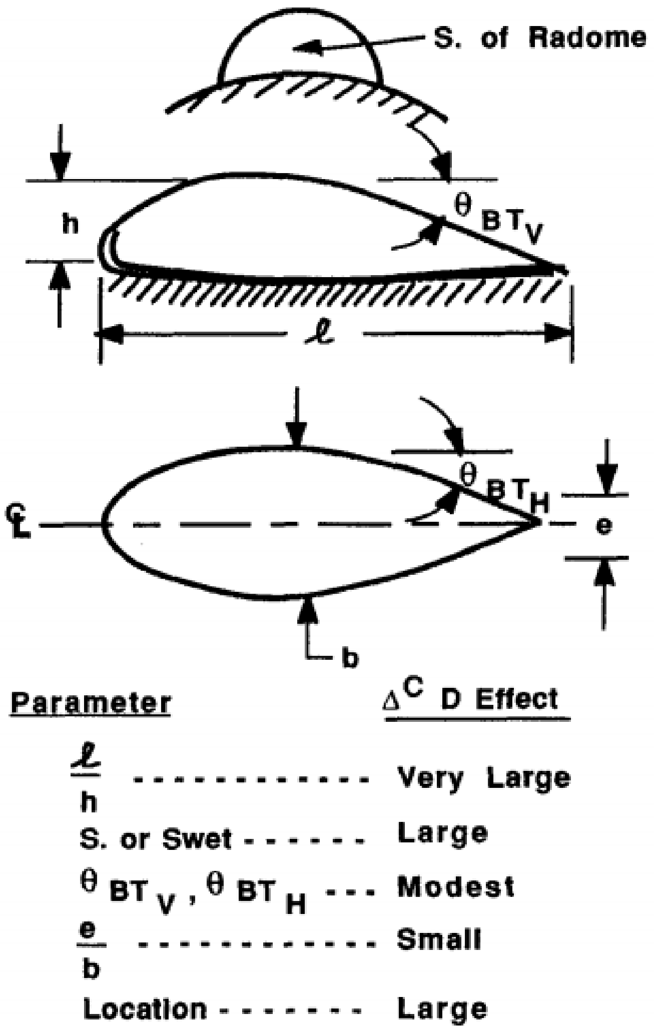

Figure 1.12 : Radome Design Workbench and Tips For their Shape (Loos & Giragosian, n.d.).

Generally, as a result of this aerodynamic optimization, when the objective functions are defined as drag minimization or maximization of the lift (max L/D), the geometries become emerged in a manner that resembles the airfoil. However, in this thesis, considering the structure with all the air vehicle geometry, the minimization of both values for stability is aimed because the radome is located on the front side of the wing structure. The reason why the radome location is chosen here is the icing conditions from the engine, mechanical obstacles and harness distances between the cabinet racks and antenna, etc. This condition is similar in the shell geometries of cars. It is a primary goal to obtain a smooth surface by taking into account the condition of minimizing the lift and the payload part in it. But, this time, the shape that resembles the reverse airfoil comes up with a hatchback-like surface without the sharp trailing edge.

The comparison of the well-accepted optimization methods and related literature surveys with the optimization subject of this thesis are detailed. The determination of the analysis method and the screening algorithm, and their conversion to a general algorithm in this thesis have been revealed on the basis of a problem encountered as an engineering requirement. Here, the optimization algorithm and aerodynamic problem are evaluated together and genetic algorithm and Fluent program are decided to use. Still, alternative methods and programs are not ignored and the literature is examined in this context meticulously.

The general optimization methods are classified in Figure A.1. According to this method of classification, the most used three methods are handled. From the stochastic methods, a simple genetic algorithm, simulated annealing methods and gradient-based method from the deterministic approach are investigated. The general behaviors of those methods are drawn in Figure 1.13.

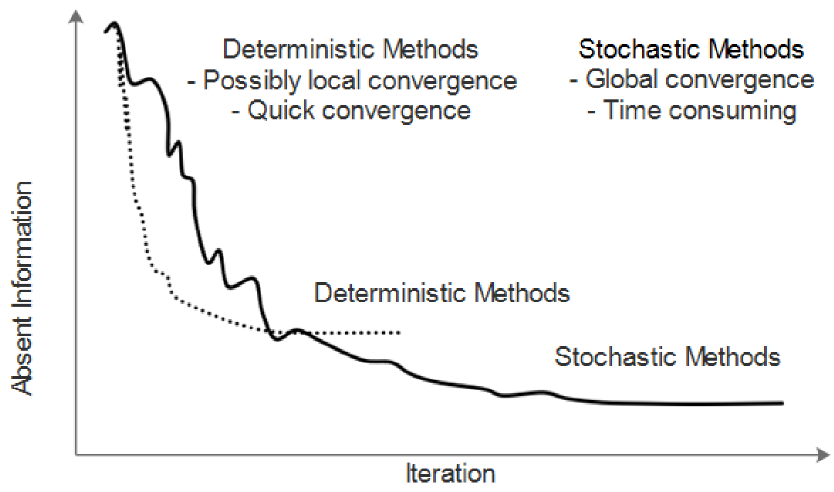

Figure 1.13 : Computational Behaviors and Time-Consuming Comparisons of The Stochastic Method and The Deterministic Method (Osaragi, 2017).

In an article that includes comparisons of genetic algorithm (GA), simulated annealing (SA) and gradient-based method (GM), it is aimed to maximize c_L value by evaluating two different parameter groups of two airfoils (NACA 2412 and NACA 64-412) with the panel method. (Obayashi & Tsukahara, 1997) In the first test case here, only two geometric parameters belonging to the airfoil equation were modified and their optimization was performed under certain limits and specific flow conditions using these methods. However, because the same parameters in two different airfoils are evaluated together with the gradient-based method, especially when the penalty function is not applied, one of the parameters has a positive effect for one of the airfoils and not for the other airfoil. The results of the solution with the gradient-based method containing the penalty function created to prevent this, yet remained in a narrow local range this time. Besides, as mentioned in section 3.1.1 , the difficulty of application of the gradient-based method in practice was mentioned in the same article and it was stated that the genetic algorithm is more efficient in finding the right optimum value.

And then, for the second test case, this initial time guess was made in 4 different alternatives for 4 parameters. Unlike the first case, only the number of parameters has been increased from 2 to 4 and the initial parameters are specified for this second case.

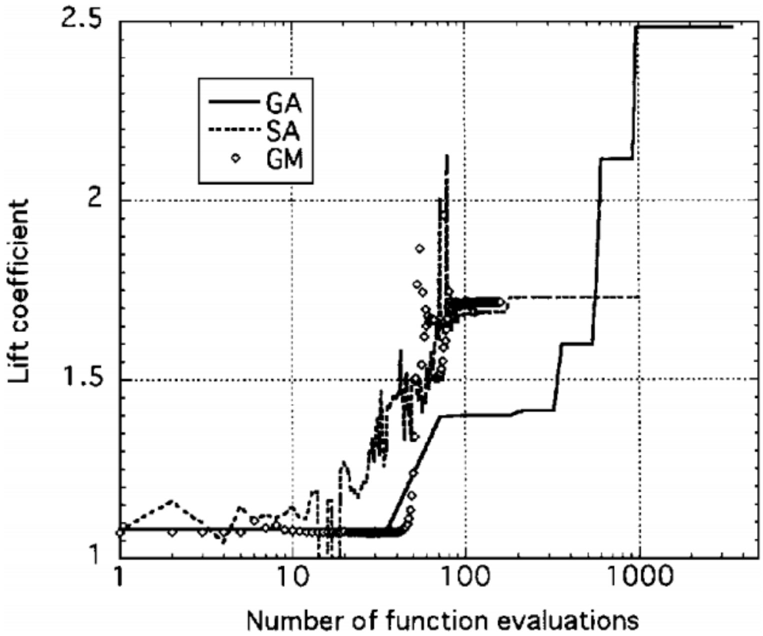

Figure 1.14 : Comparison of SA, GM and GA Methods for Maximizing c_L (Obayashi & Tsukahara, 1997)

This situation is very advantageous for Simulated annealing and gradient-based method because it is known that the closer to the real result, the shorter the solution time for these methods that adopt the hill climb strategy. However, it is unlikely that these initial geometric parameters can be estimated correctly in terms of aerodynamic coefficients. The second test case results (Figure 1.14) in this article also confirm that these parameter values cannot be easily predicted well.

In contrast, in a genetic algorithm, the fact that the first population is close to the real value among the populations included in the natural screening process does not affect the success of the algorithm in finding global results as much as other methods. This difference becomes evident, especially when faced with discontinuous problems. (For example, the shock wave problems for compressible cases)

Despite the excessive solution time, the argument in this source (Obayashi & Tsukahara, 1997) is that in the case of optimization of the aerodynamic coefficients, the genetic algorithm method is much more preferable.

On the other hand, in other sources (Štorch & Jiˇrí, 2017), (Tomac, 2011), where the mentioned methods are compared regarding the solution method of the problem, there are comparisons of these methods from different directions. Fidelity of these methods is crucial for a radome optimization because of the requirement of the separation prediction or turbulent flow conditions; however, they require more detailed CAD surfaces. The gathered information from this literature survey of the aerodynamic methods are summarized in Figure 1.15

In a more explicit expression of the increasing cost, it is known that the LES method requires a solution capable of 10 teraflops. At the same time, it can be seen that even standard quad-core computers can solve in minutes with solutions made with strip theory or potential methods. However, it is possible to obtain the values closest to today's test results with LES or RANS methods. Considering today's computing capacities, it is known that the Sunway TaihuLight supercomputer, which is considered as one of the fastest computers in the world, offers a solution speed of 93 petaflops. (Witherden & Jameson, 2017) Now, the high level of supercomputers makes this LES method very difficult to use, especially the use of these multi-solution methods, such as optimization techniques, which come up with a critical limit in the use of the LES method. In the future, it will be much more possible to simplify these methods and to apply optimizations in these methods with increasing computer speeds. For this reason, the calculation form in this thesis was realized with the FLUENT program that offers the RANS method solutions.

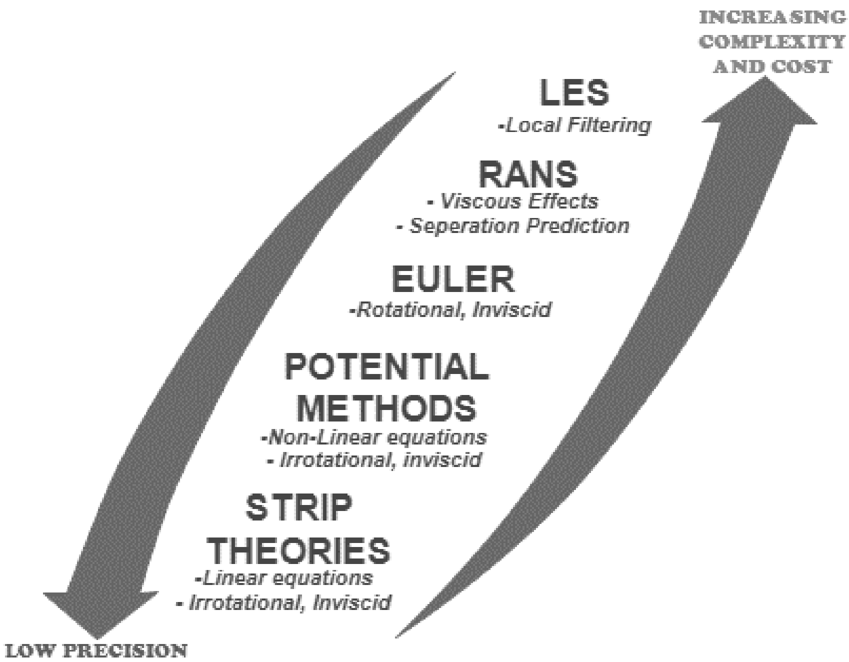

Figure 1.15 : Hierarchy of the CFD Methods.

1.3 Purpose of The Thesis

The use of mobile communication systems is becoming increasingly crucial for the aviation industry, which is intimately affected by technological developments. The widespread use of the internet or satellite communication tools in both defense projects and the civil aviation sector during the transportation of passengers or performing missions has revealed some requirements. One of these requirements is directly related to the study carried out in this thesis, and special integration processes are defined for electronics, radar equipment that meet these needs. At this point, a cover is needed to protect all these interfaces, protecting them from external factors. This cover structure is called as radome and details of them given in previous sections. However, these structures may require design processes that are as complex as the equipment they contain, and sometimes they even may require a more complicated process than them.

The main aim of this thesis is to find the most successful individuals according to the determined criteria by using the optimization algorithm of the radome that is planned to be integrated on the specific aircraft. To achieve this fundamental goal, an efficient product has been tried to be produced regarding time consumption. But here, aerodynamic analysis and design processes need to be handled together. Therefore, ensuring that all these processes are automated has been determined as another targeted subject.

The scheme makes it easier to understand the purpose and functioning of this thesis. (Figure 1.9) Here, the life cycle of a population in 8 stages is given. By repeating all these processes until all the iterations sufficient to find the best result are completed, the optimized radome is obtained in the 8th or last stage of the cycle.

Even though the complex shape generation requirements and aerodynamically unstable behavior of them, when the cycle processes are completed successfully, the most suitable structures can be found according to the objective function information, which can be easily implemented by finding the best of the offspring derived from randomly developed populations in an absolute and fixed cruise flight condition, without taking into account of the whole aircraft body, the approximations are conducted for a specific region of the aircraft to find these mentioned best elements.

1.4 Structure of The Thesis

Look back to the consistent framework of this thesis, and the introductory chapter is placed over the content plan with the endowed literature survey and definition of the main actor (aircraft radomes). The one is referred to as revealed study in this thesis and these are the design phases with the production fiction of each to use efficiently in any stochastic optimization method as CAD constraint. Their fictions already have to be instructed by the manufacturing side and material selection guide that is detailed for future MDO studies. When the related papers are examined in the literature review section, the pros and cons are reflected with explanations and inducements is compared with the idea of this work. Learned lessons are sculpted to the 3D radome optimization algorithm as an objective function or elimination method. In this context, the literature review and aerodynamic concept work contributed a lot of entry and knowledge to the underlying base of the thesis' code structure.

Superficially, the central portions of the thesis subject are split into the two main headings. The one is genetic algorithm installation for the system and the other one is made up of the endorsed solution specifications. Before them, for Chapter 2, the geometry creation basics and input variables are summoned with their technical sides and analytical background. The baseline of the genetic algorithm method is revealed here and the representation of them is itemized by accepted methods. These elaborated basics carry the issue to other fields in the continuum structure of this study, like detailed modeling of the fluid domain with the grid structure.

The most used optimization algorithms in this field are compared by the time consumption and accuracy matters. As the decision authority and commander for the thesis' main code, the optimization algorithm holds a decisive place for all steps and the genetic algorithm method is selected accordingly. By checking the conformity with this method, subsequently, developed specific selection algorithm is given with the significant effects on the evolution and their initialization period. The other crossover and random mutation operations are managed to generate many offspring lists. To enhance the code efficiency and speed, all parents are stored as a numeric package. And the crossover parameters are not be stirred while replacing with each other. Here, the similarity of the lateral sections in the radome structure was used and the elements in a similar row, column were changed and the others were kept constant. For the discussed radome structure, which is planned to be deployed on the planar surface, in this scope, zero value assumption for many parameters also helped to eliminate many of which without moving the solution away from the global area. Non-repeating parent solution way also offers reduced solution times when compared standard algorithms fairly. The details of them and test objective solutions without aerodynamic assessments are also examined in Chapter 3.

With Properly defined boundary conditions, the meshed domain is subjected to flow conditions from the predefined air quantities. By the aerodynamic discretization of the domain, selected fluid flow solver program strives to predict velocity, pressure and density variables at that settled node values inside of that volume. However, the grid convergence study is included in Chapter 4 by comparing all the domain size probabilities and their permutations are applied within 3D and 2D solution trials. On the other hand, the y+ calculation is devoted to this chapter to achieve right variable prediction in the boundary layer of the radome surface. Therefore, the boundary layer mesh thicknesses are determined for that. After importing the eligible step file to the ANSA Mesher, ANSA Script code (in Python language) is developed to handle these processes for all iterations. The quality check operations and calculating the off-element system are implemented in this script as well. This process was carried out until all analyses went below the criteria set for the skewness, aspect ratio values and warping. Finally, the output msh file is written to the Fluent data folder.

In chapter 5, the methodologies of the fluid flow solution methods are pointed. How aerodynamic analysis can be used in the optimization algorithm is expressed by applying specific discrimination methods on the methodologies specified in this section. A comparison of panel-based solution methods stands on potential flow logic and DNS, LES and RANS approach, which are carried out today as the frequently applied eulerian technique is also provided. They are included in two lines that are essential for the computational fluid solution (eulerian and lagrangian approaches). Concerning the thesis topic here, some major flow features are dealt with. (Rotation, Turbulence, compressibility, separation sensitivity, etc.) After evaluating these details and determining the solution methods accordingly, the explanation and formulation of the Realizable K-ε Turbulence Model are detailed and reported as a turbulence approach in this chapter likewise.

In light of the parameters that have been specified so far, validation works have been carried out by analyzing the aerodynamic solution methods of various airfoils in 2D. By completing this step, the mesh structure, flow conditions and the created CAD geometries are defined and combined with the Fluent application. Optimization results following the coefficients obtained from this solver.

When the optimization process is completed, it is crucial to examine the obtained values from two aspects. The most important part of this thesis has been the state of fitness values converged by the analyses performed on whether the algorithm is working correctly or not. It is the first title of Chapter 6 to show that fitness values behave independently of the number of iterations after a particular iteration surely. By evaluating these values together with their solution times, the maximum number of iterations and the maximum number of parents to be included in the population are determined, where the most suitable fitness values can be attained. In addition to comparing and interpreting the best solutions obtained as a result of all these evaluations, the pressure coefficient and the distribution of the pressure on the surface were reviewed as the final post-process step. As intended, depending on the calculated Lift and Drag values, the final shape of the geometry is determined and evaluated through the specified objective function in the early stages of that algorithm.

2. CREATION OF THE INITIAL GEOMETRY AND DEFINING THE PROPERTIES

2.1 Determination of The Input Variables

Some parameters of geometric dimension information will be considered constant in all analysis solutions since the result to be obtained during the determination of the input values is intended to convert the pressure distribution and the forces acting on the surface into a comparable form based on coefficients. "Reference Area" and "Chord" parameters in the formulas of Lift and Drag forces are one of them. The formulas used to convert these resultant force values to coefficients are expressed in the scope of equation (2.1).

$$L = \frac{\rho . V^2 . S . c_L}{2}, \quad D = \frac{\rho . V^2 . S . c_D}{2} \tag{2.1}$$

Here the variables that take place in (2.1) are given in seriatim. ρ is an air density, S is a reference area, V indicates the freestream velocity and c_L, c_D are the aerodynamic coefficients. In the context of the thesis, if the condition of minimizing these c_L, c_D values are targeted, other parameters must be determined in order to obtain the coefficients from both Lift and Drag force values calculated with the help of Fluent. The reference area and chord values are taken as 1 for all cases, but if the effect of the aircraft on the increase in drag count is observed, these values are taken as 18m2 for the wing area and 1.2m for the mean chord. These values do not affect the coefficients when calculating force; here, only the resemblance of the Re and Mach numbers between the cases is vital in terms of geometric dimensions for this incompressible solution.

The cruise flight condition of a cargo aircraft has been considered to determine the output of the case. The reason for the assessment of the cruise condition is that the aircraft body in the air mostly exposed to this environment throughout its all lifecycle and missions. This condition also attained as the most efficient flight path to generate optimized results.

The cruise speed for the cargo plane handled as an example is considered 94.7 m/s. Also, the cruise flight altitude is determined as 30000 ft from the sea level. This means the Mach number is designated approximately 0.3. If the Reynolds number was checked by (2.2), the status of the flow is specified as turbulent and incompressible for external flow conditions.

$$For\ Turbulent\ Flow: Re = \frac{\rho.V.D}{\mu} > 5.10^5 \tag{2.2}$$

The density and dynamic viscosity values obtained from the information given in Figure 1.8 and further, the values are extracted from the calculations made on the Standard Atmosphere Table to calculate the Re number value. These values were found to be 0.65 kg/m^3 for ρ and $1{,}59x10^{-5}$ Ns/m^2 for μ. In addition, dynamic viscosity can be found by applying the Sutherland formula from the temperature information at that altitude.

$$\mu = \frac{1.458\ x\ 10^{-6}.T^{1.5}}{T + 110.4} \tag{2.3}$$

The unit of the air temperature is accepted as Kelvin.

The sub-validation work is conducted by the total pressure comparison in this stage. Because the flow compressibility is found at critic interspace. Notably, the literature displays the transition point from incompressible to compressible, where this is nearly 0.3M. This depends on the differences between the total pressures obtained from equation (2.4) and (2.5).

Firstly, the Bernoulli equation is used to calculate the total pressure value for freestream:

$$P_{TOTAL} = P_{STATIC} + \frac{\rho.V^2}{2} \tag{2.4}$$

The total pressure value calculated by equation (2.4) is 7.185 Psi. On the other hand, using the Isentropic Flow pressure equation (2.5), it is calculated for freestream values where the total pressure value is 7.175 Psi.

$$P_{TOTAL} = P_{STATIC} \cdot \left(1 + \frac{\gamma - 1}{2} M^2\right)^{\frac{\gamma}{\gamma - 1}} \tag{2.5}$$

Since it is alleged that the correct value should be obtained from the equation (2.5); therefore, the error in the total pressure remains nearly 0.14%. This value indicates that the incompressible solution is applicable under this condition.

After the flow parameters have been completed, all the inputs of the optimization algorithm must be defined completely. Other parameters are the essential geometry creation inputs, and they are demanded by the genetic algorithm that aimed to reach the final result. These inputs make an interface between all necessary pieces of information that can be determined for every iteration, such as the number of elements belong to their population and the number of parents to be selected in each population. This is presented to the user in the first part of the code. Some of these are accepted as fixed for the long-sought geometries, such as intervals of the curves that enable the parallelism constraints. All of these intervals represent the 3D curve structure and their point sequences with specific distances. While arranging the convergence to the requested curve shape with minimum points, the errors between the real one and point representations are minimized by the spline command of the CAD software CATIA. Therefore, these parameters are assigned as constant but, in an unusual situation, it gives the user a chance to change that by Python interface.

Here, some input values that affect the result, as these parameters, these are presented to the user control. For example, the objective function value of the solution is one of them.

```
# GENETIC ALGORITHM(GA) AND THE INPUT VALUES OF GA
elnum=300 #Number of Chromosome in Population
criteria=0 #For the Evaluation
num_generations=60 #Iteration Number
num_parents_mating=8 #Number of Parents
crossoverlen=2 #Split Location (constant)
```

Figure 2.1 : Necessary Optimization Inputs (Python Variables).

To extract the maximum fitness value, the criteria in Figure 2.1 is defined as a positive and minimum number so that the minimize differences between the $eval_i$ and criteria at the same time. (2.6)

$$Fitness_i = \frac{1}{|criteria - eval_i|} \tag{2.6}$$

Where the $eval_i$ indicates evaluation for every element of populations. The importance of minimizing the c_L and c_D values are determined as equal in this cruise flight case. (factor of interest k_n is also modifiable.)

$$eval_i = k_1|c_L| + k_2|c_D|\ ,\ k_1 = k_2 = 1 \tag{2.7}$$

The final interaction control is made by another subcode section using the height and diameter dimensions of the cylindrical swept volume. Easily editable parameters of this equipment are added in this thesis context. These values are determined as 40 cm and 30 cm, respectively.

At this moment, all the base inputs are being completed by the system automatically. This section is the last part of the primary process that comes up with the required gaps to be filled.

2.2 Bezier Curve Representation of The Quarter Sphere

The basic configuration and their production logic of the Bezier curves are discussed in this section.

First, the use of Bezier curves and operations of parametric curve calculation in the baseline configuration is the main focus area of this mentioned logic. Generally, the many optimization ways that derived by the genetic algorithm drives Casteljau's Algorithm to represent shapes in a time-controlled phase or NURB surfaces. Bernstein polynomials are the mandatory terms to understand the working principle of the Bezier curves, which is an adequate curve sculpt.

2.2.1 Basics and application of the Bernstein Polynomials

The first appearance of the Bernstein polynomials was in the early stages of the 1900s, and are unearthed by Sergei Natanovic Bernstein. Bezier curve algorithms established on the base on which these equations emerged after Pierre Bezier's studies. After distracting the computer graphic user engineers, again, Bezier curve approach is gained the popularity among the mathematicians. The ubiquitous theoretical background of the Bezier curves is explained below: (Casselman, 2008)

$$B_{i,n}(t) = \left(\frac{n!}{i!\,(n-i)!}\right) t^i (1-t)^{n-i} \tag{2.8}$$

The first term of equation (2.8) is named as the binomial coefficient and n indicates the power degree of the polynomial. 5th order polynomials are selected, because of the providing enough geometrical deflections for every changing iterations. The 5th order Bezier curve equation is detailed once as follows.

$$\begin{aligned} B(t) = {} & (1-t)^5 P_0 + 5t(1-t)^4 P_1 + 10t^2(1-t)^3 P_2 \\ & + 10t^3(1-t)^2 P_3 + 5t^4(1-t) P_4 + t^5 P_5 \end{aligned} \tag{2.9}$$

Where the $P(x, y, z)$ is the control points in the spatial domain according to the absolute axis system.

Besides, according to Casteljau's algorithm, t value within the scope of equation (2.9) is slid between 0 and 1.

Having considered the specific t value or time, previously defined lines that are between the consecutive control points, show up the specific point locations on ourselves. Computer algorithm runs for the second successive curve groups such that construct a new one until completion of the operation for all the points again with the same t ratio. It can be easily observed that the gathered final point groups for all t values build the section line. Returns the line $B(t)$ formed upon the determination of the t value at certain and frequent intervals.

A visual examination of the situation where the t value is applied over the same control points for two different ratios is tried to be shown in Figure 2.2.

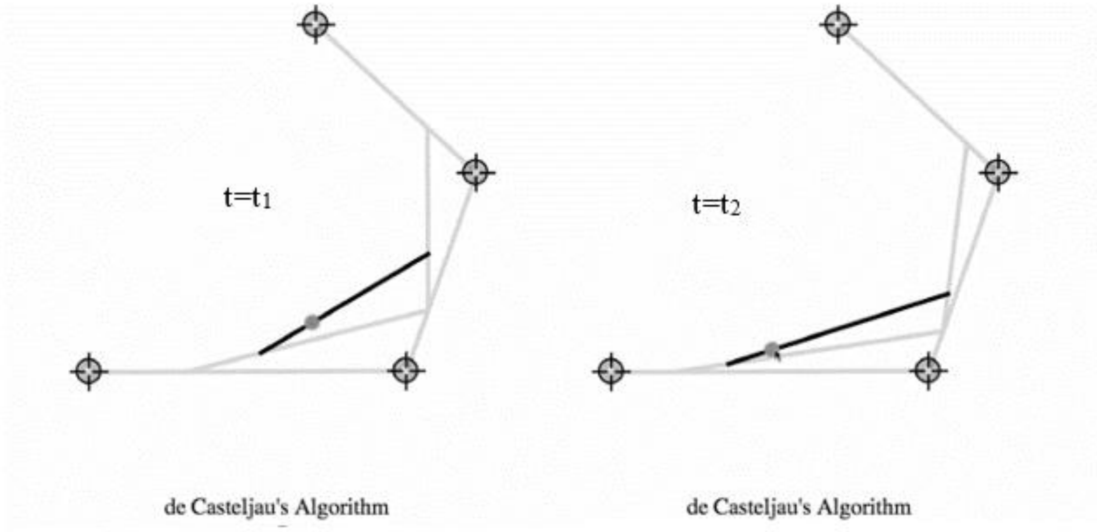

Figure 2.2 : Representative Approach to de Casteljau's Algorithm at Different Times.

Curve definition is made by this basic easily and all the algorithm is set on that basis. However, some modifications are required for a reverse operation like found a representation of known one within the algorithm.

2.2.2 Quarter-Sphere creation

This subsection consists of several mathematical problem-solving operations. Ingredients of the problem are the first and last control point locations. Equation (2.9) is rewritten in a different form to find the control points of the circular 2D curve for every t steps $(1\ to\ n)$.

Here, Matrix multiplication ($A.P_{x,y,z} = C_{x,y,z}$) is detailed (2.10);

$$A = \begin{bmatrix} 5t_1(1-t_1)^4 & 10{t_1}^2(1-t_1)^3 & 10{t_1}^3(1-t_1)^2 & 5{t_1}^4(1-t_1) \\ \vdots & \vdots & \vdots & \vdots \\ 5t_n(1-t_n)^4 & 10{t_n}^2(1-t_n)^3 & 10{t_n}^3(1-t_n)^2 & 5{t_n}^4(1-t_n) \end{bmatrix}$$

$$Control\ Points: P_{x,y,z} = \begin{bmatrix} P_{1_{x,y,z}} \\ \vdots \\ P_{n_{x,y,z}} \end{bmatrix} \tag{2.10}$$

Control points are wanted to be calculated by the contributions of the exact values.

The inverse of A matrix has to be multiplied with after known $C_{x,y,z}$. For the XY plane, RHS can be written in equation (2.11) and it is accepted to be derived again for other axes in this way.

$$C_x = \begin{bmatrix} R\cos(\pi t_1) - R(1-t_1)^5 - R{t_1}^5 \\ \vdots \\ R\cos(\pi t_n) - R(1-t_n)^5 - R{t_n}^5 \end{bmatrix}, \qquad C_y = \begin{bmatrix} R\sin(\pi t_1) \\ \vdots \\ R\sin(\pi t_n) \end{bmatrix} \tag{2.11}$$

Let us know, R_{sphere} value is given as radius of the cylinder or middle section of the sphere; their inputs are identified in Section 2.1. It is also solved for other axes systems and the only needs are summarized as dimensions of the cylinder that include H and R values to find resultant length as a semi-sphere radius. (2.12)

$$R_{sphere} = \sqrt{(R^2 + H^2)_{cylinder}} \tag{2.12}$$

Thus, control points are handled by equation (2.13).

$$P_{x,y,z} = C_{x,y,z}.A^{-1} \tag{2.13}$$

For the shape formed by the initial geometry ($P_{x,y,z}$) discussed in the thesis, t values were brought up to 1 in 5 steps. It was decided to determine the values at 5 intermediate points for the period after the error values occurring for the structure represented by the bezier curve were analyzed as discrete at 32 intermediate points, and the maximum error remained in the order of less than 0.016cm which is enough to start. Because in the case that this situation will be modified and will reach the real result, the discrimination of the points representing the splines will be provided over a minimum of 32 points.

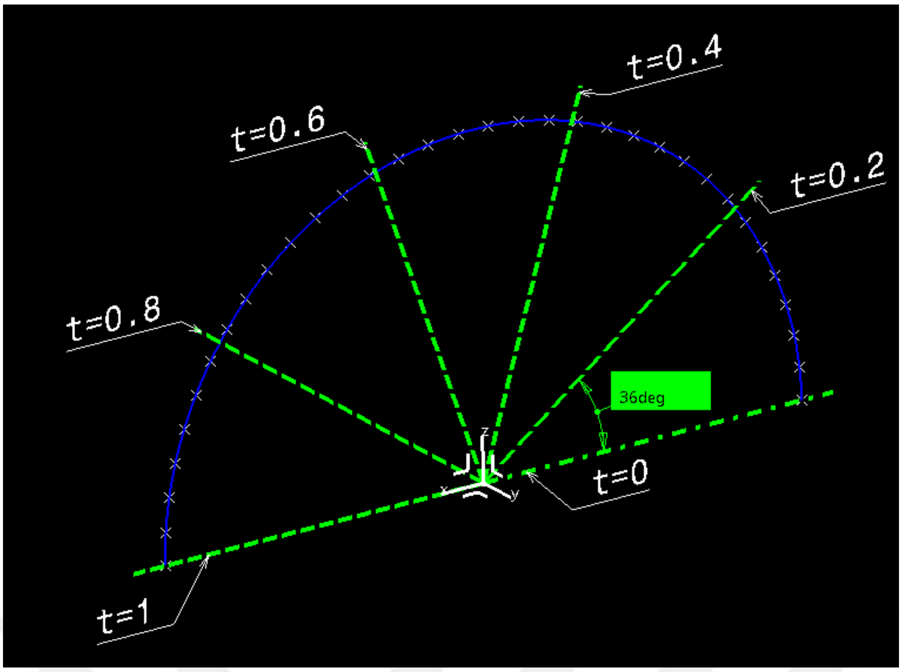

Figure 2.3 : 2D Semi-Circle Bezier Representation Result (Blue Curve: Exact Circle).

As a result, one of the most important reasons for determining the initial geometry as hemisphere that is a dull formable surface that will wrap the cylinder selected as the internal volume limit with the minimum offset space. In this way, the algorithm, where drag will be minimized, includes a surface that is based on simple mathematical fundamentals and can be manipulated quickly in the Python code. The initial hemisphere radome with 3D sample cylinder constraints is given in Figure 2.4.

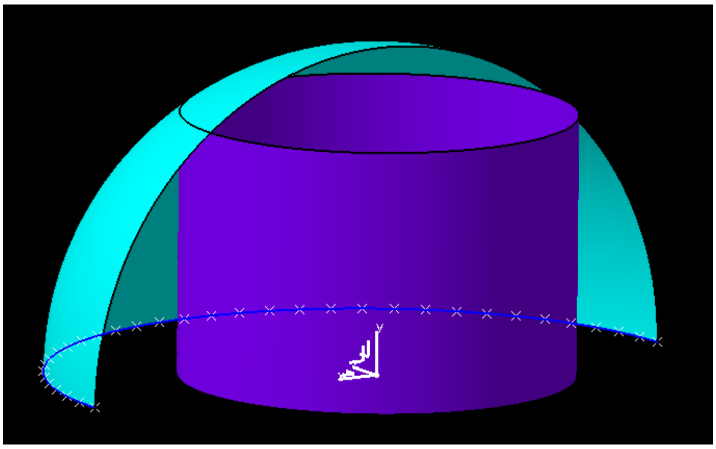

Figure 2.4 : Initial Radome Geometry from Created Nearly Semi-Sphere Surface.

3. OPTIMIZATION ALGORITHM

The purpose that explained in the introductory chapter must have the two main drivers for the created encoding. One of these drivers is about the optimization itself, which is the underlying driver that shapes the entire code structure. The other is the solution part, that is the last stop of the optimization technique. In this chapter, the optimization algorithm and the selection reason is explained with technical side effects.

3.1 Optimization Techniques for An Engineering Problem

Nowadays, there are plenty of ways to get optimized results. According to the objective function of this work, the Evolutionary Algorithms and Adjoint-Gradient Methods are the most common models to approach the final result. In this chapter, there will be a comparison of them and their reviews within the scope of advantages and disadvantages.

3.1.1 Adjoint-Gradient method

CFD solutions are present the external and internal flow calculations that are computationally costly for standard computers. The Adjoint method strives to make this approach a little more innocent as a part of gradient-based methods. Because their optimization times are shallow when it is compared with evolutionary algorithms. Even in more academic sources, evolutionary algorithms are described as stochastic. The reason for this is the more iterations they require than the adjoint methods. The approach of this optimization method is explained in short examples:

Let's apply this method to find the minimum of $f(x, y)$,

$$f(x,y) = x^2 + y^2 \tag{3.1}$$

The initial value can be defined as $(2,1)$, after that the gradients are calculated below;

$$\frac{\partial f}{\partial x} = 2x, \quad \frac{\partial f}{\partial y} = 2y \tag{3.2}$$

With the Lagrange multiplier (h), the second term is obtained;

$$f^{i+1} = f^{i} + h\nabla f \tag{3.3}$$

In here, f^{i+1} can be determined;

$$x^{i+1} = 1 + 2h, \quad y^{i+1} = 2 + 4h \tag{3.4}$$

These values substituted to equation (3.1). To get minimum value;

$$\frac{\partial f}{\partial h} = 0 \tag{3.5}$$

From equation (3.5), h can be found as -0.5. Therefore, the minimum value of $f(x, y)$ could be obtained with $x = 0 \; and \; y = 0$ which is known. When the AG method is implemented for the airfoil or wing optimizer, changes in the X cause an alteration on C that demonstrated in the equation (3.6). Let's assume, the coordination of airfoil or wing boundary data is screened as X and the flow field parameters are represented with Q. In this case, the cost value can be expressed as:

$$C = C(X, Q) \tag{3.6}$$

ΔC is managed by equation (3.7).

$$\Delta C = \left[\frac{\partial C}{\partial X}\right]^{T} . \Delta X + \left[\frac{\partial C}{\partial Q}\right]^{T} . \Delta Q \tag{3.7}$$

According to the converged result, the residual vector is already known as zero for this example;

$$\Delta R = \left[\frac{\partial R}{\partial X}\right] . \Delta X + \left[\frac{\partial R}{\partial Q}\right] . \Delta Q = 0 \tag{3.8}$$

Similar to the example mentioned previously, equation (3.8) is multiplied by transpose of Lagrange multiplier and subtracted from ΔC;

$$\Delta C - \Delta R = \Delta C = \left(\left[\frac{\partial C}{\partial X}\right]^{T} . \Delta X + \left[\frac{\partial C}{\partial Q}\right]^{T} . \Delta Q\right) - h^{T} . \left(\left[\frac{\partial R}{\partial X}\right] . \Delta X + \left[\frac{\partial R}{\partial Q}\right] . \Delta Q\right) \tag{3.9}$$

Coefficients of the ΔQ are determined as zero,

$$\left[\frac{\partial C}{\partial Q}\right] = h.\left[\frac{\partial R}{\partial Q}\right]^T \tag{3.10}$$

From the remaining part of the equation (3.9),

$$\Delta C = \left(\left[\frac{\partial C}{\partial X}\right]^T . \Delta X\right) - h^T.\left(\left[\frac{\partial R}{\partial X}\right]. \Delta X\right) \tag{3.11}$$

Equation (3.11) must be solved once for every iteration. Therefore, the computational cost will be reduced in this way. (Tashnizi et al., 2010)

This method basically has two types; one of them is discrete and the other one is the continuous adjoint method. The main differences between them are the memory requirements and gradient accuracy as a result. For the continuous adjoint solvers, the turbulence solutions are not accurate as of the discrete because the continuous adjoint method neglects the turbulent parameters of the flow equations. The discrete method is often used with two-equation turbulence models or one equation Spalart-Allmaras model for the aerodynamic coefficient optimization. (Schramm et al., 2018)

Despite all the advantages, the method has many disadvantages for radome optimization in this thesis. The major disadvantage is the complexity of the fiction of formulations and derivations from both flow equations and the custom geometry limitations. This can be seen as convenient for the two-dimensional airfoil optimizations or other wing optimizations that consist of two-dimensional little-different sections (2,5D). Yet, it is not found feasible to apply this method to a spherical or resembling dome structure. The reason for that, the process has to eliminate the surfaces that have intersection area with the cylinder and implementation of these detections are causing the difficulties to create gradients. The representation of the electronic equipment becomes vital for the whole solution; without them, the objective function and problem are going to be different.

In the literature, these two methods have been applied for SST wing-body configuration and the shape optimization of this configuration (Sasaki et al., 2001). The objective function of the research is about minimizing the L/D ratio. The research has revealed the results which are given in Table 3.1.

Table 3.1 : Comparison of the Adjoint Method and Genetic Algorithm Per Aerodynamic Coefficients.

	Initial	Adjoint Method	Genetic Algorithm
C_L	0.099962	0.100154 (+0.19%)	0.099978 (+0.02%)
C_D	0.006346	0.006267 (+1.24%)	0.006226 (+1.88%)
L/D	15.75232	15.98111 (+1.45%)	16.05708 (+1.94%)

In Table 3.1, the initial airfoil geometry has modified by these methods and obviously, the genetic algorithm code can reach the highest L/D ratio despite the more computational time. Also, the same source suggests evaluating objective functions to optimize the intended problem, as aforementioned in the previous paragraph (Sasaki et al., 2001).

3.1.2 Genetic Algorithm

The genetic algorithm is the most prevalent part of the Guided Evolutionary Algorithms. Holland (1975) first introduced this method with respect to the idea that relies on Charles Darwin's theory of the natural evolution for biological nature. The algorithm finds the best individuals with the aid of natural selection logic. The first stage of the natural selection process is the evaluation of the entire population and separating them. The population parents identified in here. As they mate with other parents of the current population, they leave their randomly mutated genes to their children. The better the parents have proper genes, the more likely the offspring will be to succeed. This process continues until the most appropriate individual is found.

With the increasing computational capabilities, analysis times remarkably decreased since the 1980s. These developments make the genetic algorithm accessible and useful in this field, especially for the two-dimensional wind turbine airfoils. This method has the individual generation cycle to find an optimized result. The scheme (Figure 3.1) can easily demonstrate the algorithm steps.

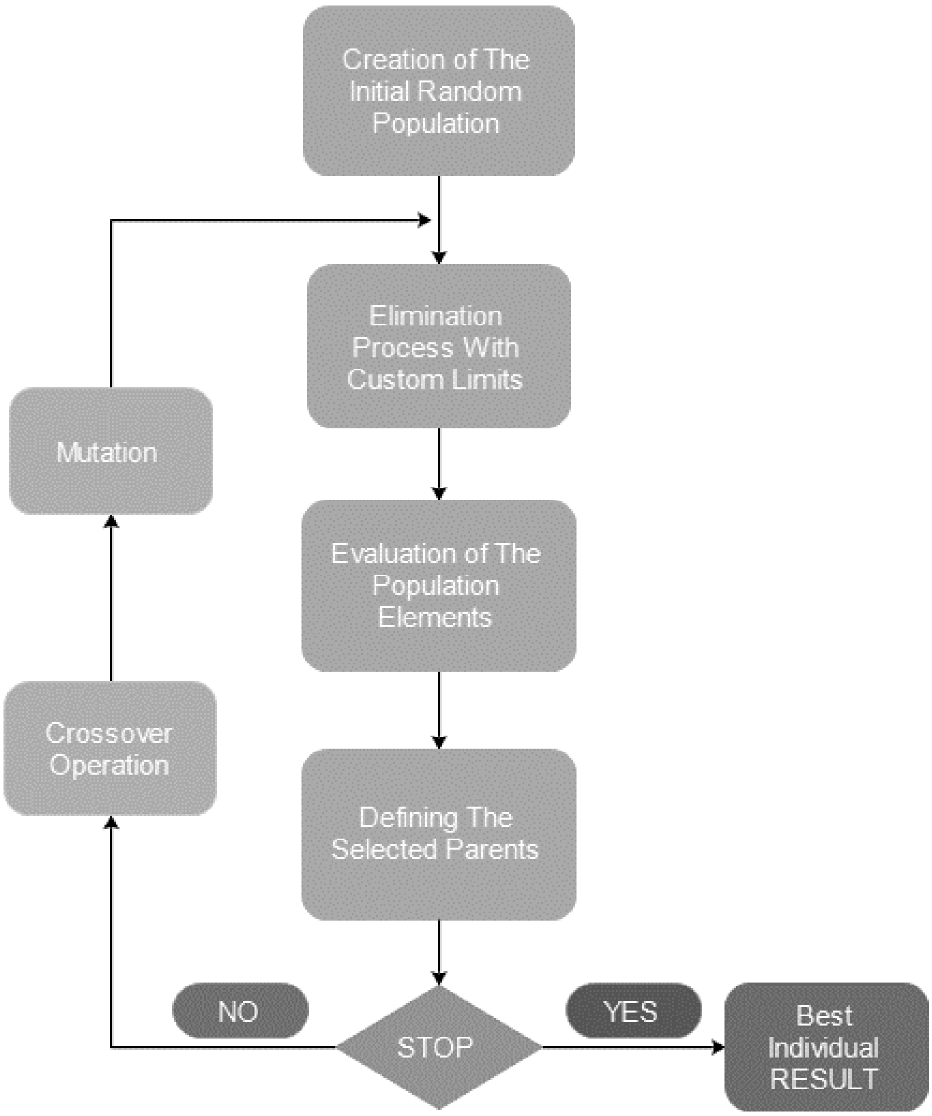

Figure 3.1 : Genetic Algorithm Standart Generation Cycle.

This cycle can be modified and expanded depending on the problem and the number of parameters can also be adjusted quickly. Without any sensitivity analysis, this method can search in discontinuous and nonlinear design spaces and they are not affected by the lack of irrelevant information. The reason for this is that the genetic algorithm generates the next populations based on a defined population rather than working with a single point. Thus, it can check the global domain rather than a local one. (Gardner et al., 2003)

Therefore, In this thesis, this method is chosen as the algorithm method. Like many modern genetic algorithm methods, a unique search method is created and used for the solve the problem of this study.

3.2 Initialization of The Population

This section is created to gain an initial solution set or population and clarify the design milestones from that originated product group to operations on the GA phases. GA algorithm takes office, mainly distributing the small genes to defined addresses while finding the fit chromosomes. As mentioned in the first stage of this process, variable numbers can be changed for every generation with modified parts. The code automatically alters the environment to understand how many population elements are sent to the solution calculation phase. The most valuable reason for this unknown search space, it is more likely to converge an output shape that is close to the real result among the randomly generated initial population consists of many elements than the sized population with a relatively low number of elements.

Consider a case; If the initial population is set to reach the final result with more population components, the completion time is known to be excessive than the other small-sized population groups that belong to the incoming populations. However, when this situation is maintained for all generations, it is determined as meaningless in terms of that excessive solution time. Such that, according to the subsequent generations, the analysis should be continued by lowering this number once at a reasonable rate (not in a local cluster) so that the global result can be reached in a short time. (Figure 3.2)

Figure 3.2 : Determination Chart for The Initial Population Infrastructure.

Among the infinite alternatives in space, the limits set for the ranges of the control points must be selected to scan the global domain in all elements and be simplified. Here, the determination of these ranges is not entirely under the control of the modifier, but with the "section curve number" option provided, geometries that are very close to each other but corresponding to different results in space can be created. In any case, it is suggested that this parameter be provided with three ribs and accordingly, the experiments in the thesis have been carried out with them.

An XY, XZ and YZ-plane-supported (1,2 and 3,4,5, respectively) curves (Figure 3.3) with 6 control points and random search limits of their structures are shown in space with the corresponding matrices. (3.12)

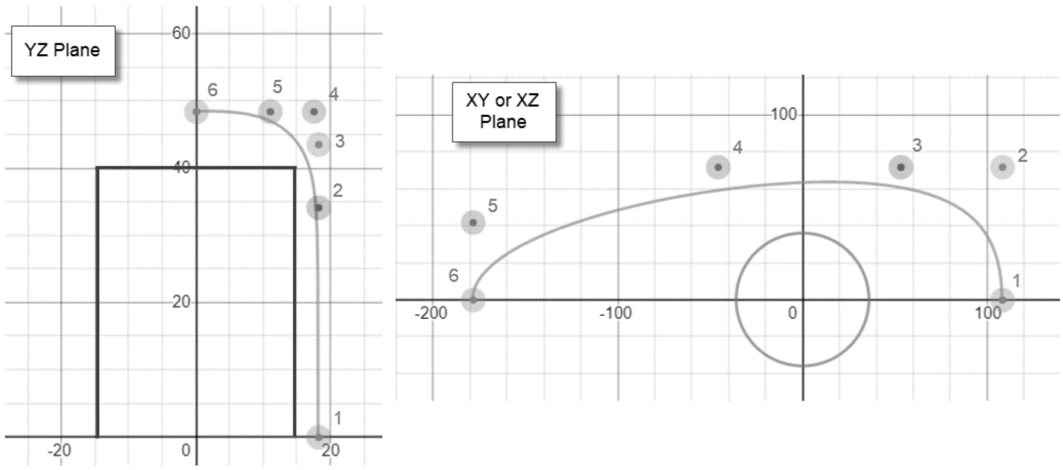

Figure 3.3 : Graphical Representation of the Sections (RHS: l_1,l_2 , LHS: l_3, l_4, l_5).

The 3,4,5 curves that are lieu on the every l_1 and l_2 combination is created from the bezier curve formulation and the first and last control points of l_3, l_4 and l_5 are derived. It can be observed easily; the x values are determined as the same thus, the interface is constructed on another YZ plane intrinsically. Quoted terms indicate the already procured terms by the Bezier calculations of l_1 and l_2 instantly for the current iteration.

$$l_{1,2} = \begin{bmatrix} x_0 & 0 & 0 \\ x_0 & 0, y_0 & z_0, 0 \\ x_1 & 0, y_0 & z_0, 0 \\ x_2 & 0, y_0 & z_0, 0 \\ x_3 & 0, y_1 & z_1, 0 \\ x_3 & 0 & 0 \end{bmatrix}, \qquad l_{3,4,5} = \begin{bmatrix} x_0{}' & 0 & z_0{}' \\ x_0{}' & y_2 & z_0{}' \\ x_0{}' & y_3 & z_0{}' \\ x_0{}' & y_0{}' & z_2 \\ x_0{}' & y_0{}' & z_3 \\ x_0{}' & y_0{}' & 0 \end{bmatrix} \tag{3.12}$$

Ranges of that parameters are also determined as below,

Table 3.2 : Random Generation Intervals of the Population Genes.

	x_0	x_1	x_2	x_3	y_0	y_1	$y_2{}^*$	y_3	z_0	z_1	z_2	$z_3{}^*$
Min	R	-3R/2	x_3	-6R	R/2	0	0	0	R/2	0	0	0
Max	2R	x_0	x_1	-2R	3R	y_0	y_3	$y_0{}'$	3R	z_0	$z_0{}'$	z_2

From Table 3.2, y_2 and z_3 values are found once and after that, for subsequent curves are generated with the different y_2 and z_3 that are divided by the specific ratios. These are also computed using the l_3's y_2 and z_3. Two different ratios are evolved such as; the first ratio is $(y_2/y_3)_{l_1}$ or the second one is $(z_3/z_2)_{l_1}$. Here, it is aimed to capture similar fluctuations for l_4 and l_5 considering these rates. Although efforts are made to prevent waves on the surfaces, if the number of ribs is higher, it will not be sufficient to prevent fluctuations by accepting the ratios as linear like defined. Besides, in the case where the number of ribs is more than three, the possibility of additional fluctuations that cannot be observed with the eye-control is increased unintentionally. Even if this situation remains in its current form, it will be eliminated in aerodynamic analysis, but it is aimed not to create these structures unnecessarily from the beginning and to complete the process efficiently without increasing the number of populations available.

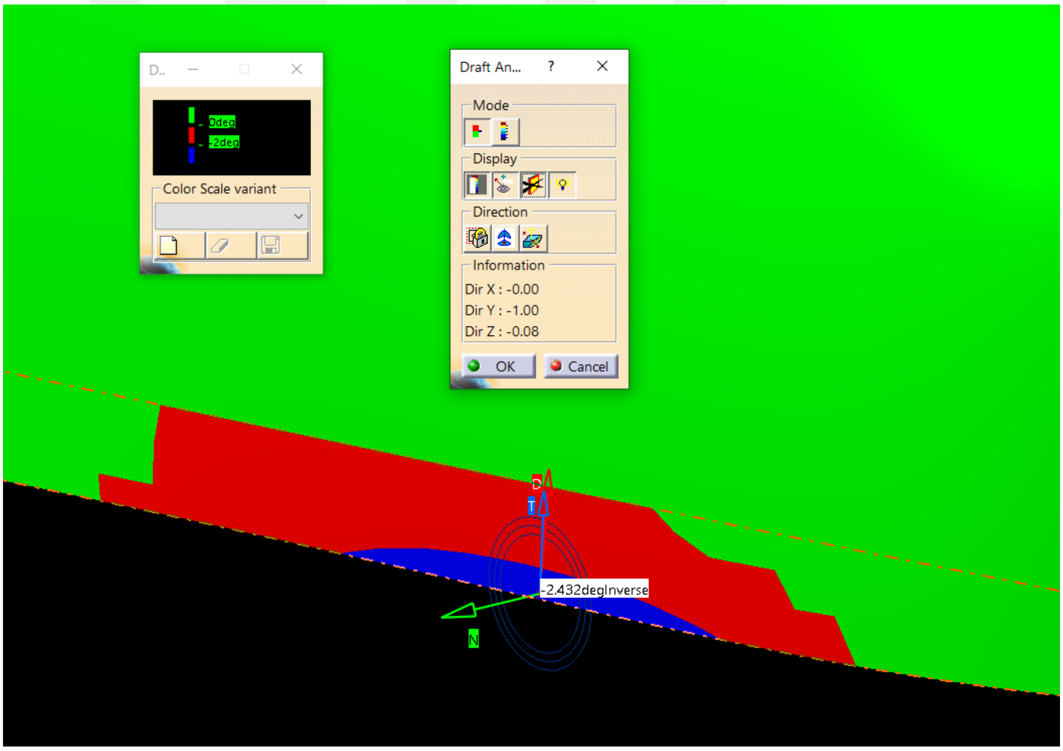

Figure 3.4 : Draft Analysis on an Example Surface.

There are various features in CAD programs for tracking these fluctuations in a standard design process. Specifically, the "Porcupine Curvature Analysis" and "Draft Analysis" commands in the CATIA toolbars help to reveal the undesired fluctuations visually and numerically. (Figure 3.4) However, due to this measure (tree lateral sections), no profile control was required in this direction during the optimization process.

Only the control of tiny disorder states on the resulting geometry will be achieved at the final stage. Otherwise, the negative angles associated with the mold production mentioned in the introductory section result in the difficulty of the part leaving from the molds and the part needs more than one mold consequently. This makes production complicated when the cost, vacuuming difficulties and sealing conditions are taken into account during the hand-lay up production process. All these reasons make it necessary to check that the symmetrically optimized radome cannot achieve a tangent transition with symmetry in the middle section and whether minimal deflections internal zones are within certain production tolerances.

All these reasons make it necessary to check some conditions before sending it to the manufacturing side, such as tangency with its other symmetric surface and improper profile tolerances that can be flexed by the contribution of minimal deflections.

3.3 Parent Selection

The number of parents determined at the beginning is of great importance for the next generations and it is essential to decide on a certain proportion according to the population number. Here, the determination of this number will detail the values that will come from the first iteration solution to meet certain conditions, and the grouping of the largest elements as much as this specified number will be detailed.

In addition to the significant intersection controls for Radom, many parameters affecting surface quality are also evaluated and play an essential role in parent selection. The user is also informed about which criteria the case cannot pass by encoding these values differently for each iteration. Details of the screening system here are addressed in 3.7. Each of the elements that pass this elimination part in the process until the beginning of the analysis process, creates an output file at the first stage according to the characteristic features and provides the primary inputs of the CAD geometries to be created in the future. In case the number of elements passed through these screenings at the beginning is less than the requested number of parents in one generation, the solution is terminated. Because continuing to evolve with a population that does not have a good enough individual can behave infertile in generating future populations. Because of this, the control mechanism in the code structure is raised.

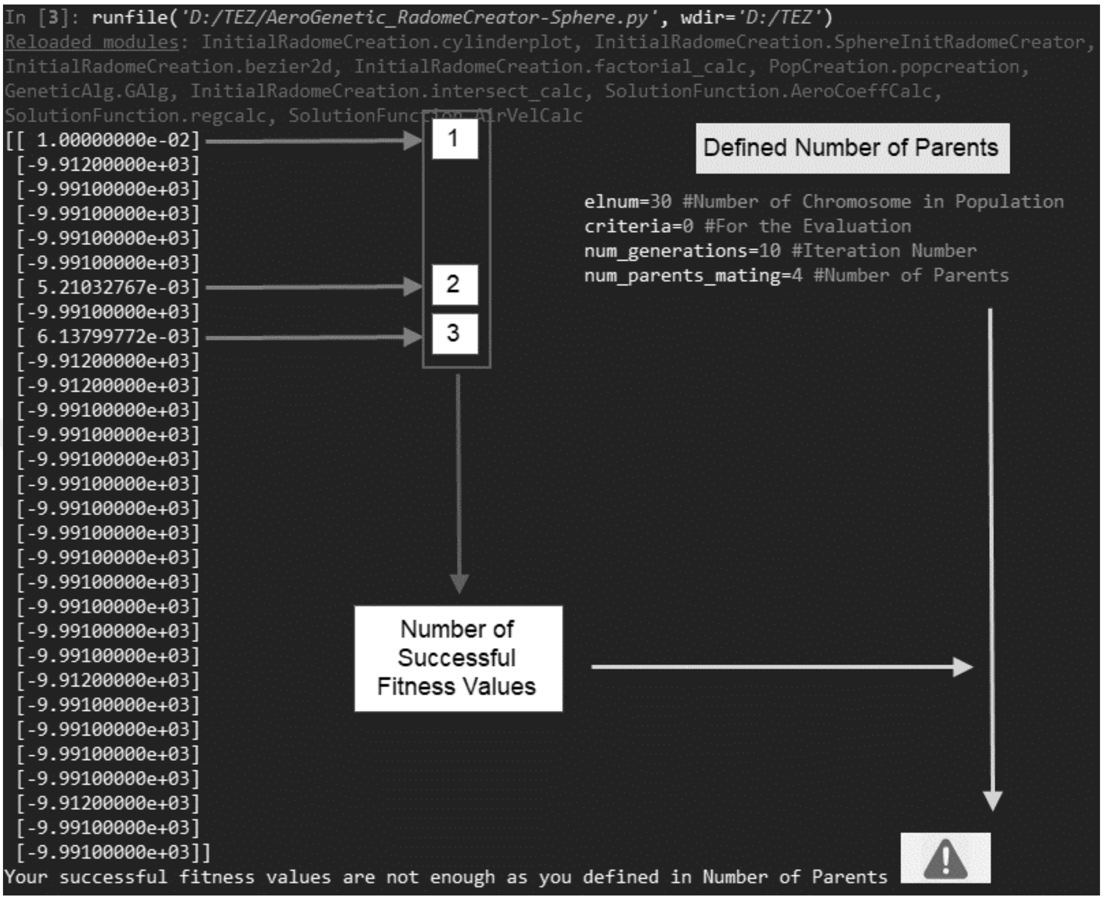

Figure 3.5 : First Iteration Failure for Population of 30 Elements and Termination.

When the result of the first batch analysis group of a 30 element population selected as an example in Figure 3.5 is evaluated, the algorithm; when it saw that the solvent number could not reach the required number of parents determined as a minimum of 4 pieces, it stopped the program as a result of the first iteration in order not to continue with an inefficient period and time loss. Here, the values of the negative elements in the fitness list provide information to the user about the reason for which the elimination algorithm is not suitable. Also, evaluations are made by comparing the similarity of the criterion value with the relevant element within the scope of the specified objective function. The element closest to the criteria value has the highest fitness value and is entitled to be a parent.

3.3.1 Determination of the fitness values and evaluation process

In the determination of fitness values, performing the solution by taking the criteria value as 0 in the equation (2.6) means that the maximum fitness value will be obtained in the smallest value of the current element to be evaluated. This value is the sum of the lift and drag coefficients as the solution function based on the thesis and it is understood from the k_1 and k_2 values in the equation (2.7), which are attained as 1.

As an added value in the evaluation process, an algorithm is introduced to the code structure that the parent elements that have already been solved for each iteration will not be resolved again, in this case, the solution time is shortened by around 15% and 20%. Therefore, just like the elimination criteria, the solution of the parents is done only within the context of the first and last generation. But better results from all other element evaluations are resolved as a new parent at each iteration.

```
if num_generations>ite>0 and i<=num_parents-1:
    fitness[i]=max_fitnesses[i]
    continue
```

Figure 3.6 : Exemption of Intermediate Solutions from Parents.

It was stated that some specific parameters of the produced radome geometries will be provided for the mesh algorithm and CAD program in the form of output without creating the radome drawings. It is critically attributed to specify the chord value and thickness value in the Y and Z directions from these parameters. As a valid reason, it is known that these values will take all the characteristic features of the domain from these three values during the domain creation process. In addition, the required velocity, density, Re number and reference area information are detailed in this output file and provided as input to the solver program. However, in order to create these values, the condition that the solution element is selected in accordance with the prerequisites. It has been found appropriate to use these flow parameters at the stage where the forces generated after the evaluated result are converted to coefficients. In this way, the system notifies the characteristic structures of the geometries that it creates at the beginning according to random values at certain intervals and calculates the elements of the comparison list using these parameters when the evaluation process is carried out.

3.4 Crossover Operation

The crossover process is defined as the recombination stage in the Genetic Algorithm. In other words, it is the birth process of each of the new individuals that two or more parents cross into. For stochastically produced new chromosomes, It is desired to select the genes coming from the gene pool of more than one individual selected as a parent by chance, and a new individual production takes place with an approach different from the cloning process. The 1st column of Figure 3.7 represents the non-altering genes of all parents while contributing to the new chromosomes of the children. For instance, in the case of this thesis, the 1st column of the population for each l_1, l_2, …, l_5 is the same because of the support plane similarity.

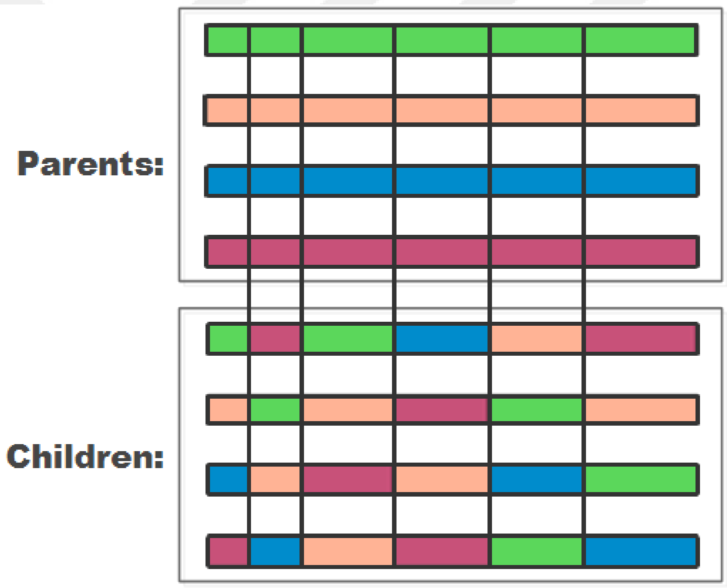

Figure 3.7 : Illustrative Basic Philosophy of Crossover Operation.

When this method applied to radome structures, only some of the genes that determine the character of the chromosomes are provided to these processes. According to the determined split location information, the pattern of the newly created individuals will be provided by their parents. The division of this number into the number of genes that will be subjected to crossover on a chromosome will reveal the solution path that reaches the globe by scanning correctly from the local stage during this search for the result.

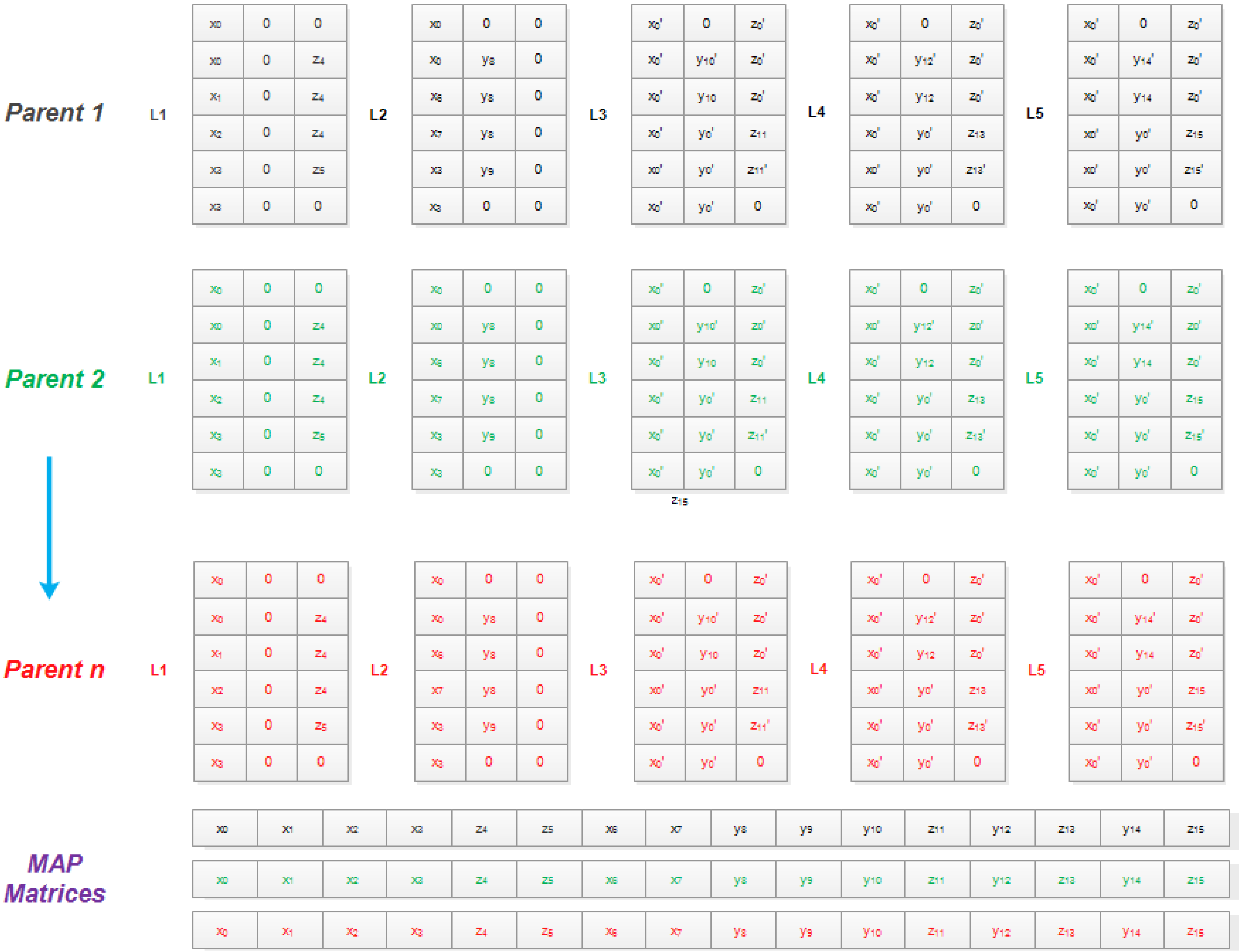

Figure 3.8 : Map Extraction from Parents.

From the created algorithm, all shared genes are collected from each parent chromosome and brought together in a single line. For example, let the first row and first column value for l_1 be the first part of this shared gene map (x_0). The next element is also get x_1 information from the same parent. If a split location of the algorithm solution is given as 2, the x_2 information to be selected or transferred from another parent. The most important rule is that at this stage, the selected l chromosome from different parents will serve the gene only for the same l of a new individual. The new gene map created by combining all the differentiated elements of these matrices and it does not deal with the Z coordinate of a point on the XY plane, which is 0 for this direction; also, other operations such as distribution and mutation are realized using this map. Besides, the number of genes to be subjected to crossover processing of these curves was determined as two, by applying the process of creating a certain proportion of the guide section curve coordinates that came to the agenda during the formation phase of the first population.

The main purpose of all these processes is to ensure the minimum time loss in the process of chromosome creation and the former good individuals selected as parents can efficiently present better individuals to the next generations by combining their powers from their valuable genes.

3.5 Random Mutation Algorithm

During the genetic algorithm process, chromosomes can reach acceptable generations by scanning the global better with mutations that create a random tweak effect in a limited number of genes. A Mutation algorithm can be designed based on a variety of methods, but some conventional mutation methods are preferred for the generic algorithm. A few of them are Dynamic Mutation, Schema Mutation, Compound Mutation, Clustered Mutation and Hyper Mutation Based Dynamic Algorithm. From these methods, the Compound Mutation Algorithm method is similar to the mutation algorithm of this thesis. Compound Mutation Algorithm is given as a method that can move away from the optimum local value and converge to the global result. However, as a disadvantage in this method, it can be shown that the number of mutations cannot be determined well. This part, which seems to be a disadvantage, is actually at a point that does not affect the solution of this thesis. (Patil & Bhende, 2014)

Table 3.3 is presented in which these methods are shown comparatively.

Table 3.3 : Different Mutation Types (Patil & Bhende, 2014).

Mutation Types	Features	Pros	Cons
Dynamic Mutation	Usage of Several Mutation Operators	Automatically choose appropriate mutation operator	Premature convergence problem.
Schema Mutation	Deals with premature convergence problem	It has an excellent wide range of constitutive property and maneuverability, also are superior to the ordinary genetic algorithm on computational efficiency and convergence stability.	The problem of local optimum
Compound Mutation	A specific strategy is used to avoid trapping into the local optimum.	1) Seek a better solution based on the contemporary population, 2) Keep the diversities of population, assure the further evolution of population and avoid local convergence.	Impossible to produce a suitable mutation number.
Clustered Based Adaptive Mutation	It produces a suitable mutation number adaptively and it guaranteed the higher survival rate of offspring in a selection operation.	Cluster Based GA chooses a suitable mutation number for decreasing the computing time and maintaining the population diversity to prevent premature convergence.	The problem of random search
Hyper Mutation Based Dynamic Algorithm	The Hyper Mutation Scheme adaptively adjusts the mutation rate during the run of GA. The diversity of GA can be maintained.	Two different types of Hyper Mutation Scheme to increase the performance of GA.	The hyper-mutation GA where the mutation rate is gradually increased is not suitable for the problem

A Compound Mutation-like mutation algorithm is planned to be implemented and coded on the gene map created in the offspring stage before distribution occurs. The mutation probability of all elements in the map matrices given in Figure 3.8 is determined by the condition of maintaining the value in a given random range. For the element to which mutation will be applied, the determination of the value is also performed by selecting a random range of function based on the cylinder radius value inside.

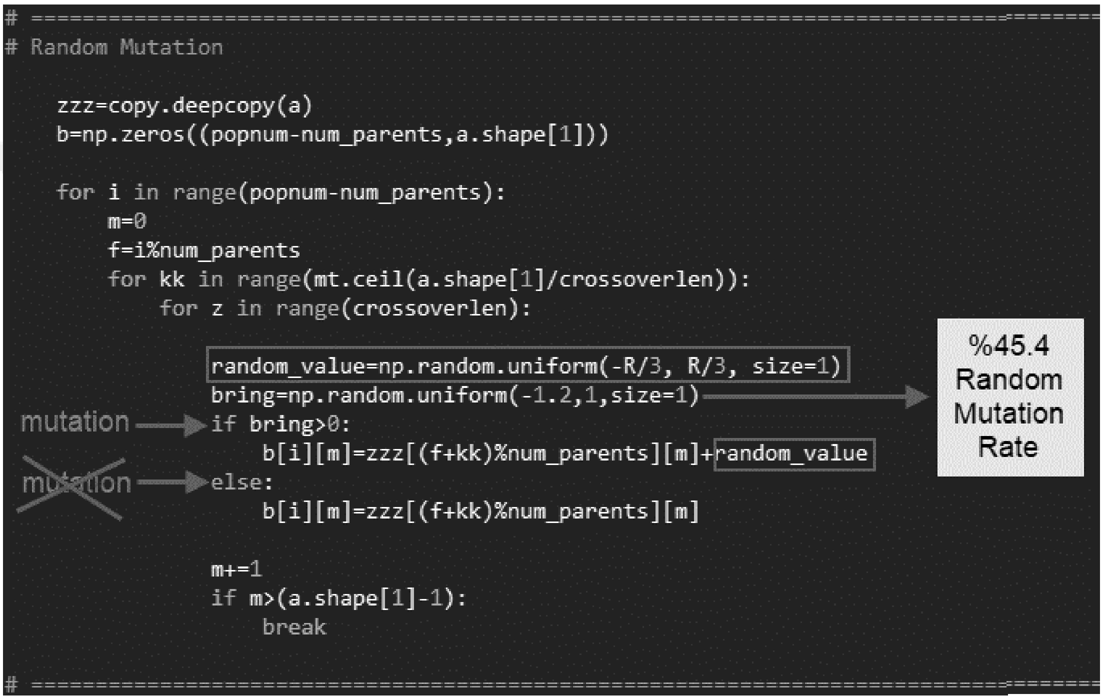

Figure 3.9 : Definition of The Random Mutation.

For the selection of the random mutation rate, while it is already known that the number of mutations cannot be adjusted, it has been obtained from the conducted experiments that the mutation rate must be in the range of 50% and 40% to be productive. These experiments involve the processes that sweep the structure geometrically to an individual character and do not need long CFD solutions. For example, in an experiment carried out, only when the formed surface is examined longitudinally, the closeness of the control points at the front and back to the cylinder structure was evaluated. According to these trials, it was evaluated that it would be appropriate to have the mutation rate in this specified range. In the current situation, when the Compound mutation method is applied, it is known that the mutation rate and value ranges will be advantageous in terms of approaching the solution in less iteration. The values in Figure 3.9 have been determined by performing quick trials in this context.

3.6 Determination of The Iteration Numbers

To govern the number of iterations, the crossover logic must first be organized and the variables in the mutation algorithm must be frozen. It was mentioned that the values included in the mutation algorithm would directly concern the number of iterations in order to achieve the final value properly.

In this section, solution trials have been made as stated by the information of different objective functions and in these cases where the number of parameters related to control points on geometry has not been changed for each, analysis results have been shared according to these different test functions. The minimization of the frontal border, which is accepted as the first one and again minimizing both frontal and aft borderline that is constructed as the second objective function are compared. The gathered knowledge from that set of analyses is declared that the number of control points, valid coordinates and chromosomes were the compulsory and most substantial actors for every set of iterations. Where multiple solutions are made for each condition, the number of populations, number of parents and number of iterations are tested in an adequate diversity environment. Thus, not only the number of iterations but also the required number of parents and the number of populations are determined well.

When a time-based evaluation is carried out, only the increase in the number of elements according to the formation of domain size can make these conditions uncontrolled. Even in this case, the number of iterations, the number of populations and the number of parents are correctly determined in the GA process, but the pre-estimates of the analysis time depend directly on the objective function in CFD.

To be more explanatory and precise, the results of the test case analyses are included in the two tables with their abundant trials. Within the confines of these analyses made according to the values given in Table 3.4 and Table 3.5, fitness changes were evaluated as a percentage.

Table 3.4 : Fitness Results of The Frontal Limitation Test Cases.

Test Case	Trial #1 Fitness	Trial #2 Fitness	Trial #3 Fitness	Trial #4 Fitness	Max ΔFitness/ Fitness%
50 population elements, 40 iterations, 7 parents (1A)	0.0245	0.02457	0.02522	0.0249	2.93
40 population elements, 20 iterations, 6 parents (2A)	0.0245	0.02001	0.02358	0.0233	22.43
200 population elements, 60 iterations, 30 parents (3A)	0.0258	0.02572	0.026	0.0258	1.08
$\frac{\lvert(3A)-(1A)\rvert}{(3A)}\%$, $\frac{\lvert(3A)-(2A\rvert)}{(3A)}\%$	5, 5	4.4, 22.3	3, 9.3	3.4, 9.6	

Table 3.5 : Fitness Results of The Aft and Frontal Limitation Test Cases.

Test Case	Trial #1 Fitness	Trial #2 Fitness	Trial #3 Fitness	Trial #4 Fitness	Max ΔFitness/ Fitness%
50 population elements, 40 iterations, 7 parents (1B)	0.03044	0.03146	0.03192	0.0303	5.34
40 population elements, 20 iterations, 6 parents (2B)	0.02887	0.0308	0.02959	0.0276	11.59
200 population elements, 60 iterations, 30 parents (3B)	0.03237	0.03247	0.03228	0.03246	0.58
$\frac{\lvert(3B)-(1B)\rvert}{(3B)}\%$, $\frac{\lvert(3B)-(2B)\rvert}{(3B)}\%$	5.9, 10.8	3.1, 5.1	1.1, 8.3	6.6, 14.9	

When the test case solutions are evaluated, it is seen that the configuration (2) is not sufficient to reach the correct result, as opposed to the results obtained from (1) and (3). It is understood that the (3) configuration has the disadvantage that the solution time is very high and the high number of unnecessary elements are solved in (3). Therefore, regardless of the objective function, it is found that the same configurations reflect similar outputs in the environment where the control parameters are kept the same. In the optimization algorithm based on the CFD solution, where the objective function information comes from the c_L and c_D values, it is envisaged to perform analyses by increasing the number of iterations and the number of population elements at least 10% conservatively. In addition, the fact that the one above related to the first iteration consists of the solution of more population will provide some protection. However, when the tables are justified carefully, increasing in the number of parents is being non-effective to facilitate finding close fitness values. For this reason, the algorithm in the thesis will be solved without much increase in the number of parents.

Whether the current assumptions are consistent or not will be revealed by plotting fitness graphs in the results section. However, as expected, as a result of the evaluation of fitness values on the basis of Lift and Drag forces, there will be differences that the design will not change in the forces since the geometry optimization will also be terminated here and the aim which is to obtain the geometrically optimized surface shape is maintained already.

3.7 Geometric Element Elimination

In addition to the process of determining the parents according to the inputs from the CFD result in the elimination process, it is necessary to grade the structures as worst or not before sieving them according to their geometric properties and passing them to the solution stage with this. In this way, a severe reduction in solution time can be achieved. However, the shape elimination processes of these geometries created in 3 dimensions are either additional items that will come from the limitations arising from production as stated in the introduction part or it is already the process of recognizing and sieving a shape that will cause deterioration aerodynamically.

In cases where the multi-section curves used by CAD programs are sweep between each other and produce a holistic surface, various draft analyses should be performed and mold-part incompatibility and removal-assembly convenience status should be revealed for each surface. (Figure 3.4) Of course, this process will be applied only to the list with the most recent geometries, since there is no need to automate this section in this thesis. The most efficient and productive parts are determined aerodynamically via using the geometric eliminations.

3.7.1 Additional limitations

In this subchapter, the mentioned elimination types are classified in detail. As the first elimination criterion, the condition where the cylinder and the surface intersect was considered. The elements remaining from this elimination are stamped with -9991 fitness value. This 1st condition is used to remove the elements forming an intersection with the cylinder for five curves (Figure 3.8) created in 2D and attain the fitness values directly in this aspect. (Figure 3.10) The 2nd condition with a -9992 fitness value is the condition where the negative y values in all curves that may occur as a result of mutation are eliminated. The fitness values of other elimination lines are similarly in negative 999X format.

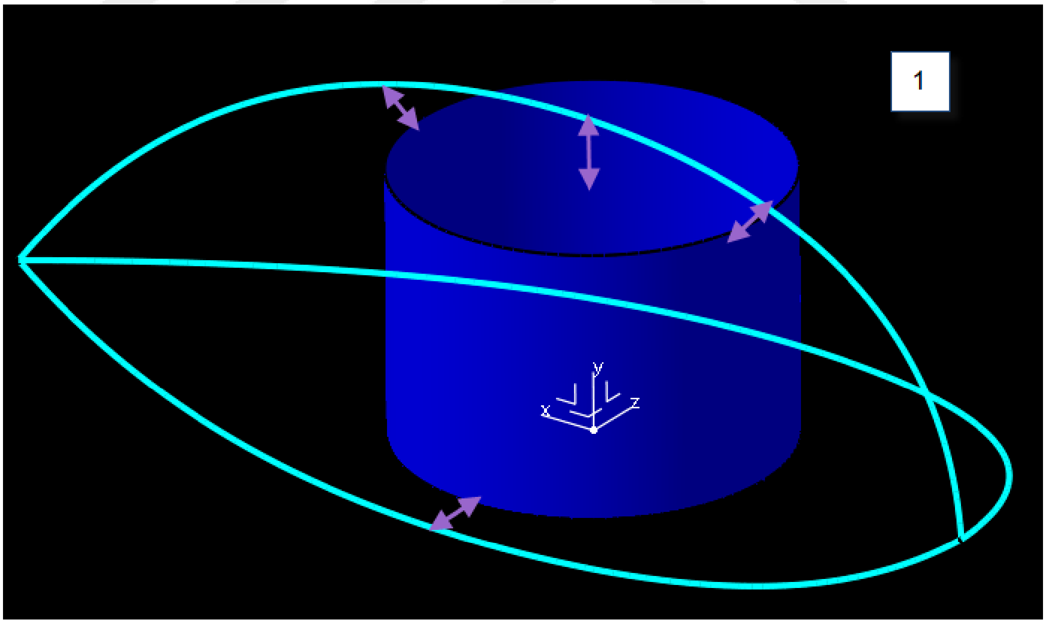

Figure 3.10 : 2D First Elimination Criteria Visualization (1).

If a population element that cannot pass the 3rd and 2nd conditions continue to the surface formation phase, the termination of the system will be faced since the surface cannot be created from the formed curves inappropriately. For example, when the surface formed in the third condition produces a product with an intersection point in itself, it becomes impossible to create a surface from curves. Screening conditions numbered 4, 5 and 6 are the arbiter that will prevent the creation of wavy and rough surfaces. These conditions, which are currently not eliminated here, will likely be eliminated during the CFD solution phase. The last condition, which is the 7th condition, is to control the front, aft and top side borders again and eradicate chromosome genes of defective population elements that come from mutations.

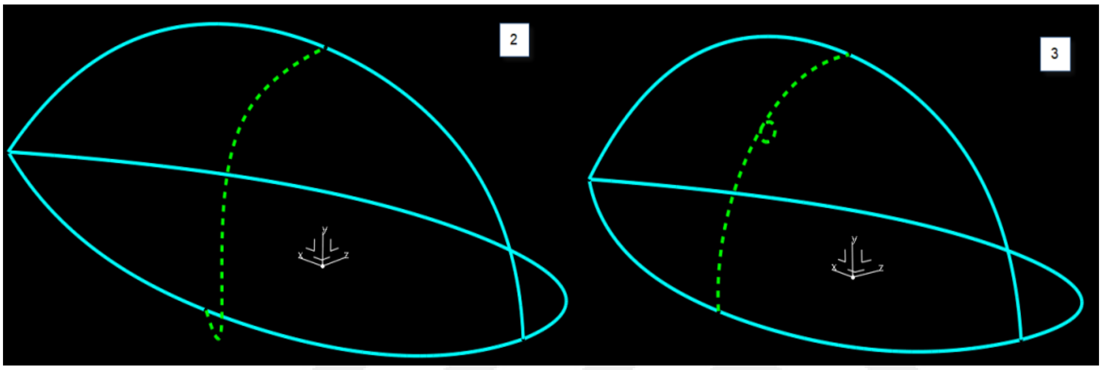

Figure 3.11 : Prevention of the Termination, Criteria (2), (3).

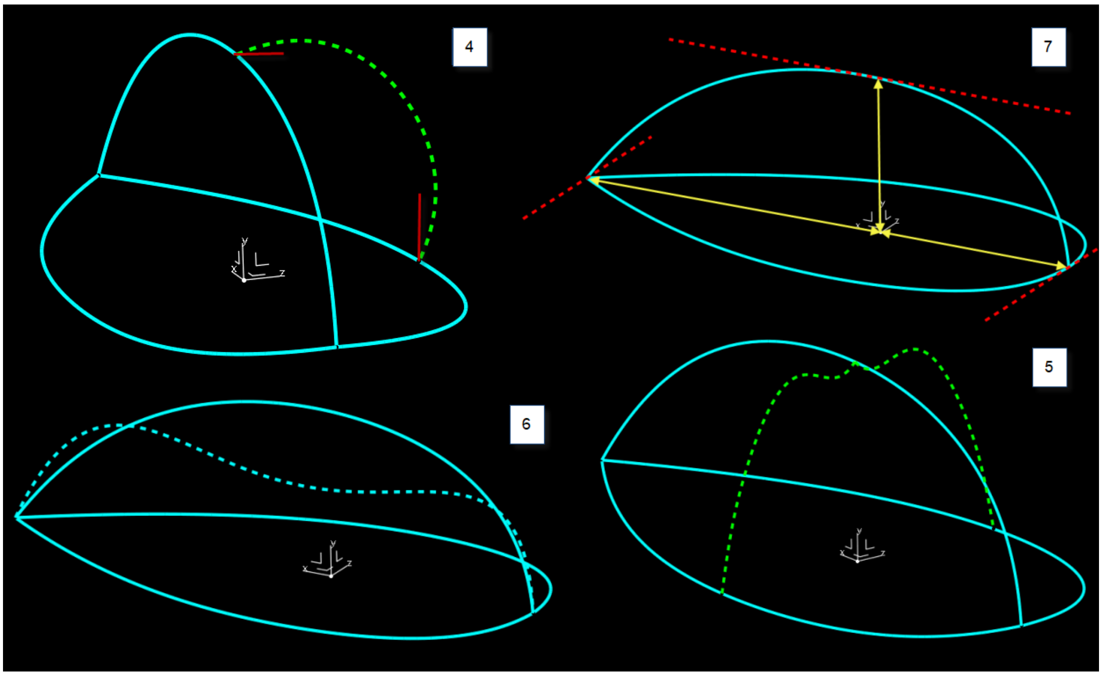

Figure 3.12 : Suppression of the Wavy Surface, Criteria (4), (5), (6), (7).

Despite all these eliminations, there is still the possibility of a product with a structure that intersects with the cylinder inside. To understand this, a screening benchmark is run for the last time on all valid elements without exception. This criterion creates a new part using the created CAD surface geometry with the script code in CATIA and performs a 3D intersection analysis considering the cylinder dimensions. After evaluation, if the result is assigned as eligible, the domain creation phase is started.

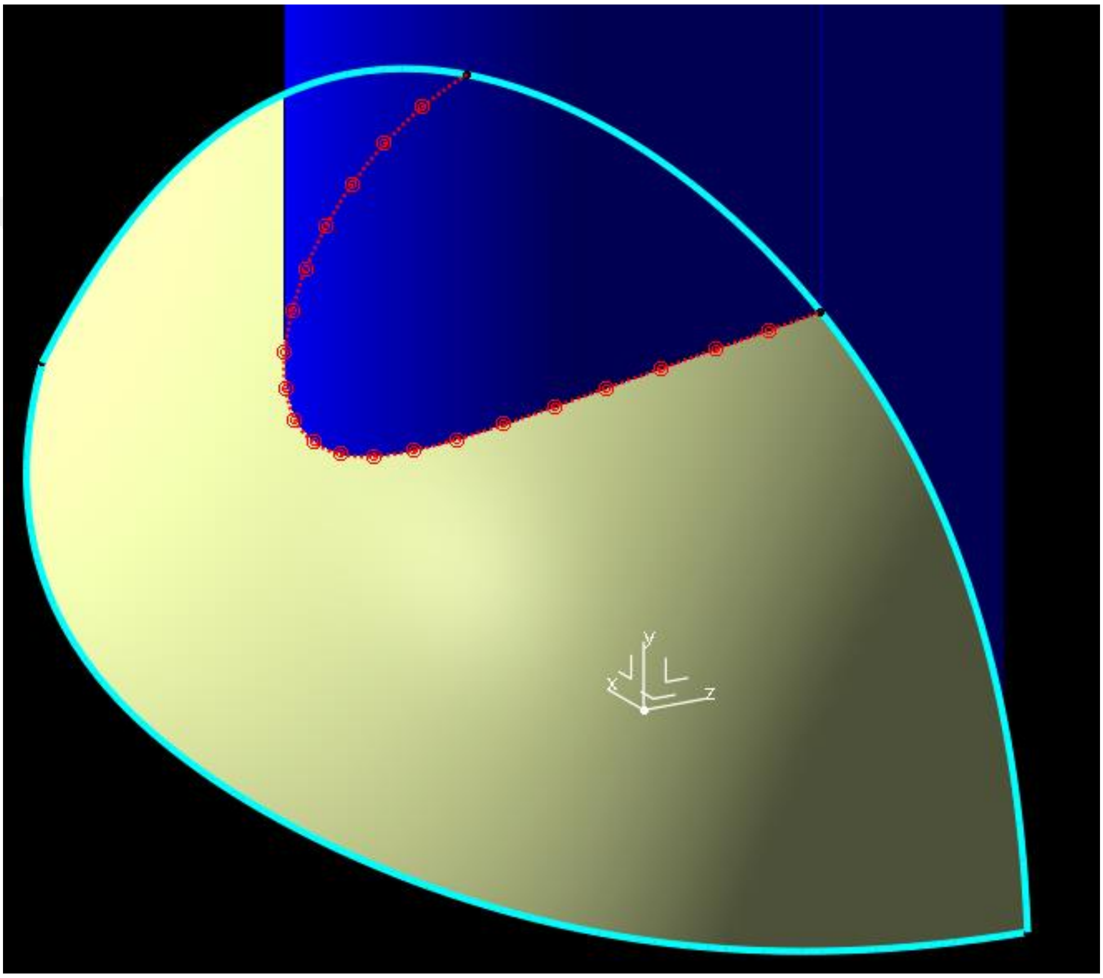

Figure 3.13 : 3D Intersection Computation of the Radome Surface.

While doing this, the cylinder height whose intersection is calculated is selected in infinite length ($>>$ H). Thus, the elimination is performed by comparing the heights of the intersection points obtained as discretized with H. (Figure 3.13)

4. DETERMINATION OF THE RADOME DOMAIN AND MESH CREATION

Up to this section, information was given about the air properties and shape evolve studies. In 4th Chapter, the details of mesh and domain creation processes according to the finite volume method for CFD analysis of population products that came from GA processes to the final stage and successfully passed through the screening stages will be discussed.

Details of how the surface and domain boundaries are determined are given as subtitles. Also, for the domain sizes determined or solution areas of different widths and heights that may occur, a grid convergence study in which many parameters such as adequate mesh count, boundary layer mesh thicknesses are examined and presented.

4.1 Radome Surface and Domain Creation

The stage of forming the Radom surface was carried out for many populations in the GA process, given in Chapter 3. CFD Solution is a decision-maker that calculates how much fitness value will be in the new parent list after passing the elimination process needs a domain to solve. This domain is created for each solution alternative automatically and placed in the 3rd stage of the CAD program, where the other stages are created for the only radome surface genesis.

The dimensions of the domain, which resembles the prism of rectangles, are linked with the internal dimensions of the radome. The reason for this is that the domain that will be created automatically can has compatible dimensions with its own radome. The distance ahead in the creation of the domain is critical for the development of the boundary layer because the bottom domain surface under the radome is modelled as a solid wall. Therefore, the developing boundary layer effect will produce different results at different frontal distances. Grid Convergence analyses were carried out so that the distance between the domain inlet wall and the radome leading edge is 7 times the chord value. Mesh properties are determined and the domain creation criteria of the radomes are realized according to these parameters.

Although the leading edge - inlet distance is decided as $7\ x\ sphere\ chord\ (C_x)$ value for the case, the side and back distances are assessed according to the convergence state of the numerous grid analyses with the same parameters. (Table 4.1)

Table 4.1 : Determination of the Side and Aft Dimensions for the Radome Domain.

Case No	a_1, a_2, a_3 or a_4	b_1, b_2, b_3 or b_4	Mesh size Radome max/min (Growth Factor)	Mesh size Towards to Far-Field min/max (Growth Factor)	Total Layer Height (cm)	Last Layer Height (cm)	No. of Mesh
1	$7C_x$, $7C_x$, $7C_{z,y}$	$2.5C_x$, $3.125C_x$, $3C_{z,y}$	1/1.5 (1.15)	1.5/55 (1.15)	13.31	1.85	0.521M
2	$7C_x$, $10C_x$, $10C_{z,y}$	$2C_x$, $2.5C_x$, $3C_{z,y}$	1/1.5 (1.15)	1.5/55 (1.15)	13.31	1.85	0.543M
3	$7C_x$, $10C_x$, $7C_{z,y}$	$2.5C_x$, $3.125C_x$, $3C_{z,y}$	1/1 (1.15)	1.5/55 (1.15)	13.31	1.85	0.869M

All analyses performed in Table 4.1 were performed with the same mesh size properties and layer thicknesses. In addition, the box refinement grid structure created around the radome has very similar properties. The a and b dimensions in here are being meaningful if Figure B.1 and Figure B.2 are examined.

For Case 1, Lift Force was calculated as 628.44N and Drag Force as 62.35N. Here, especially Case 2, is used to reveal the effects of increasing distances to the sides and to the rear in the domain, compared to this 1.Case result. As a result of Case 2, 624.07N Lift Force and 61.94N Drag Force were calculated. According to these results, it was evaluated that the lateral change did not affect the solution after a certain distance.

Comparison of Case 3 results with Case 1 is handled to examine the effects of the only rear distance without changing the mesh properties for the grid refinement box structure around the radome. The aim of this box comes from the required sufficient turbulence observation capacity in a more frequent mesh structure. The lift force value of Case 3 was calculated as 631N and Drag force value as 61.45N.

Final differences in percentage between Case 1 - Case 2 and Case 1 – Case 3 forces remain under 2. The situation can be assigned as stationary for these parameters within these cases. As a result, in the light of the information obtained from the calculations, it was decided to continue with the domain dimensions and refinement box dimensions in Case 1.

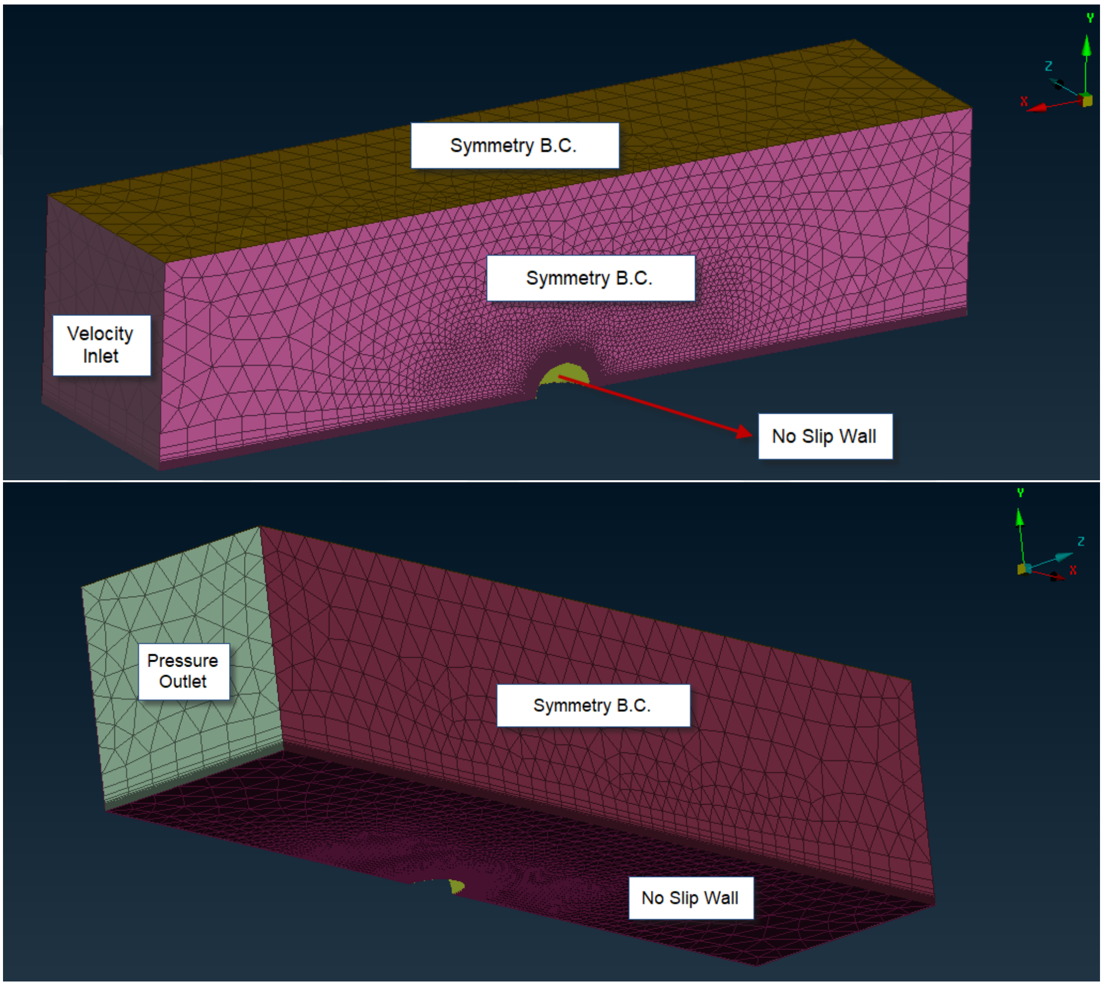

Figure 4.1 : Boundary Condition Types of A Schematic Domain.

The boundary conditions properties of other domain walls were created by making use of the symmetry condition. The boundary conditions of all walls are expressed in the image Figure 4.1.

4.2 Grid Convergence Analyses and Final Mesh Properties

The grid convergence analysis sequence with simultaneous processes and the analyses required for determining the domain boundaries are expressed as part of the same study thoroughly. The most important reason can be explained in that, the domain size cannot be determined in terms of insufficient grid number and resolution, it also requires very conservative domain measurements in determining the number of grids by analysis without determining the domain dimensions, and this situation increases the solution times considerably. Therefore, this study follows a combined group of analyses that include all the decision type items about domain size and grid density.

One of the results of the three analyses mentioned in Table 4.1 is actually the result of the initial hemisphere solution in the real case. However, to attain the mentioned property set as the final one, many analyses with coarse and fine mesh sizes in several domains were performed manually and their differences were revealed in section 4.2.2 . This work has been described as the grid convergence study that contemplated with some dioristic layer properties and layer sizes also.

To identify the mesh properties of the boundary layer correctly, the estimated first cell center, estimated first layer height and total boundary layer thickness distances are determined according to the velocity, density, viscosity and reference length information found out according to a predicted target y^+. In section 4.2.1, this y + forecast, the definition of y + and what this concept wants to convey are detailed.

4.2.1 y+ calculation

The value of y^+ is a non-dimensional and virtual distance between the wall and first mesh node defined in various turbulence models, which allows the flow prediction in the CFD methods accurately. In a typical process, to properly understand the flow field properties, whole computational solution must be realized. However, the y^+ value prediction is used for minimizing the risk of the wall treatment error. The mesh structure is reshaped by the y^+ term and using equation (4.1), y (wall distance) is found for the first node a little far away from the wall.

$$y^{+} = \frac{\rho U_{\tau} y}{\mu} \tag{4.1}$$

But in the first stage, it should be understood whether the flow is turbulent or not and This value is checked for external flow by calculating Re. Then, U_{τ} has to be calculated for equation (4.1).

$$U_{\tau} = \sqrt{\frac{\tau_w}{\rho}} \quad where, \quad \tau_w = 0.5 C_f \rho {U_{\infty}}^2 \tag{4.2}$$

Equation (4.3) is followed to calculate the C_f;

$$C_f = \frac{0.058}{Re^{0.2}} \tag{4.3}$$

By returning to equation (4.1), the y value is calculated for the estimated y^{+}. Thus, estimated wall distance is found.

In order not to calculate incorrect velocity and pressure distribution due to the wall functions of the turbulence model, the value of y^{+} must be in the logarithmic layer range. In accordance with the wall modeling strategies, the y^{+} estimation must be in the range of minimum 30 and maximum 300 for the selected turbulence model. Turbulent boundary layer regions are detailed in Figure 4.2 and Figure 4.3.

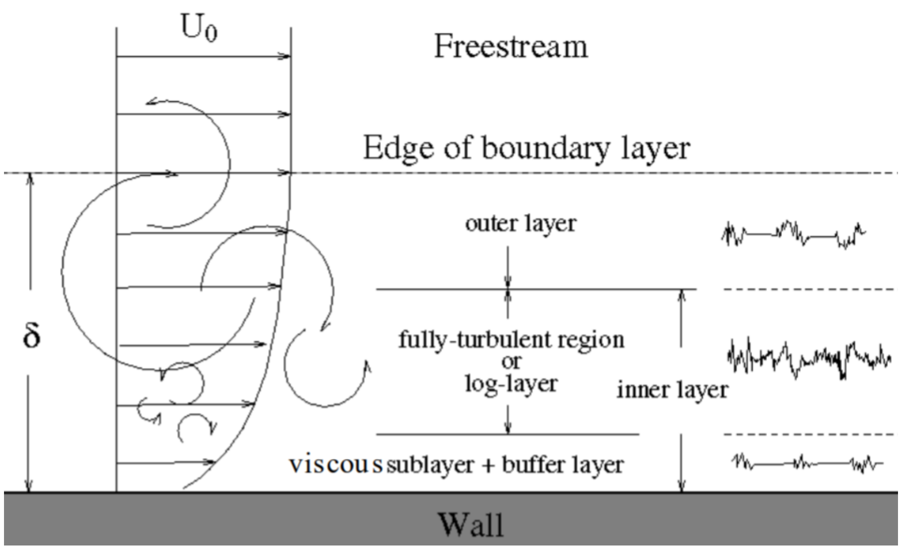

Figure 4.2 : Turbulent Boundary Layers (ANSYS, 2014).

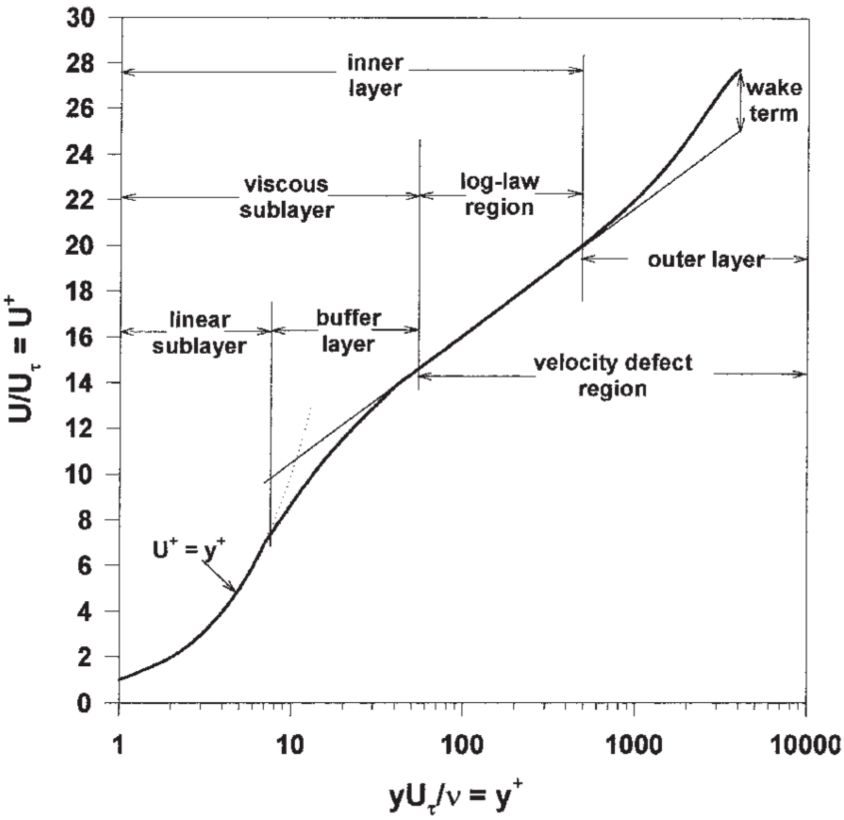

Figure 4.3 : Non-Dimensional Velocity Profile in Different Layers (Schultz et al., n.d.).

Considering all these issues, it was decided to include the value of y^+ as 200 and as a result of the calculations, it was revealed that the value of the first cell height (y) should be between 0.2 mm and 2 mm. In the current estimate, the y value is calculated as 1.34 mm.

4.2.2 Grid convergence results

Until this subchapter, whole the domain specifications are attained nearly, but one of the most critical parameters is not finalized up to here. This parameter states the mesh density of the domain and affects the computational time with already frozen variables that again belongs to the domain.

Some particular examination ways are developed for the spatial grid convergence studies, but the main target of this chapter, finding the best convenient grid fidelity while comparing with the finest grid resolution using the randomly selected cases. Based on the logical foundations, the cases are created by taking into account the critical variables to reduce from the finest one.

They are defined in the same specific growth rate, and these grid sizes are placed in box and whole domain of radome and its own surface. Details of all analysis items are reflected in Table 4.2.

Table 4.2 : Properties of Grid Convergence Analyses (Hemi-Sphere Radome / Half, Symmetrical Domain).

Case No	a_1, a_2, a_3 or a_4	b_1, b_2, b_3 or b_4	Mesh size Radome max/min (Growth Factor)	Mesh size Towards to Far-Field min/max (Growth Factor)	Max Box Mesh Size	Layer Growth Factor	First Layer Height (cm)	Total Layer Height (cm)	Last Layer Height (cm)	No. of Mesh	Lift Force (N)	Drag Force (N)
1	$7C_x$, $7C_x$, $7C_{z,y}$	$2.5C_x$, $3.125C_x$, $3C_{z,y}$	1/1 (1.2)	1/40 (1.2)	10	1.15	0.13	13.31	1.85	0.844M	633.46	61.47
2	$7C_x$, $7C_x$, $7C_{z,y}$	$2.5C_x$, $3.125C_x$, $3C_{z,y}$	1/1 (1.2)	1/40 (1.2)	10	1.15	0.13	13.31	1.85	0.435M	635.28	60.71
3	$7C_x$, $7C_x$, $7C_{z,y}$	$2.5C_x$, $3.125C_x$, $3C_{z,y}$	1/1 (1.2)	2/45 (1.2)	10	1.15	0.13	13.31	1.85	0.175M	618	64.7

4	$7C_x$, $7C_x$, $7C_{z,y}$	$2.5C_x$, $3.125C_x$, $3C_{z,y}$	1/1 (1.2)	1/60 (1.2)	12	1.15	0.13	13.31	1.85	0.440M	636	60.9
5	$7C_x$, $7C_x$, $7C_{z,y}$	$2.5C_x$, $3.125C_x$, $3C_{z,y}$	1/1 (1.2)	1/55 (1.2)	12	1.15	0.2	13.01	1.87	0.385M	624.5	66.28
6	$7C_x$, $7C_x$, $7C_{z,y}$	$2.5C_x$, $3.125C_x$, $3C_{z,y}$	1/1 (1.2)	1/55 (1.2)	12	1.15	0.11	13.07	1.8	0.450M	640.2	58.25
7	$7C_x$, $7C_x$, $7C_{z,y}$	$2.5C_x$, $3.125C_x$, $3C_{z,y}$	0.5/0.5 (1.2)	0.5/55 (1.2)	12	1.15	0.1	13.76	1.88	1.47M	641.7	59.08
8	$7C_x$, $7C_x$, $7C_{z,y}$	$2.5C_x$, $3.125C_x$, $3C_{z,y}$	1/1 (1.15)	1/20 (1.15)	5	1.15	0.11	15.14	2.07	1.87M	632.02	60.5
9	$7C_x$, $7C_x$, $7C_{z,y}$	$2.5C_x$, $3.125C_x$, $3C_{z,y}$	1/1 (1.2)	1/55 (1.2)	10	1.15	0.13	13.31	1.85	0.521M	628.44	62.35

In addition to the analyses performed, the skewness of all analyses and angles of the elements are also checked. A script section that controls and corrects these values has been added to the automated mesh algorithm. This script ensures that 3D off elements cannot be accommodated within the domain after the volume mesh is created.

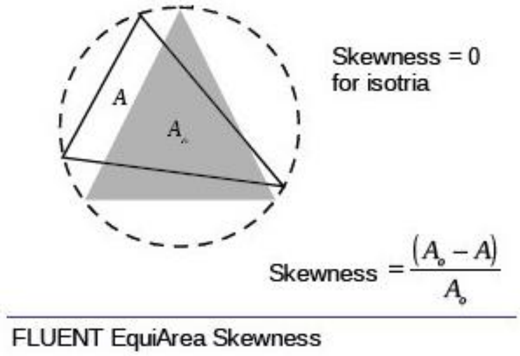

Figure 4.4 : Description of The Skewness (ANSA Commercial Software).

Results of cases numbered 1.7 and 8 are very close to each other and calculated using fine grid properties. For all cases, calculations were made using the same turbulence model and the same CAD geometry but, different experiments were carried out for the boundary layer in accordance with the previously determined 0.2 mm and 2 mm first layer thickness rule.

When the forces are examined, it is decided to continue the analysis with Case number 9 by considering the mesh number, boundary layer properties and grid densities of the other refinement box structure together. For Case 9, which seems to have minimal differences from the real situation, considering that CFD solutions will already be used in a comparative way for lift and drag coefficients, the small errors for this Case 9 can be ignored with that. Despite these small errors, the most useful properties are selected for Case 9 with a minimum number of mesh elements. (0.521M)

5. CFD METHOD AND VALIDATION OF THE SOLVER

Computational aerodynamic solutions are the main center of the evaluation phase, where fitness values will be obtained for this thesis. These values are run only for one specific condition determined. The main reason for this is that the specified aircraft usually operates at a fixed altitude and a constant velocity. It is the subject of this Chapter how to calculate these previously determined values. In general, the classification of flow problems and the approaches to be solved within the domain are summarized. It is planned to make calculations using the script created for ANSYS Fluent program. K-ε turbulence model is used in solutions realized using RANS equations. Because there are nonlinear coupling problems between the radome surface and viscous effects. The details of all are epitomized in this chapter.

5.1 Computational Fluid Flow Solution Methodologies

As the nonlinear PDE set, Navier Stokes equations represent the one at the top of the flow model charts (Peerlings, 2018) with the highest precision and their methods generally based on the Eulerian perspective. The main difference from the lagrangian approach is the observation way of accelerations and the forces acting on a fixed point in the control volume, rather than the moving particle. (Figure 5.1)

Basically, these equations can be used with viscous, compressible and unstable flow properties. The Reynolds number value of the problem in this thesis, defined as $Re \cong 3.89\ x\ 10^6$ and the problem shows turbulent flow characteristics for the external flow.

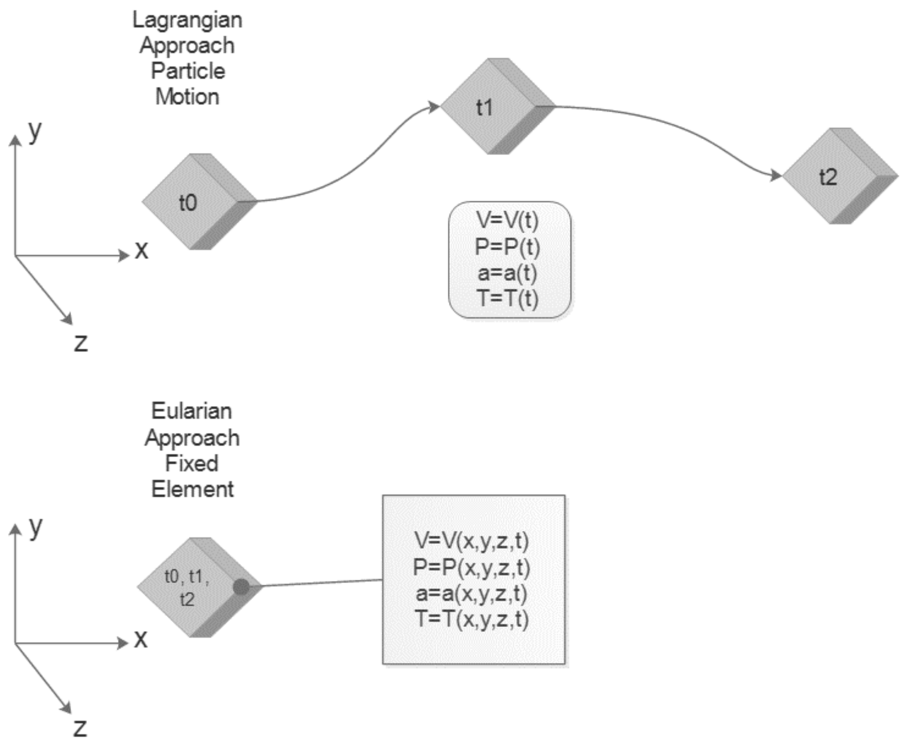

Figure 5.1 : Eulerian and Lagrangian Approaches.

Navier Stokes equations consist of three parts; these are commonly known as the momentum equation (Newton's second law of motion), continuity equation (Conservation of mass) and energy equation (Conservation of energy). (5.1) , (5.2) , (5.3) , (5.4) , (5.11) (Anderson, 1995)

$$Continuity\ Equation:\ \frac{\partial \rho}{\partial t} + \frac{\partial(\rho u)}{\partial x} + \frac{\partial(\rho v)}{\partial y} + \frac{\partial(\rho z)}{\partial z} = 0 \tag{5.1}$$

$$X - Momentum:\ \frac{\partial(\rho u)}{\partial t} + \frac{\partial(\rho u^2)}{\partial x} + \frac{\partial(\rho uv)}{\partial y} + \frac{\partial(\rho uw)}{\partial z} = -\frac{\partial P}{\partial x} + \left(\frac{\partial \tau_{xx}}{\partial x} + \frac{\partial \tau_{xy}}{\partial y} + \frac{\partial \tau_{xz}}{\partial z}\right) + \rho f_x \tag{5.2}$$

$$Y - Momentum:\ \frac{\partial(\rho v)}{\partial t} + \frac{\partial(\rho v^2)}{\partial y} + \frac{\partial(\rho uv)}{\partial x} + \frac{\partial(\rho vw)}{\partial z} = -\frac{\partial P}{\partial y} + \left(\frac{\partial \tau_{yx}}{\partial x} + \frac{\partial \tau_{yy}}{\partial y} + \frac{\partial \tau_{yz}}{\partial z}\right) + \rho f_y \tag{5.3}$$

$$Z - Momentum: \frac{\partial(\rho w)}{\partial t} + \frac{\partial(\rho w^2)}{\partial z} + \frac{\partial(\rho u w)}{\partial x} + \frac{\partial(\rho v w)}{\partial y} = -\frac{\partial P}{\partial y} + \left(\frac{\partial \tau_{zx}}{\partial x} + \frac{\partial \tau_{zy}}{\partial y} + \frac{\partial \tau_{zz}}{\partial z}\right) + \rho f_z \tag{5.4}$$

According to Isaac Newton, Newtonian fluids must have a relation between shear stress and the time rate of strain. Thus, shear stresses can be explained as below,

$$\tau_{xx} = \lambda(\nabla\vec{V}) + 2\mu\frac{\partial u}{\partial x} \tag{5.5}$$

$$\tau_{yy} = \lambda(\nabla\vec{V}) + 2\mu\frac{\partial v}{\partial y} \tag{5.6}$$

$$\tau_{zz} = \lambda(\nabla\vec{V}) + 2\mu\frac{\partial w}{\partial z} \tag{5.7}$$

$$\tau_{xy} = \tau_{yx} = \mu\left[\frac{\partial v}{\partial x} + \frac{\partial u}{\partial y}\right] \tag{5.8}$$

$$\tau_{xz} = \tau_{zx} = \mu\left[\frac{\partial w}{\partial x} + \frac{\partial u}{\partial z}\right] \tag{5.9}$$

$$\tau_{yz} = \tau_{zy} = \mu\left[\frac{\partial w}{\partial y} + \frac{\partial v}{\partial z}\right] \tag{5.10}$$

$$\begin{aligned} Energy\ Equation: \ \rho\frac{D}{Dt}\left(e + \frac{\vec{V}^2}{2}\right) \\ &= p\dot{q} + \frac{\partial}{\partial x}\left(k\frac{\partial T}{\partial x}\right) + \frac{\partial}{\partial y}\left(k\frac{\partial T}{\partial y}\right) + \frac{\partial}{\partial z}\left(k\frac{\partial T}{\partial z}\right) - \frac{\partial(up)}{\partial x} \\ &- \frac{\partial(vp)}{\partial y} - \frac{\partial(wp)}{\partial z} + \frac{\partial(u\tau_{xx})}{\partial x} + \frac{\partial(u\tau_{yx})}{\partial y} + \frac{\partial(u\tau_{zx})}{\partial z} \\ &+ \frac{\partial(v\tau_{xy})}{\partial x} + \frac{\partial(v\tau_{yy})}{\partial y} + \frac{\partial(v\tau_{zy})}{\partial z} + \frac{\partial(w\tau_{xz})}{\partial x} \\ &+ \frac{\partial(w\tau_{yz})}{\partial y} + \frac{\partial(w\tau_{zz})}{\partial z} + \rho\vec{f}\vec{V} \end{aligned} \tag{5.11}$$

Our problem occurs in a viscous, incompressible (Ma<0.3, ρ = constant) and steady flow $\left(\partial/_{\partial t} = 0\right)$ condition. Thus, the Navier Stokes equations are simplified and the Energy equation (5.11) is eliminated (Incompressiblity).

$$Simplified\ Continuity\ Equation: \frac{\partial u}{\partial x} + \frac{\partial v}{\partial y} + \frac{\partial w}{\partial z} = 0 \tag{5.12}$$

$$Simplified\ X - Momentum: \rho\left(u\frac{\partial u}{\partial x} + v\frac{\partial u}{\partial y} + w\frac{\partial u}{\partial z}\right) = -\frac{\partial P}{\partial x} + \mu\left(\frac{\partial^2 u}{\partial x^2} + \frac{\partial^2 u}{\partial y^2} + \frac{\partial^2 u}{\partial z^2}\right) + \rho f_x \tag{5.13}$$

$$Simplified\ Y - Momentum: \rho\left(u\frac{\partial v}{\partial x} + v\frac{\partial v}{\partial y} + w\frac{\partial v}{\partial z}\right) = -\frac{\partial P}{\partial y} + \mu\left(\frac{\partial^2 v}{\partial x^2} + \frac{\partial^2 v}{\partial y^2} + \frac{\partial^2 v}{\partial z^2}\right) + \rho f_y \tag{5.14}$$

$$Simplified\ Z - Momentum: \rho\left(u\frac{\partial w}{\partial x} + v\frac{\partial w}{\partial y} + w\frac{\partial w}{\partial z}\right) = -\frac{\partial P}{\partial z} + \mu\left(\frac{\partial^2 w}{\partial x^2} + \frac{\partial^2 w}{\partial y^2} + \frac{\partial^2 w}{\partial z^2}\right) + \rho f_z \tag{5.15}$$

There will be a new turbulent equation from the selected turbulence model. (The details are given in Chapter 5.5.)

In this section, it is provided to express the fundamental equations that driving our solution. In the next subtitles, the different solution strategies that benefit from other linear methods and discretization methods will be discussed in brief.

As traditional particle tracking methods do not take into account the flow separation in accordance with the problem discussed in this thesis, no solution has been made with these methods, but they are quite common to solve similar problems. Since it may be useful for future studies that will be kneaded with optimization algorithms, this section contains related methods and their methodologies.

5.2 DNS, LES and RANS Equations

DNS, LES and RANS methods are widely used to calculate turbulent flows. DNS method is the most accurate one, among others and has unique characteristics of methodology. The methodology of the DNS is different because it uses the discretized solution steps but not include the time-average approach with neglected terms. Although DNS is not need modeling efforts, DNS consumes much calculation time, especially in cases with high Reynolds number like in this thesis. Also, the DNS approach resolves the complete range of scales with solving the unsteady Navier Stokes equations in basics.

Unlike the DNS method, instead of resolving all turbulence models, only large eddies are resolved within the entire domain in the LES method. However, as it is known, only some small scale turbulence models are directly solved within the LES method, whereas the required grid points in specific domain locations would be reduced suddenly. In this method, which uses less time than the DNS method, the solution of filtered Navier Stokes equations is being done. The use of this method will gain importance after the RANS method in time with the increase in the discovered new computational capabilities and thus, LES will become one of the most frequently used methods in the future.

The time-averaged Navier Stokes solution is the basics of the RANS and this method is common in the industry. The principle of RANS depends on the modeling of all the turbulent activity. Derivation of the RANS is exemplified for only the x momentum and continuity equation.

$$RANS\ Continuity\ Equation: \ \frac{\partial \bar{u}}{\partial x} + \frac{\partial \bar{v}}{\partial y} + \frac{\partial \bar{w}}{\partial z} = 0 \tag{5.16}$$

$$\begin{aligned} RANS\ X - Momentum: \ & \rho\left(\bar{u}\frac{\partial \bar{u}}{\partial x} + \bar{v}\frac{\partial \bar{u}}{\partial y} + \bar{w}\frac{\partial \bar{u}}{\partial z}\right) \\ &= -\frac{\partial \bar{P}}{\partial x} + \mu\left(\frac{\partial^2 \bar{u}}{\partial x^2} + \frac{\partial^2 \bar{u}}{\partial y^2} + \frac{\partial^2 \bar{u}}{\partial z^2}\right) + \rho f_x + \overline{\boldsymbol{\rho u}\frac{\boldsymbol{\partial u}}{\boldsymbol{\partial x}}} \\ &+ \overline{\boldsymbol{\rho v}\frac{\boldsymbol{\partial u}}{\boldsymbol{\partial y}}} + \overline{\boldsymbol{\rho w}\frac{\boldsymbol{\partial u}}{\boldsymbol{\partial z}}} \end{aligned} \tag{5.17}$$

The bold terms indicate the Reynolds stresses. When all the momentum equations are solved like equation (5.17), the tensor of the Reynolds stresses show up. (5.18) (ANSYS, 2014)

$$R_{i,j} = \begin{bmatrix} -\rho\overline{u'^2} & -\rho\overline{u'v'} & -\rho\overline{u'w'} \\ -\rho\overline{u'v'} & -\rho\overline{v'^2} & -\rho\overline{v'w'} \\ -\rho\overline{u'w'} & -\rho\overline{v'w'} & -\rho\overline{w'^2} \end{bmatrix} \tag{5.18}$$

This symmetrical tensor has to be solved and derived from the convective terms in equation (5.13) through (5.15). To close RANS equations, $R_{i,j}$ is modelled. There are two ways to close, the first one is Eddy Viscosity Models, which depends on the Boussinesq hypothesis. In this hypothesis, the ratio between Reynolds stresses and the rate of strain of the mean velocity has a constant relation, which is named as Eddy Viscosity. Usually, to calculate the Eddy Viscosity, the transport equations have to be solved on a convenient scale for the Eddy Viscosity models. The other model is called Reynolds Stress Models and in this model, the RANS equations closed by solving the partial derivative transport equations for every $R_{i,j}$ terms.

This method is going to be used in the thesis via the commercial Fluent solver. The prediction of the separation is well handled by this method within the framework of wide usage. This one is also included in the advantageous side of this method for the radome optimization case.

5.3 Traditional Linear Methods

The most used traditional linear ways are commonly classified as VLM and Panel solvers. If the comparison made between the Strip theories and these methods considering the current computational capacity and speed, the high fidelity of the VLM and Panel solvers can fairly be defined as salient. Because the computational time benefits of the Strip solvers are meaningless while checking the performance of all together. However, it should be noted that the differences in the effects of fidelity are the major notions even in the case which neglect the computational speed. Therefore, the details of Panel and VLM solvers are detailed in subsequent sub-chapters.

5.3.1 Panel solver

This method is used to define potential flow variables over arbitrary geometries and the conditions of the panel method are described as incompressible, irrotational and inviscid flows. The Laplace equation is the primary source of this method, which is a linear differential equation, is derived from the full potential flow equation. (Elham, 2013) Based on the continuity equation (steady) expressed in equation (5.1), the velocity potential form is also given and this equation is stated as follows:

$$\rho(\phi_{xx} + \phi_{yy} + \phi_{zz}) + \phi_x \frac{\partial \rho}{\partial x} + \phi_y \frac{\partial \rho}{\partial y} + \phi_z \frac{\partial \rho}{\partial z} = 0 \; where,$$
$$\phi_x = u,\ \phi_y = v,\ \phi_z = w \; and \; V = \sqrt{{\phi_x}^2 + {\phi_y}^2 + {\phi_z}^2} \tag{5.19}$$

For an isentropic flow, between pressure and density, there is a coefficient associated with the speed of sound:

$$\frac{dp}{d\rho} = a^2 \tag{5.20}$$

Under inviscid and irrotational flow conditions, the Euler equation is written as below;

$$dp = -\rho.V.dV = -\rho.d\left(\frac{V^2}{2}\right) = -\rho.d\left(\frac{{\phi_x}^2 + {\phi_y}^2 + {\phi_z}^2}{2}\right) \tag{5.21}$$

A new series of equations (5.22), (5.23), (5.24) are obtained by taking the derivative of the equation (5.21) according to x, y and z directions separately and multiplying it with the ϕ_x, ϕ_y and ϕ_z:

$$\frac{\rho}{a^2}\left({\phi_x}^2\phi_{xx} + \phi_x\phi_y\phi_{yx} + \phi_x\phi_z\phi_{zx}\right) + \frac{\partial \rho}{\partial x}\phi_x = 0 \tag{5.22}$$

$$\frac{\rho}{a^2}\left(\phi_y\phi_x\phi_{xy} + {\phi_y}^2\phi_{yy} + \phi_y\phi_z\phi_{zy}\right) + \frac{\partial \rho}{\partial y}\phi_y = 0 \tag{5.23}$$

$$\frac{\rho}{a^2}\left(\phi_z\phi_x\phi_{xz} + \phi_z\phi_y\phi_{yz} + {\phi_z}^2\phi_{zz}\right) + \frac{\partial\rho}{\partial z}\phi_z = 0 \tag{5.24}$$

To obtain the velocity potential equation, it is necessary to sum these four equations (5.19) and (5.22) through (5.24);

$$\left(1 - \frac{{\phi_x}^2}{a^2}\right)\phi_{xx} + \left(1 - \frac{{\phi_y}^2}{a^2}\right)\phi_{yy} + \left(1 - \frac{{\phi_z}^2}{a^2}\right)\phi_{zz} - \frac{2\phi_x\phi_y}{a^2}\phi_{xy} - \frac{2\phi_x\phi_z}{a^2}\phi_{xz} - \frac{2\phi_y\phi_z}{a^2}\phi_{yz} = 0 \tag{5.25}$$

Finally, the equation (5.25) is simplified to the Laplace equation which has been handled with the satisfied conservation of mass equation, the equation (5.26) evolved by the assumption $a = \infty$ because of the incompressible flow condition;

$$\phi_{xx} + \phi_{yy} + \phi_{zz} = 0 \ \ or \ \ \nabla^2\phi = 0 \ \Rightarrow V = \nabla\phi = 0 \tag{5.26}$$

The same Laplace equation is valid for all geometries; their differences come from the boundary conditions of them. On the other hand, without any mesh grid, this equation entails governing the flow field by using the discretized panels and serves the pressure distribution over these panels. This is called the panel method.

Equation (5.26) is recalled as the different form which is made up of the distribution of potentials that corresponds to the freestream, vortex and sources with respect to the Superposition principle. (Juan J. Alonso, 2000)

$$\phi_{total} = \phi_\infty + \phi_V + \phi_S \tag{5.27}$$

If the airfoil is represented by this method, the panels are also shown as Figure 5.2.

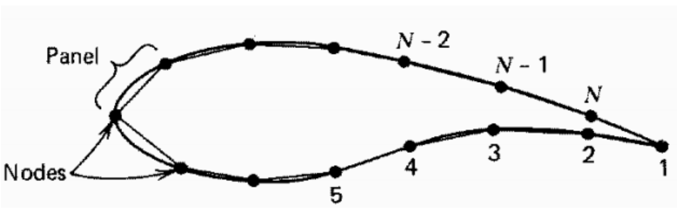

Figure 5.2 : Implementation of The Panel Method On An Airfoil.

Potential flow calculations are made for each of these discrete panels according to equation (5.28), where the source strength will vary on each panel and vortex strength gamma will be constant.

$$\phi = V_\infty(\mathrm{x}\cos\alpha + y\sin\alpha) + \sum_{i=1}^{N}\int_{panel\ i}\left[\frac{q}{2\pi}\ln r - \frac{\gamma}{2\pi}\theta\right]ds \tag{5.28}$$

For equation (1.36), the more the number of panels, i , the more accurate results can be obtained. The reason for this is that as the number of panels increases, similar curves or shapes appear directly with the airfoil geometry. Also, there are N (q) + 1 (γ) unknowns for the N number equations; thus, this is not enough to solve our problem. Therefore, the Kutta condition is applied at the end of the airfoil. In this way, the number of equations and unknown values become equal. (N+1)

As the outcome of the solution of that matrix, the obtained tangential velocities are converted to the Cp value of the airfoil. (5.29)

$$C_p = 1 - \frac{V_t^2}{V_\infty^2} \tag{5.29}$$

This irrotational, inviscid and incompressible flow solver can be turned into the compressible one with the Prandtl-Glauert corrections. The main advantage of this method is fewer calculation times when compared with the other methods, but using this solver, the prediction of the separation will be poor.

5.3.2 Vortex Lattice method

This method is generally used for the first stages of the aircraft concept design phases and applied to the robust conceptual design programs such as VSPAERO. It is generally used for the wing geometries or rudimentary aircraft geometries because of the little time-consuming. Like the panel method, the wing surface is splitted to lots of panels and the vortices are calculated and both methods are defined as low-fidelity methods. In this section, the basics of the VLM methods and the formulations behind the method are summarized.

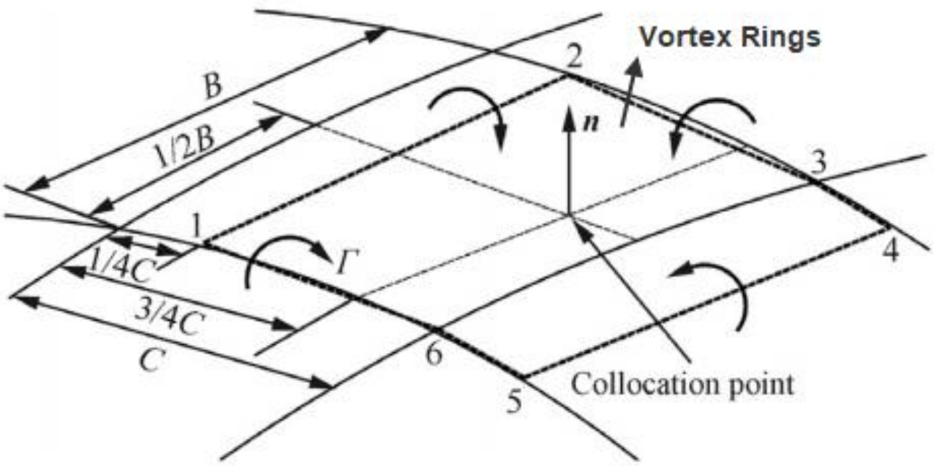

Figure 5.3 : 6-Edge Vortex Ring Example (Gabor et al., 2016).

The normal flow is determined as zero over these panels. At the quarter chord line, the vortex strengths (horseshoe) Γ are gathered. Figure 5.3 shows that the collocation points of the rings are placed onto the three-quarter chord (75%) of the panel. Trailing edge gammas are defined as zero in this method, so the extracted equation would drive our solution and the boundary condition of this have become as follows: (5.30)

$$\nabla(\phi_{\infty} + \varphi_i).\mathrm{n}_i = 0 \text{ and } \gamma_{te} = 0 \tag{5.30}$$

In terms of the influence coefficient matrix v, the vortex strength can be calculated (Biot-Savart Law) (Katz & Plotkin, 2001),

$$\nabla\varphi_i = \sum_{j=1}^{N} \Gamma_j \mathrm{v}_{ij} \;\; and \;\; \nabla\phi_{\infty} = V_{\infty} \tag{5.31}$$

According to the equation (5.30) and (5.31), the acquired linear system from these collocation points of all rings is given in (5.32).

$$\begin{bmatrix} v_{11}.n_1 & v_{12}.n_1 & \cdots & v_{1N}.n_1 \\ v_{21}.n_2 & v_{22}.n_2 & \cdots & v_{2N}.n_2 \\ \vdots & \vdots & & \vdots \\ v_{N1}.n_N & v_{N2}.n_N & \cdots & v_{NN}.n_N \end{bmatrix} \begin{bmatrix} \Gamma_1 \\ \Gamma_2 \\ \vdots \\ \Gamma_N \end{bmatrix} = \begin{bmatrix} -V_{\infty}.n_1 \\ -V_{\infty}.n_2 \\ \vdots \\ -V_{\infty}.n_N \end{bmatrix} \tag{5.32}$$

With the transverse segment vector of the vortices, the force acting on the panel can be found for all individuals. By summing these forces, a single resultant force is calculated in equation (5.33).

$$\text{Total Force} = \sum_{j=1}^{N} \rho(\mathrm{V}_j + V_\infty)\Gamma_j \; x \; l_i \tag{5.33}$$

In equation (5.33), V_j is the perturbation velocity for every individual and l_i is the transverse segment vector of the panels. (Ghoreyshi & Jenkins, 2019) The lift and drag values (induced) can also be calculated by these formulations,

$$\begin{aligned} \text{Drag } &= \mathrm{F}_x.\cos\alpha + \mathrm{F}_z.\sin\alpha \\ Lift &= -\mathrm{F}_x.\sin\alpha + \mathrm{F}_z.\cos\alpha \end{aligned} \tag{5.34}$$

As an advantage, without changing the thin airfoil assumptions at a small angle of attack values, the vortex strengths have been found by the direct numerical calculation. However, one of the most important features that distinguish this method from the panel method is the presence of aerodynamic forces without taking into account the thickness of the panels. In addition, the fact that boundary conditions are applied in the center of the surface without representing the entire surface is an essential disadvantage of this method. (Hadjiev & Panayotov, 2013) For this method, since viscous drag calculation is not possible just like the panel method, this method is not dedicated as a solution method suitable for the problem of this work.

5.4 Common Basic Discretization Methods

Unlike the Panel and Vortex Lattice methods, nonlinear methods, which are based on the Eulerian approach, calculate the velocity and pressure values at certain points within the domain. Nonlinear CFD methods are often used in RANS and Euler solvers, and the solution method in this thesis also performs RANS solutions using the Finite Volume Method (Fluent Solver). FDM and FEM methods are also frequently used methods and the technical details of them are summarized in this section.

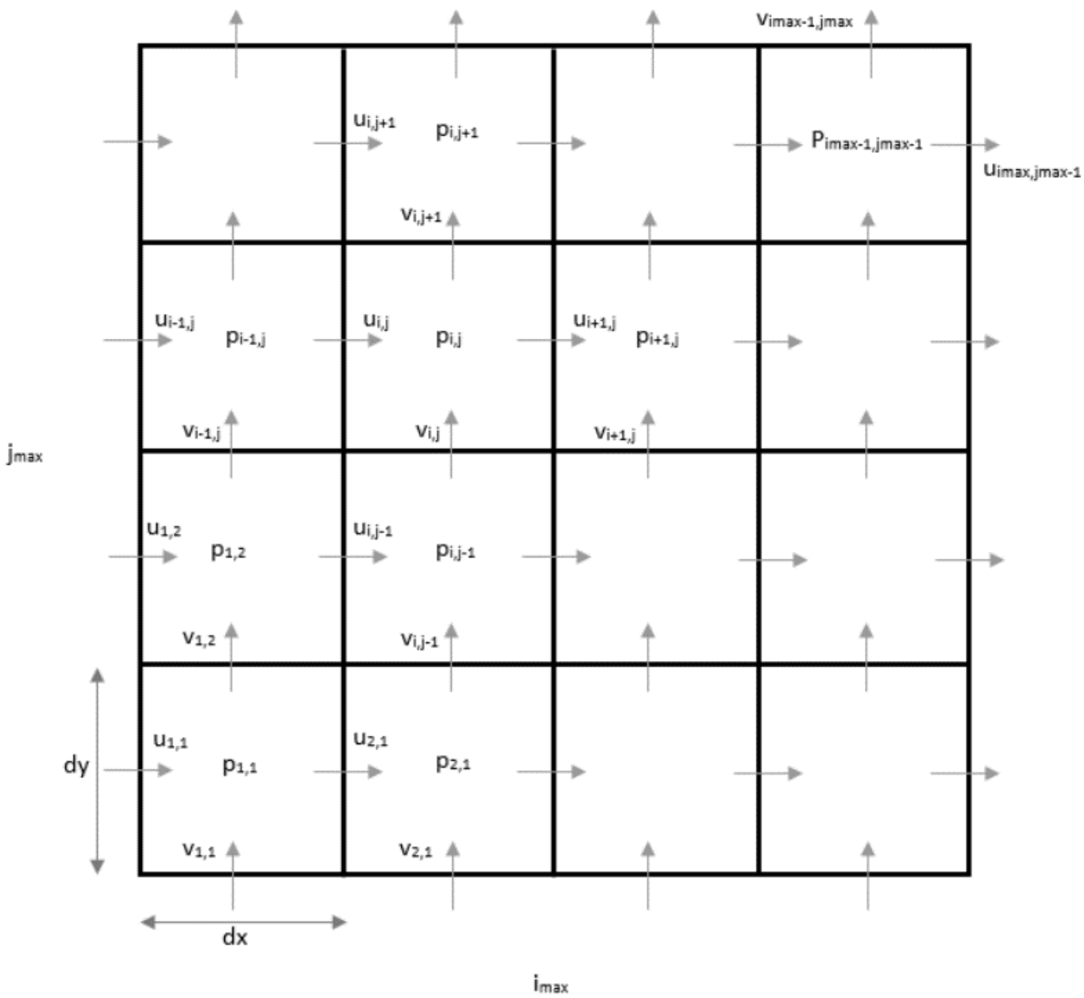

Figure 5.4 : 5X5 FDM 2D Stencil, Grid Representation.

FDM is the oldest way to discrete nonlinear equations between the FVM and FEM. The first numerical analysis (The Flow Past Circular Cylinders at Low Speeds) with FDM performed by A.Thom in 1933. This method makes the flow equations easy-programmable using Taylor Series expansions, which is very quick to implement and is the main reason for the widespread use of the method. Offering a solution in accordance with the structured mesh, this method also imposes a limitation on the variety of applications. An example of 2D implementation is given in Figure 5.7.

For example, consider the incompressible continuity equation for every $p(i,j)$ with respect to Figure 5.7, equation (5.35) is followed: (Tannehill et al., 1997)

$$\left(\frac{u_{i+1,j} - u_{i,j}}{dx}\right) + \left(\frac{v_{i,j+1} - v_{i,j}}{dx}\right) + Err = 0 \tag{5.35}$$

In two-point and first-order derivative (5.35), Err value comes from the Taylor series expansion and is called as “truncation error”.

The second discretization method is the Finite Element Method and generally used for structural analyses. In fact, the first use of FEM was by Courant (Bakker, 2006) in 1943 for a torsion problem. This method divides the computational domain into finite elements. The first phase is obtaining the weak form of the problem PDE. Subsequently, test functions are defined and discretization is made. Bilinear-Quadrilateral, Triangular (2D), hexahedral and tetrahedral elements (3D) are the element types often used by this method. While the unstructured mesh structure formed by these elements can be solved with the FEM method and can quickly solve complex geometries compared to FDM, the solution time is longer than it for the same case. The reason why it cannot be used for the application in this thesis and also one of its most important weaknesses is that the method is challenging to apply and insufficient in solving turbulent flows in contrast to the laminar-viscous problems.

The last and most used method in CFD is the FVM, first properly defined by Evans and Harlow (Bakker, 2006) (1957). The control volume is divided into structured or unstructured grids, similar to FEM, and cells are created within the domain. It is aimed to make flux calculations in each of these cells in conformity with the governing equation. (5.36) This conformity is provided by the neighbour cells. The boundary conditions are also determined according to the problem and assigned to the adjacent edges or surfaces. In FVM, the location of the unknown parameters is determined by the two basic approaches. Cell Vertex based method is being one of them; the other approach is Cell-Centered based. (Figure 5.5)

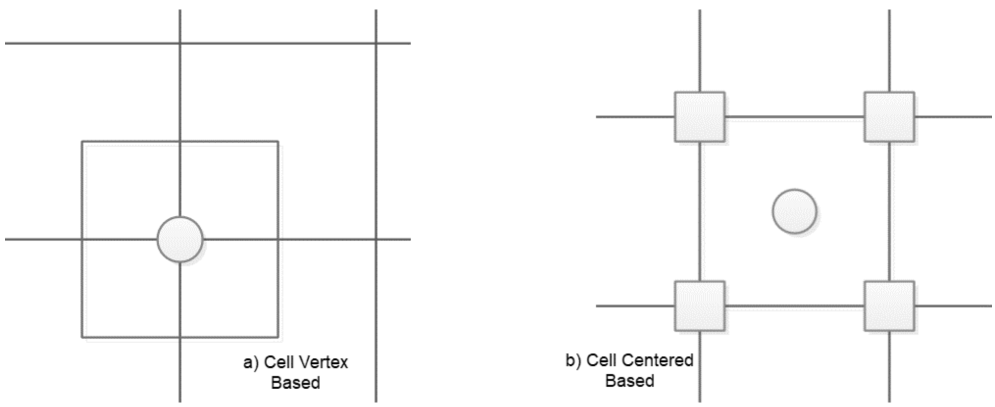

Figure 5.5 : a) Cell Vertex, b) Cell Centered Grid Structures in FVM.

The main difference in these two approaches is that the Cell-Vertex based one is slower than the other, but offers more accurate results. Here, the most important feature of FVM is that spatial discretization is applied directly within the physical domain, and with this feature, it can be easily applied and programmed to both structured and unstructured mesh grids. Another advantage of direct discretization, even when the mesh structure is not very fine, is that it can numerically satisfy the conservation laws. (Blazek, 2001) (Anderson, 1995)

Herewith, the Navier Stokes equations can be defined as;

$$\frac{\partial}{\partial t}\int_{\Omega} \vec{W}\, d\Omega + \oint_{\partial\Omega} \vec{F}_C\, dS = \int_{\Omega} \vec{Q}\, d\Omega + \oint_{\partial\Omega} \vec{F}_V\, dS \tag{5.36}$$

The flux terms in equation (5.37) are made up of convective and viscous parts.

$$\vec{F}_C - \vec{F}_V = \begin{bmatrix} \rho\vec{V} \\ \rho u\vec{V} + n_x p - (n_x\tau_{xx} + n_y\tau_{xy} + n_z\tau_{xz}) \\ \rho v\vec{V} + n_y p - (n_x\tau_{yx} + n_y\tau_{yy} + n_z\tau_{yz}) \\ \rho w\vec{V} + n_z p - (n_x\tau_{zx} + n_y\tau_{zy} + n_z\tau_{zz}) \\ \rho HV - (n_x\theta_x + n_y\theta_y + n_z\theta_z) \end{bmatrix} \tag{5.37}$$

Conservative variables and source term (comes from body forces and volumetric heat) are also given as below, respectively, from equation (5.36).

$$\vec{W} = \begin{bmatrix} \rho \\ \rho u \\ \rho v \\ \rho w \\ \rho E \end{bmatrix} \quad \vec{Q} = \begin{bmatrix} 0 \\ \rho f_x \\ \rho f_y \\ \rho f_z \\ \rho\vec{f}\vec{V} + \dot{q}_h \end{bmatrix} \tag{5.38}$$

These governing equations are used by the temporal discretization methods, which include explicit and implicit numerical solution schemes to solve flow problems by engineers well-understandably. However, the lack of accuracy in the determination of the diffusion values stands out as a significant disadvantage while the use of simple numerics for FVM. Although this disadvantage, the method is still the most prevailing one among the three spatial discretization methods. (Bakker, 2006)

5.5 Realizable K-ε Turbulence Model

Turbulence models are classified in approximately 200 types and used in the solution of transport equations. The most frequently used methods in the solution of RANS equations are divided according to the number of equations. Mixing Length and Cebeci models are used as examples of Zero equation models and the most common single equation model is Spalart-Allmaras. The Realizable K-ε model is one of the most proven ways with k-ω in the 2-equations eddy viscosity model category. (Laccarino, n.d.)

The most important reason for choosing the Realizable K-ε model is raised from some criterias. It can perform the solution of complex shear flows (with rapid strain) and provide the solution of boundary layer separations that may occur behind a bluff-like structure such as our radome. The k-ω model will also be suitable for these solution criterias again, but since the time required for each iteration will be longer than the Realisable K-ε model. (Laccarino, n.d.) Therefore, the prognostic transport equations of the Realisable K-ε model will be solved. This selection is made via Fluent solver. (Solutions are made with the wall treatment information, which is non-equilibrium wall treatment.) Two transport equations of the Realizable K-ε turbulence model are given in equation (5.40) and (5.39) for dissipation rate (ϵ) and turbulence kinetic energy (k). (Wilcox, 2006)

$$\frac{\partial(\rho k)}{\partial t} + \nabla(\rho k u) = \nabla\left[\left(\mu + \frac{\mu_t}{\sigma_k}\right)\nabla k\right] + P_k + P_b - \rho\epsilon - Y_m + S_k \tag{5.39}$$

$$\frac{\partial(\rho\epsilon)}{\partial t} + \nabla(\rho\epsilon u)$$
$$= \nabla\left[\left(\mu + \frac{\mu_t}{\sigma_\epsilon}\right)\nabla\epsilon\right] + \rho C_1 S\epsilon - \rho C_2 \frac{\epsilon^2}{k + \sqrt{\nu\epsilon}} - C_{1_\epsilon}\frac{\epsilon}{k}C_{3_\epsilon}P_b + S_\epsilon \tag{5.40}$$

In equation (5.40), C_1 term is defined below,

$$C_1 = max\left[0.43, 1 + \frac{5}{S\frac{k}{\epsilon} - 5}\right] \; where \;\; S = \sqrt{2S_{ij}S_{ij}} \tag{5.41}$$

The generation of the turbulence kinetic energy because of the mean velocity and buoyancy are symbolized by the P_k and P_b respectively. The eddy viscosity formula and other coefficients that belong to the equation (5.40) are expanded in (5.42) and (5.43)

$$\mu_t = \rho\frac{k^2}{\epsilon}C_\mu \tag{5.42}$$

$$C_\mu = \frac{1}{4.04 + \sqrt{6}.\cos\left(\frac{1}{3}\arccos\left(W\sqrt{6}\right)\right).k\frac{\sqrt{S_{ij}S_{ij} + \widetilde{\Omega}_{ij}\widetilde{\Omega}_{ij}}}{\epsilon}} \tag{5.43}$$

For the $\widetilde{\Omega}_{ij}$, S_{ij} and W, see the equation (5.44) and (5.45).

$$\widetilde{\Omega}_{ij} = \overline{\Omega_{ij}} - 3\epsilon_{ijk}\omega_k \tag{5.44}$$

The formula $\widetilde{\Omega}_{ij}$ rotation tensor for the mean rate is being indicated in terms of the $\overline{\Omega_{ij}}$.

$$W = \frac{S_{ij}S_{jk}S_{ki}}{\left(\sqrt{S_{ij}S_{ij}}\right)^3} \; where, \;\; S_{ij} = \frac{1}{2}\left(\frac{\partial u_j}{\partial x_i} + \frac{\partial u_i}{\partial x_j}\right) \tag{5.45}$$

Likewise, the Standard K-ε, model constants are given in equation (5.46).

$$C_{1_\epsilon} = 1.44, \qquad C_2 = 1.9, \qquad \sigma_k = 1, \qquad \sigma_\epsilon = 1.2 \tag{5.46}$$

All these model constants are used for many types of turbulent flow applications, even in ventilation problems of a room. Thus, the highly considered boundary layer separation will be captured accurately owing to the usage of this Realizable K-ε model turbulent model.

5.6 Validation of The Solver

Fluent solver is selected as a calculator of the turbulent flow characteristics and finding the closest gradient values of the nodes to get the actual result. In chapter 4, the correct approximations were attempted for the grid structure. However, it should be shown that simpler solution alternatives in 2D are compared with the data in the literature to verify this solver for their grid properties and the solution domain.

In order to ensure this satisfactory process of the whole algorithm, it must be proved that the solver has to produce the right values in similar model properties and the nearly same designed geometries while considering the basic dimensions and airflow constants. Different thick airfoils are adopted in a wide range of angle of attack values for this purpose. Selected NACA 63-430 and 63-A415 airfoils are operated to show the solver is appropriate for the radome geometries.

5.6.1 2D Validation study of the NACA 63-430 airfoil

NACA 63-430 airfoil geometry, which has a 30% thickness ratio, is formulated for the CAD program knowledge of the curve creation. According to the 0.6 m (Case 1) and 1 m (Case 2) chordwise model of the NACA 63-430, the airfoil coordinates are scaled and conveyed to the CATIA platform using VBA macros manually. Then, boundaries of the semi-rectangular domain joined with the semi-circular nose are set like the radome domain creation detailed in Section 4.1. (Figure 5.7)

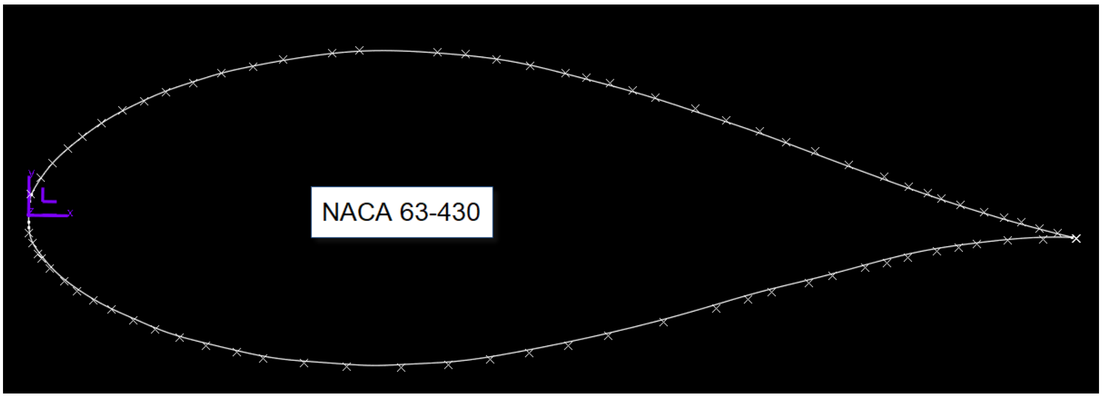

Figure 5.6 : Airfoil Coordinates (NACA 63-430).

Meshing scenario is again created in ANSA for both layer and standard surface mesh. While realizing the mesh structure of that 2D RANS model, y^+ and turbulent equations are determined using the same way with the radome problems of the GA. Because of the case similarities that are taken as reference for this validation case, the layer growth factor is accepted 1.1. However, the absolute first height is also calculated as 0.091 mm (Case 1) and 0.8mm (Case 2) for $y^+ = 30$ (Case 1) and $y^+ = 50$ (Case 2) unlike the source (Rahimi et al., 2014), because of the y^+ requirement of the Realizable k-epsilon turbulence model, like the given cases in Table 4.2. As a piece of information about cell numbers, the total number of mesh elements is fixed to the 761653 (Case 1) and 333506 shell cells (Case 2), include nearly 1.5% (Case 1) and 10% (Case 2) quad-layer cells except for trias.

Additionally, the flow parameters have to be known to calculate y (first cell height) from given y^+ values using equation (4.1). Therefore, Table 5.1 and Table 5.2 are created to show the parameters of the initial condition and turbulence. It is noted that the pressure-velocity coupling scheme is selected as SIMPLE via the Fluent journal file for both cases.

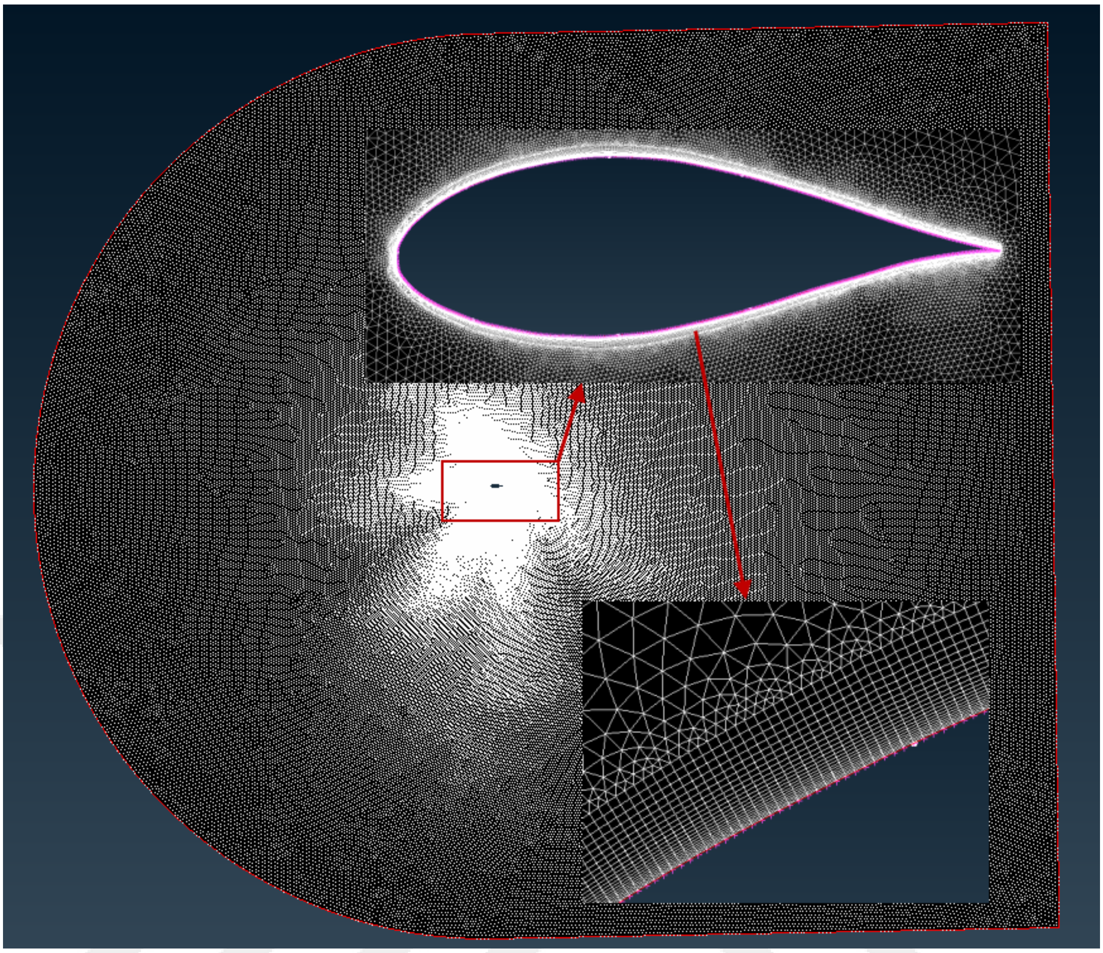

Figure 5.7 : Grid Demonstration Around the NACA 63-430.

Table 5.1 : NACA 63-430 1st Case Flow Properties and 2D Mesh Creation Variables (Fuglsang et al., 1998).

Reynolds Number	Air Velocity (m/s)	Dynamic Viscosity (kg/ms)	Density (kg/m^3)	Growth Factor	Number of Layers	Turbulent Intensity (%)
1.5x10^6	24	1.7526E-05	1.0953	1.1	20	1

Table 5.2 : NACA 63-430 2nd Case Flow Properties and 2D Mesh Creation Variables (Rahimi et al., 2014).

Reynolds Number	Air Velocity (m/s)	Dynamic Viscosity (kg/ms)	Density (kg/m^3)	Growth Factor	Number of Layers	Turbulent Intensity (%)
1.6x10^6	38.02	1.7894E-05	1.255	1.1	20	1

In this FVM solver, the spatial discretization notion is essential to find more precise results at the center of the faces (considering the skewness error); thus, the gradient type is preferred as Green-Gauss Node Based approach rather than the Cell Based methods.

The different angle of attack values applied to Case 1 because the real radome cases have to be represented in this way. In the validation of the high angle of attack values for NACA 63-430, these validation models can provide a better thickness resolution capability of the radome surface simulation when compared to the zero angle of attack model. In the final evaluation of this validation must comprise of the comparisons with the experimental results. Details of the results are blended in Figure 5.8 and Figure 5.9.

Crude estimation is enough for the turbulence modeling in our radome cases because the most important one is the trend of the coefficients in every angle of attack changes. The k-epsilon Realizable (with a selection of non-equilibrium wall function using the Fluent User Guide (ANSYS, 2014)) is found as suitable to resolve the tendency of these coefficients and faster than k-ω SST model.

The differences between the experimental result and the k-epsilon Realizable model remain under 15% for both c_L and c_D. (Fuglsang et al., 1998) Also, magnitudes of these forces behave in the same tendency with their experimental results as the angle of attack is changed. These changes cover the many geometric chromosomes in the radome population.

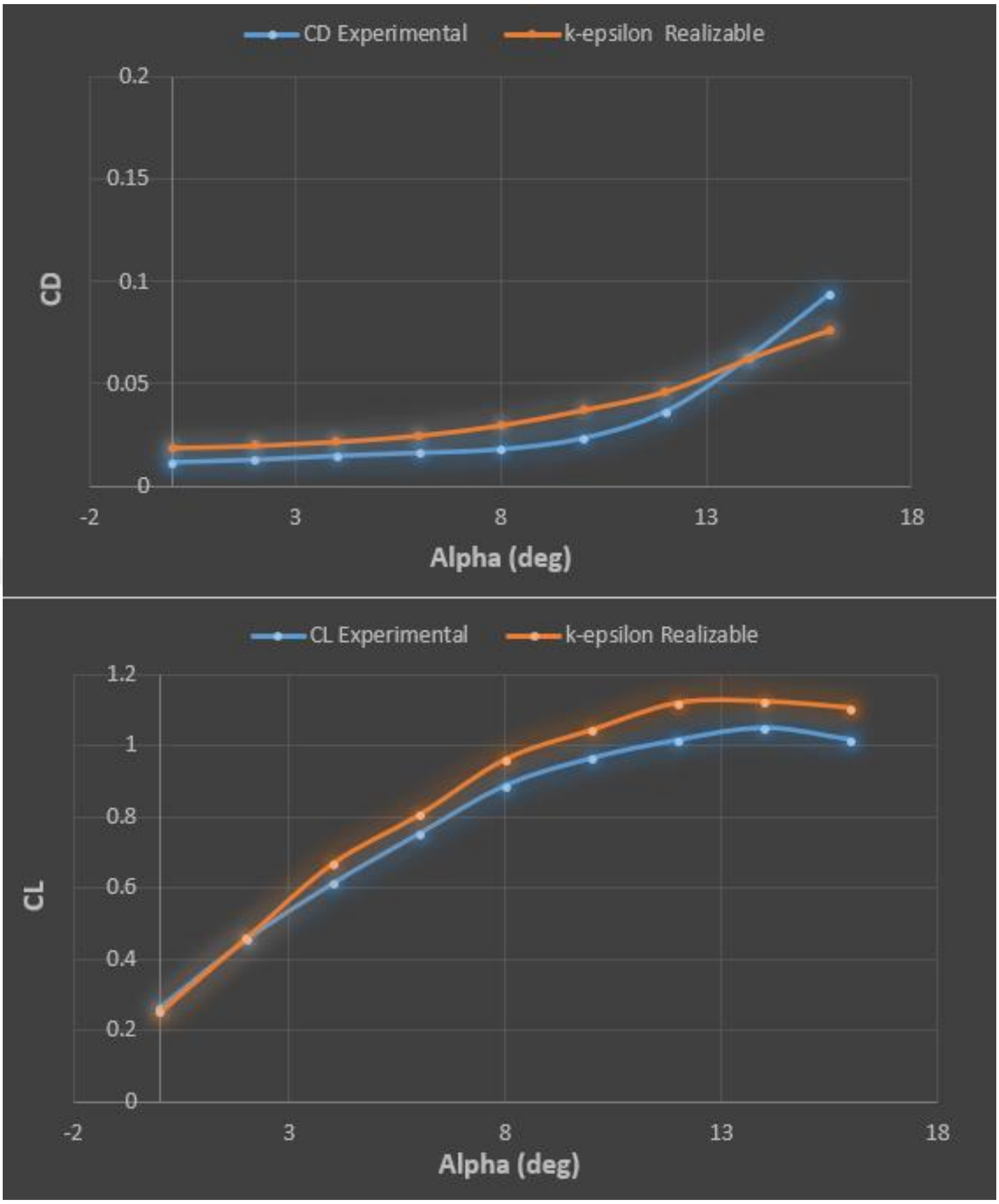

Figure 5.8 : c_L/Alpha and c_D/Alpha Graphs (Fuglsang et al., 1998) with Fluent Solution (k-epsilon Realizable Case 1).

Another NACA 63-430 case (Case 2) is solved for only 6 and 10 deg angle of attack values and their flow constants and mesh parameters are detailed in Table 5.2. This case is created to illustrate comparable chordwise -Cp graphs from the source (Rahimi et al., 2014) (experimental and Realizable K-epsilon model).

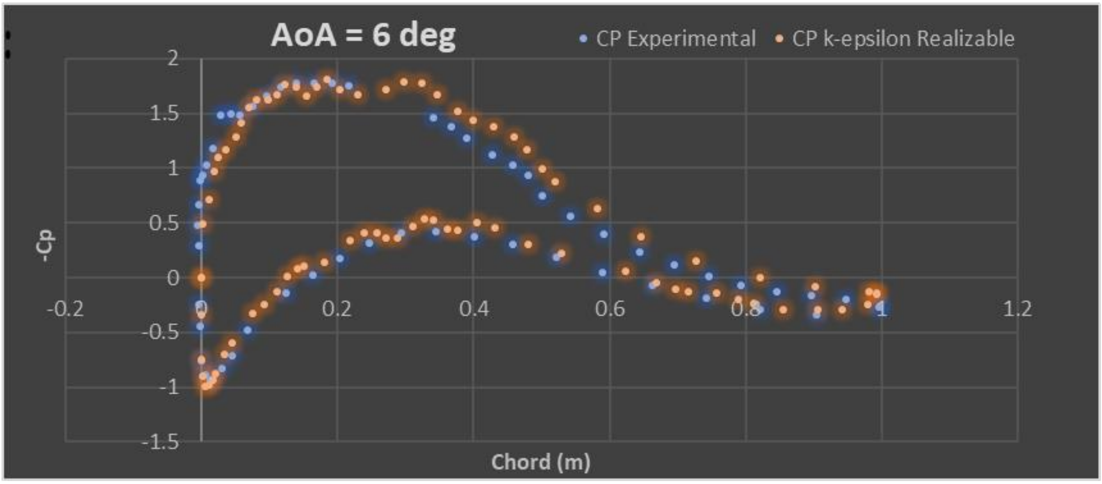

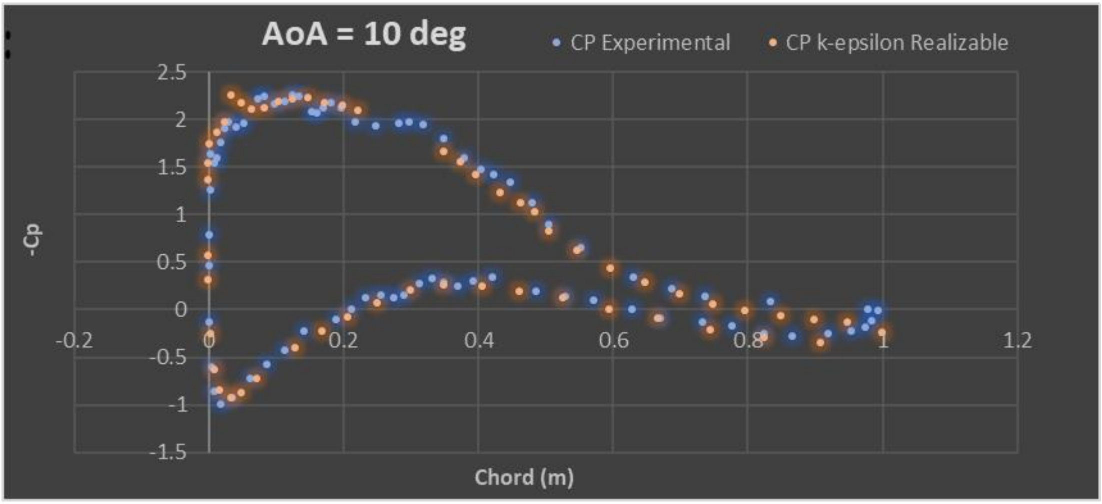

Figure 5.9 : AoA 6, 10 deg - Pressure Coefficient Results (Rahimi et al., 2014) with Fluent Solution (k-epsilon Realizable Case 2).

For the final assessment, the solution with this airfoil thickness value contains similar errors when compared to the data in the reference source. In addition, when an objective evaluation is made, the changes in the drag and lift coefficients are framed for each angle and the differences are negligible according to this airfoil dimension. (Figure 5.8)

When looking at the results of the different angle of attack cases, which will represent the high thickness radome verification of the solution methods of those radomes completed employing 2-dimensional models. High angle of attack values will cause an early separation location, which is near to the nose when compared with the other airfoil has 0 angle of attack and 40% thickness. (NACA 63-440) Therefore, the correct approach is going to be followed by using this technique while checking the skin friction details for each validation section. In this way, it is obvious that investigating the locations of separation is a more conservative method for a radome solution assessment, which includes replacement with the high angle of attack validation instead of high thickness one. Figure 5.10 is summoned to figure out their differences in point of skin friction.

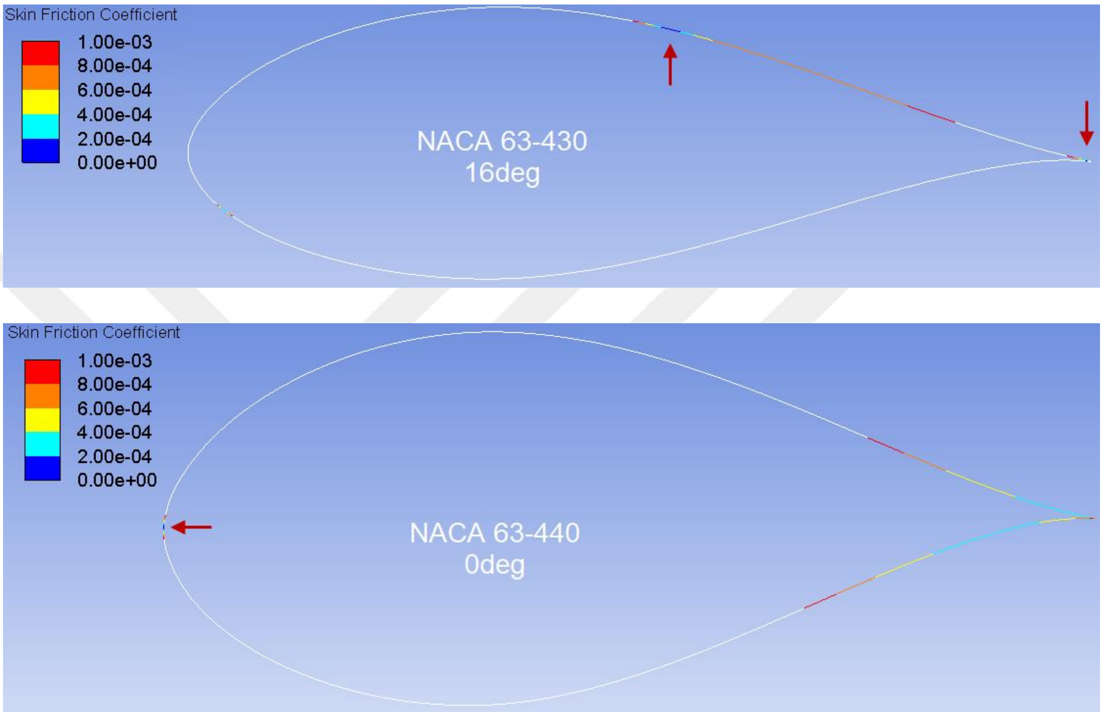

Figure 5.10 : NACA 63-430 (AoA=16 deg) and NACA 63-440 (AoA=0 deg) Separation Prediction Using Skin Friction Contours (Fluent).

The results presented here demonstrate that the Fluent solver to be used for the natural eliminating algorithm can be adopted for that specified aerodynamic purpose or objective function; however, the validation of NACA63-430 fit for purpose and used for the radome thicknesses that must be in a range between the 30% and 40%. Such that, when the produced radome thicknesses are evaluated together with the objective function (Both Lift and Drag minimization), they generally found in that interval.

5.6.2 2D Validation study of the NACA 63-A015 airfoil

Validation studies are divided into two subsections because of the need of the scanning the all possible radome thicknesses in the unique flow condition. The other one is selected from the range between 15% and 30% arbitrary radome thickness is enveloped by this angle of attack approach again. If this NACA 63-A015 airfoil is validated in 2D like NACA 63-430 airfoil, from approximately 40% to 15% radome thicknesses are sought in the probably most desired space totally. It ought to be considered that out of this interval is not applicable for radome geometry that surrounds the minimum internal volume and can not exceed the defined height within the maximum front and aft limitations detailed in section 3.7. This means that the random radome must have a minimum 15% thickness; thus, the lower bound is an obligatory case to validate, which is the objective of this title.

On the contrary to the lower bound case (NACA 63-A015 Validation), the upper bound (NACA 63-430 Validation) has to be achieved for the thickness interval of the general radome creation phase driven by GA, which is the most critical side when considering the flow stability (separation prediction) and the solution of this will be enough for our radome creation phase.

Here, the lower bound validation of the radome in the 2D airfoil case is solved and detailed with the results of it. When using the same VBA macro with section 5.6.1 the airfoil geometry is imported to the CATIA in the same dimensions. (Figure 5.11)

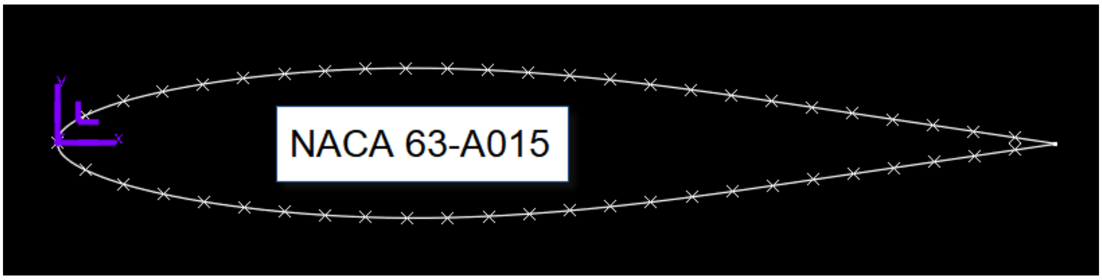

Figure 5.11 : Airfoil Coordinates (NACA 63-A015).

The mesh generation parameters are generally taken as equal with the NACA 63-430 airfoil Case 2. 299815 trias and 5680 quad elements are utilized to solve this 2D RANS problem.

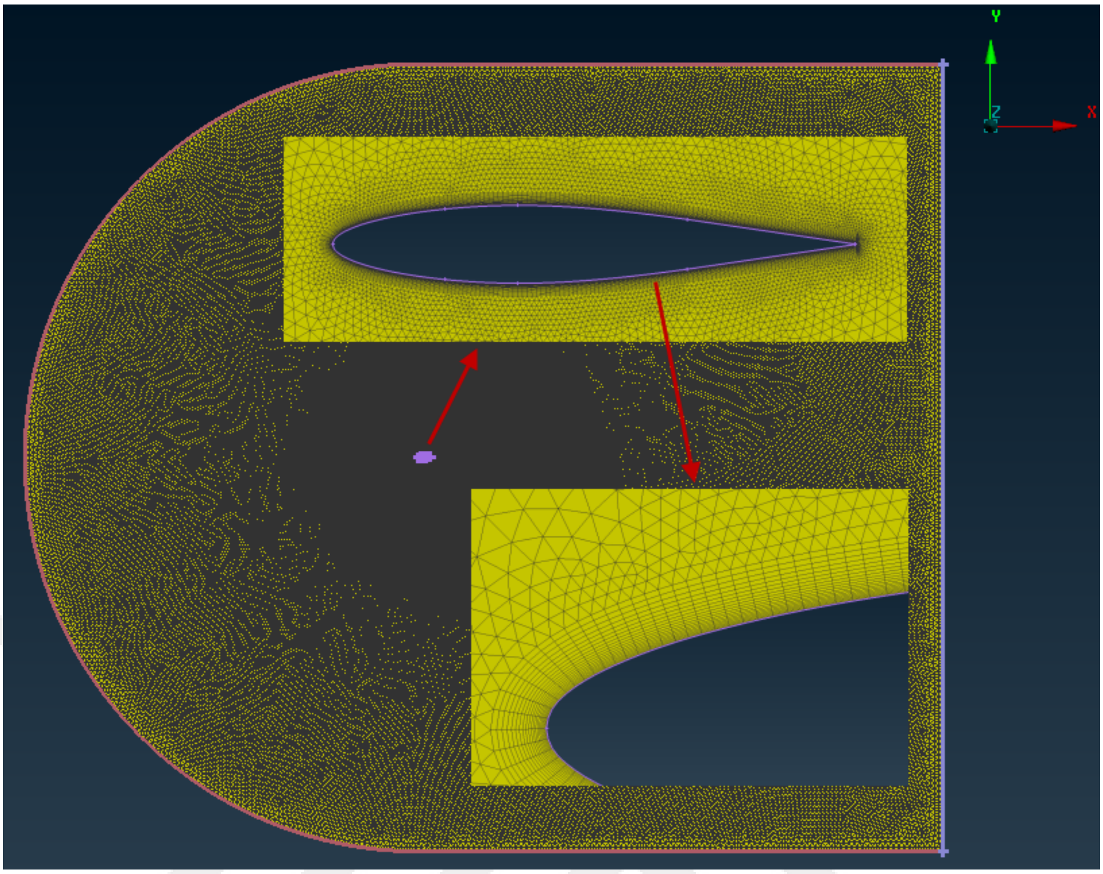

Figure 5.12 : Grid Demonstration Around the NACA 63-A015.

According to the properties of the k-epsilon Realizable wall functions, y (first cell height) is calculated from determined y^+ value ($y^+ = 50$) using equation (4.1). Mesh properties are given in Table 5.3.

Table 5.3 : NACA 63-A015 Flow Properties and 2D Mesh Creation Variables (Lednicer, 1976).

Reynolds Number	Air Velocity (m/s)	Dynamic Viscosity (kg/ms)	Density (kg/m^3)	Growth Factor	Number of Layers	Turbulent Intensity (%)
2.9x10^6	98.3	1.79E-05	1.2131	1.1	20	1

The pressure coupling scheme is assumed to be same with NACA 63-0430 Cases and selected as SIMPLE approach. The limit of the maximum angle of attack is determined by using the skin friction plots because the separation coverage is an asset for this thinner airfoil case when compared with NACA 63-0430 airfoil. c_L and c_D graphs are demonstrated in Figure 5.13.

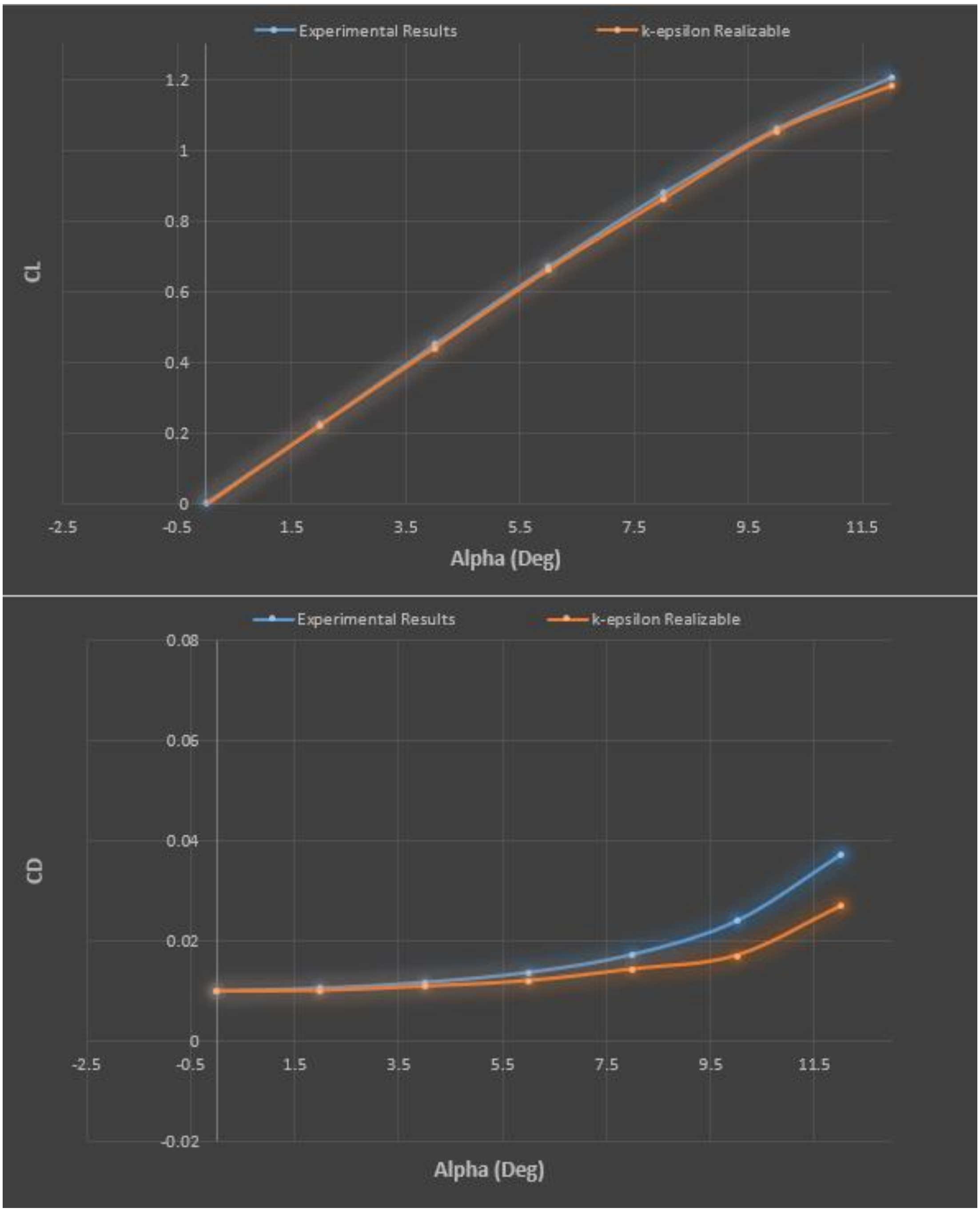

Figure 5.13 : c_L/Alpha and c_D/Alpha Graphs (Lednicer, 1976) with Fluent Solution (k-epsilon Realizable).

It can be seen that the linear region is solved without much error, but increasing in alpha causes stall and discrepancies between the experimental result. In our cases, these discrepancies can not be ignored, but the most crucial notion for our cases is the tendency and moving direction of the c_L and c_D with alpha. The determination of the turbulence model and solver has to meet these requirements without expensive solutions considering computational efforts and time.

On the other hand, the completion of the interval between 15% and 40% radome thickness is designed by the different angle of attack values for NACA 63-A015. The equivalent or adequate angle is determined by using the distribution of the skin friction coefficient over these airfoils. (Figure 5.14).

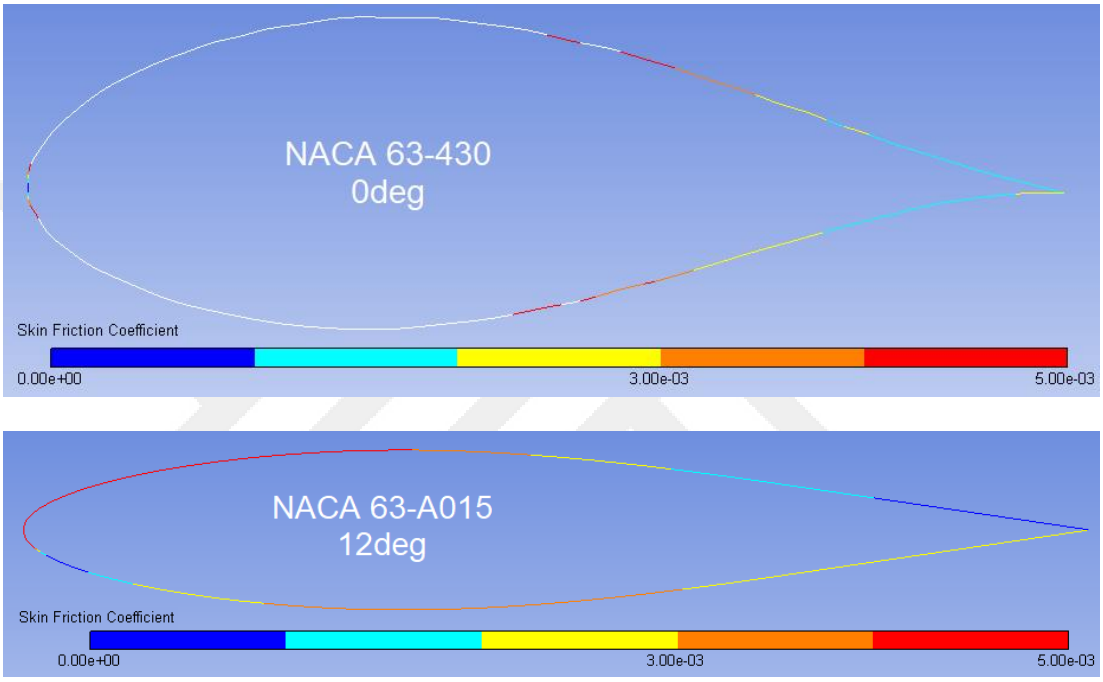

Figure 5.14 : NACA 63-430 (AoA=0 deg) and NACA 63-A015 (AoA=12 deg) Separation Prediction Using Skin Friction Contours (Fluent).

In light of these studies, the most critical stage in the radome generation process or the validation process of the CFD analysis part for the GA is completed.

Based on these studies in this scope, it is shown that the results of the formed radome structure and also their comparisons with each other will give the desired shape in the fastest and most reliable way.

6. OPTIMIZATION RESULTS

In this final chapter, the accumulation of all results and implications are detailed. Before carrying out the whole comparisons and flowfield results, the fitness results and the other GA process have to be investigated. There are 2 solutions to make more understandable this natural outcome for the selected objective functions. Even in the other cases created over a different objective function like the minimization of both variables (c_L and c_D), the same in-domain checks are conducted and comments are made by considering the basic aerodynamic rules in these below sections. The CAD results of both L&D minimization and L/D maximization cases are pointed out in Figure 6.1 and Figure 6.2.

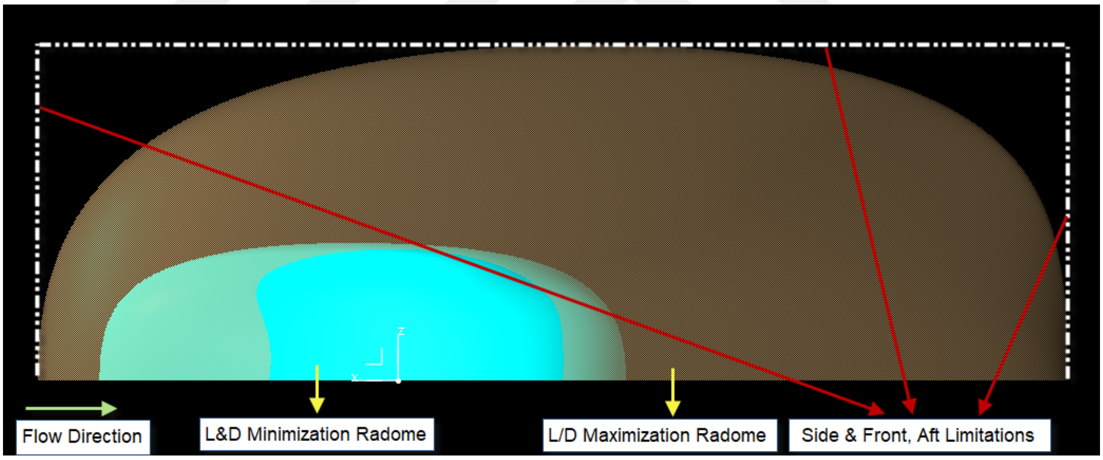

Figure 6.1 : Top View, Cad Results.

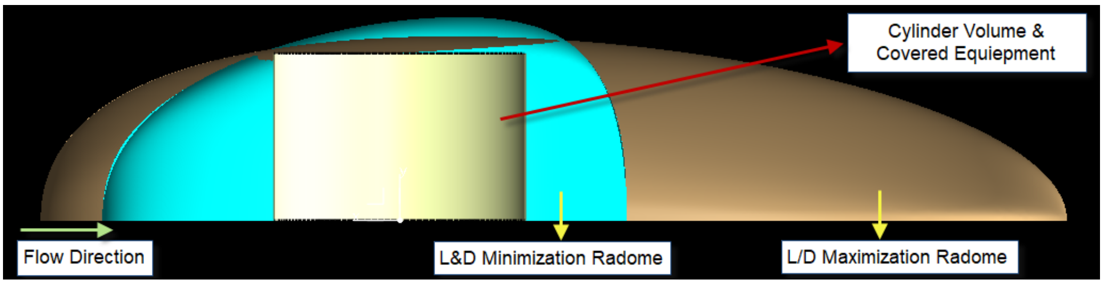

Figure 6.2 : Side View, Cad Results.

6.1 Convergence and Detailed Flowfield Results of the L/D Maximization Case

The analysis results for the two disparate objective function information and the distribution of the best fitness values per iterations are expressed in this section and Section 6.2. Basically, the main objective function of the analysis group carried out by Python code is minimization in both lift force and drag force, while the other objective function information of the trial condition is kept as L/D maximization. In this trial condition, an airfoil-like structure was expected in the side sections, while it was expected to have a geometry that covers this whole specified area and almost intersected with the indicated volume inside at the beginning. When the final geometry is checked attentively, it is seen that all are provided. The flowfield images of the other second and third solutions were held in Appendix C.

The L / D maximization condition that is intended to test the optimization method is set to cover the same cylinder internal volume as the main condition (Section 6.2). In total, 439 analyzes took 35.5 days to complete within the scope of 70 iterations. (12 CPU, Xeon® X5650 2.67GHz) The maximum fitness value obtained was found as 28.76, and the lift and drag forces of this analysis result were calculated as 1151.3N and 40N, respectively. The fitness convergence graphic of this result is given in Figure 6.3.

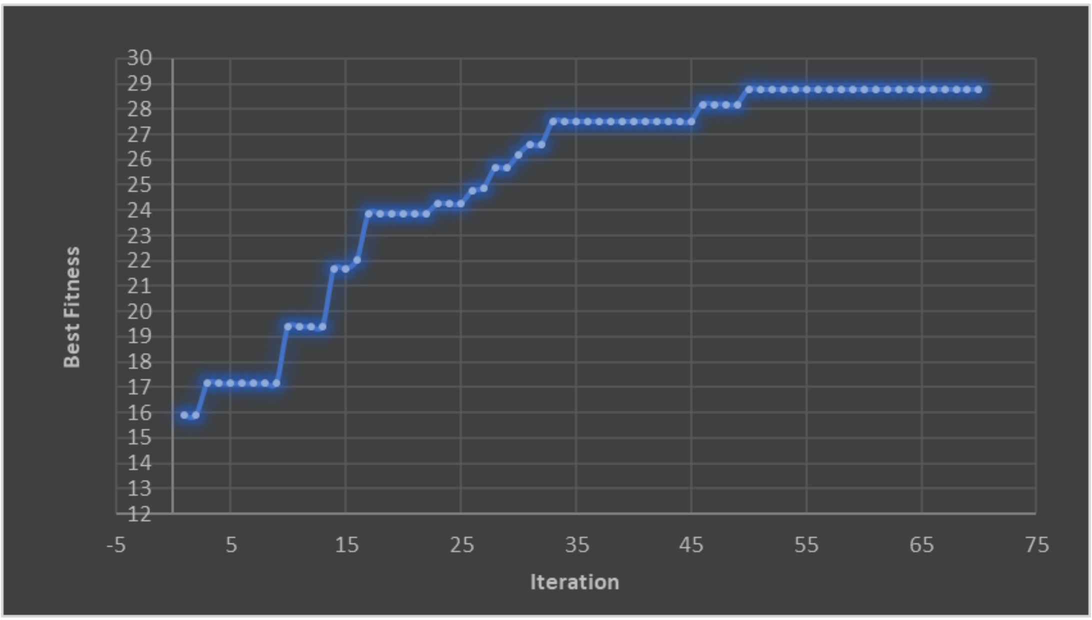

Figure 6.3 : Extracted Best Fitness Values for CL/CD Maximization Case.

By comparing the iteration and best fitness values in Figure 6.3, the following conclusion is reached; It is seen that the sufficient number of iterations is obtained for this solution after iteration 52. During the last 18 iterations, a new trend has not occurred because the algorithm already achieved the best result. The first population has 350 initial elements tough; the others have 70 elements.

The pressure coefficient graphics are illustrated in Figure 6.4, Figure 6.5, and Figure 6.6.

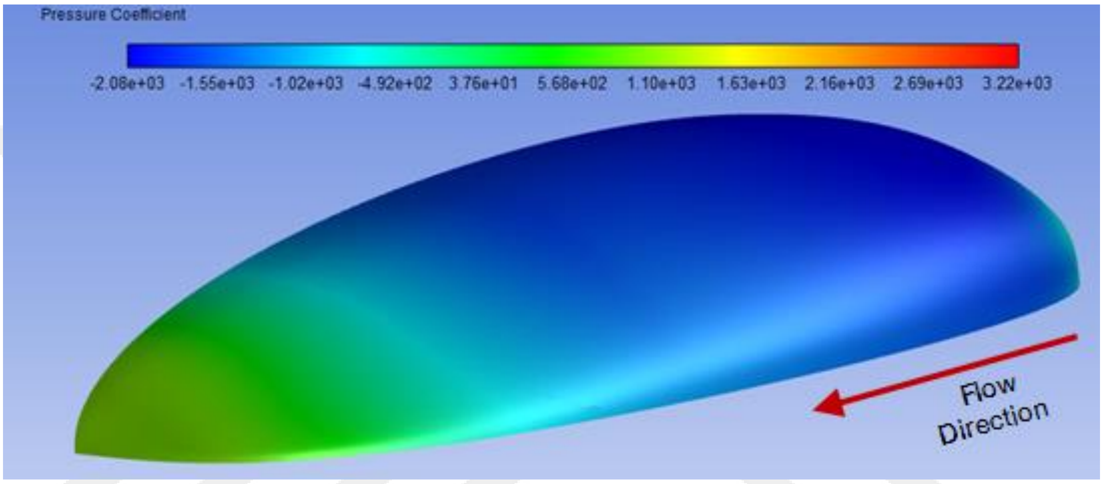

Figure 6.4 : L/D Maximization Case, Pressure Coefficient (Isometric-Aft).

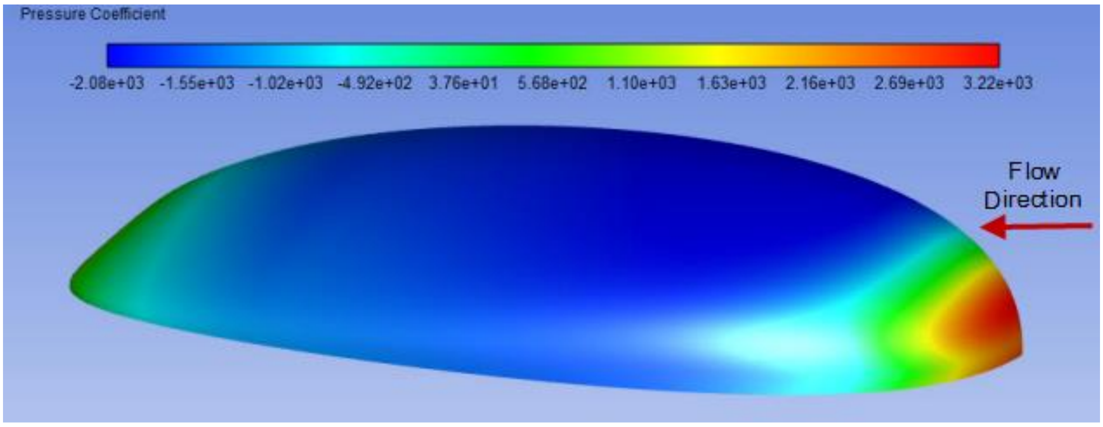

Figure 6.5 : L/D Maximization Case, Pressure Coefficient (Isometric-Front).

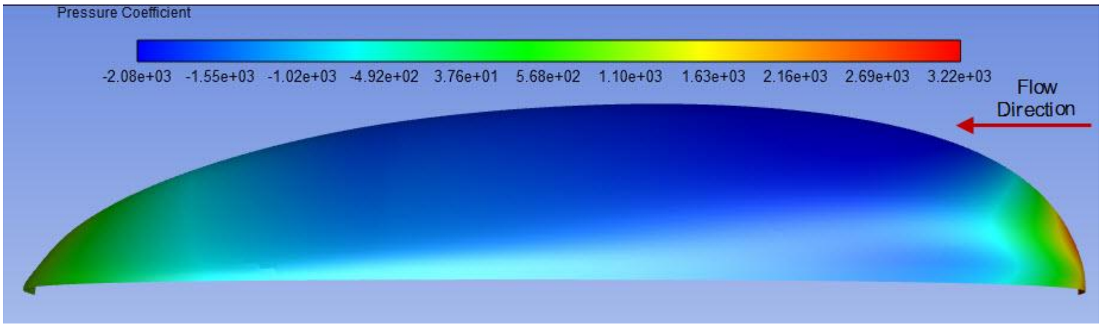

Figure 6.6 : L/D Maximization Case, Pressure Coefficient (Side).

Skin friction contours on the radome surface are shown in Figure 6.7, Figure 6.8, and Figure 6.9. The blue regions are showing the separation locations on the surface.

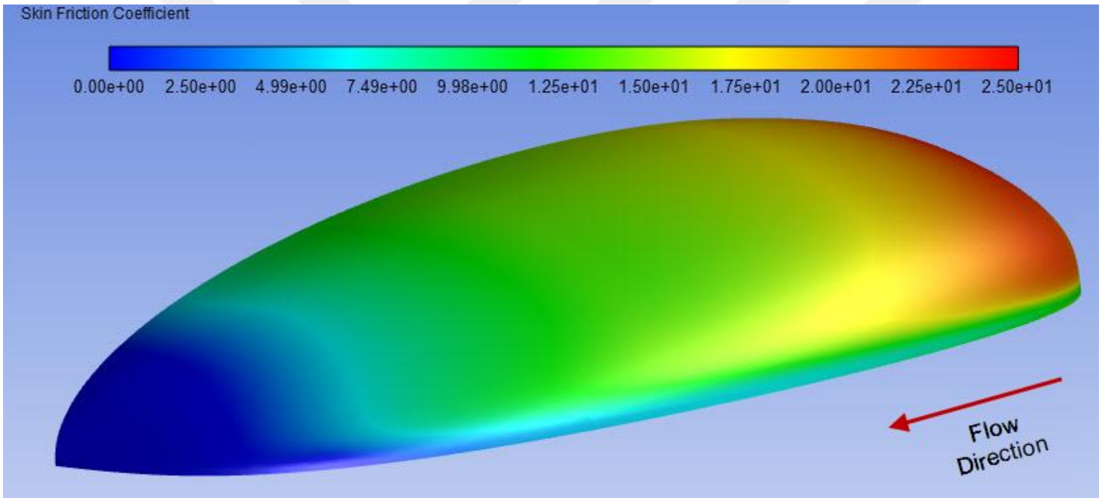

Figure 6.7 : L/D Maximization Case, Skin Friction (Isometric-Aft).

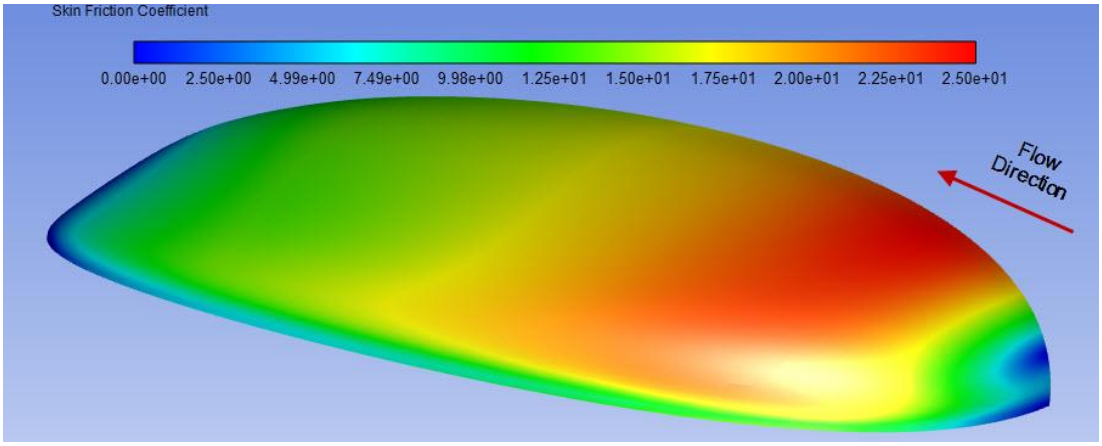

Figure 6.8 : L/D Maximization Case, Skin Friction (Isometric-Front).

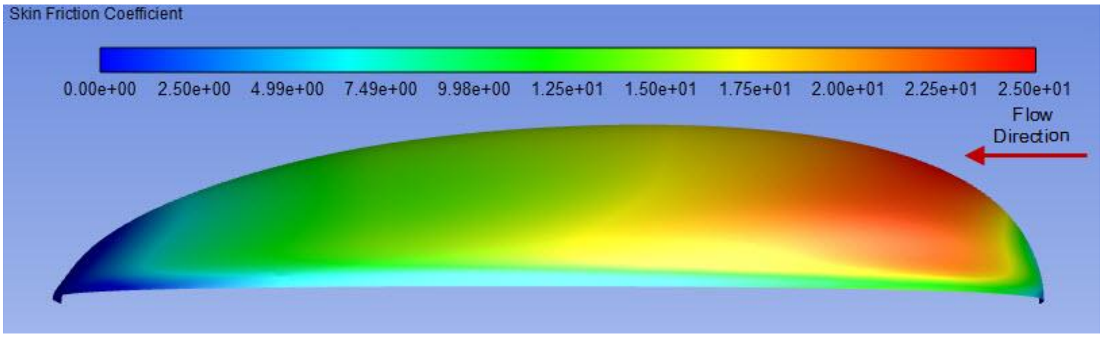

Figure 6.9 : L/D Maximization Case, Skin Friction (Side).

The separation regions are located at the rear side of the radome and small region on the nose. They take place less than 10% of the entire surface to get the minimum drag force.

Wall y^+ values are also drawn on the surface to check initial mesh properties determined in Section 4.2. (Figure 6.10, Figure 6.11, Figure 6.12).

It was observed that the wall y^+ value of the no separation regions (over 80%) on the radome is between 30 and 130. This complies with the k-epsilon Realizable turbulent model requirements. For this reason, it has been observed that the mesh size is correctly determined except for the combination of the lower surface and the radome, the separation area in the posterior region.

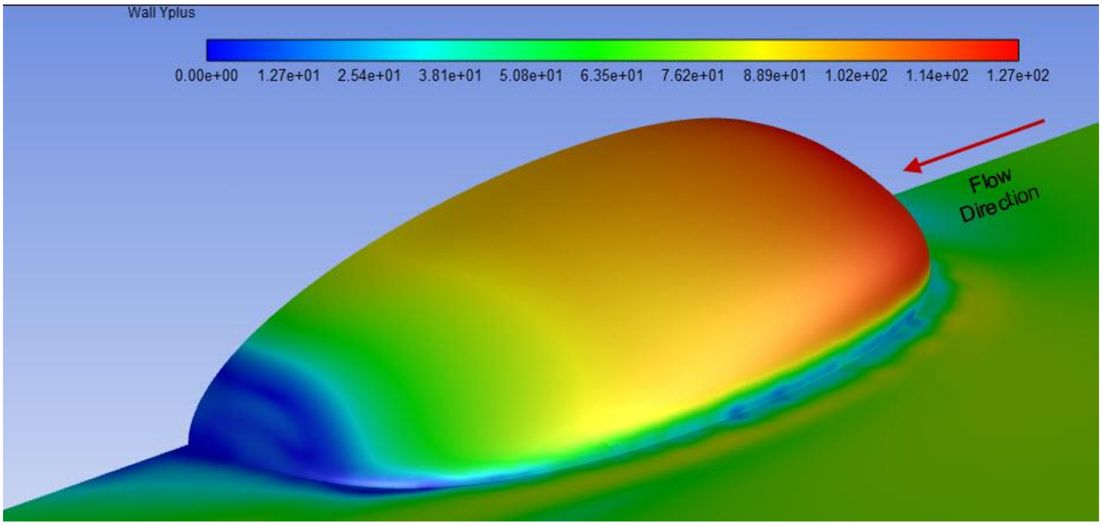

Figure 6.10 : L/D Maximization Case, Wall y^+ (Isometric-Aft).

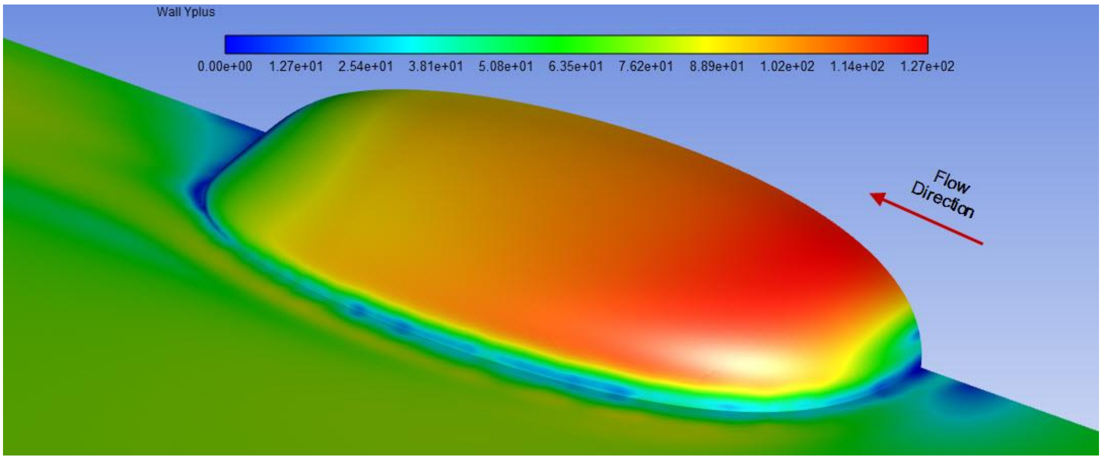

Figure 6.11 : L/D Maximization Case, Wall y^+ (Isometric-Front).

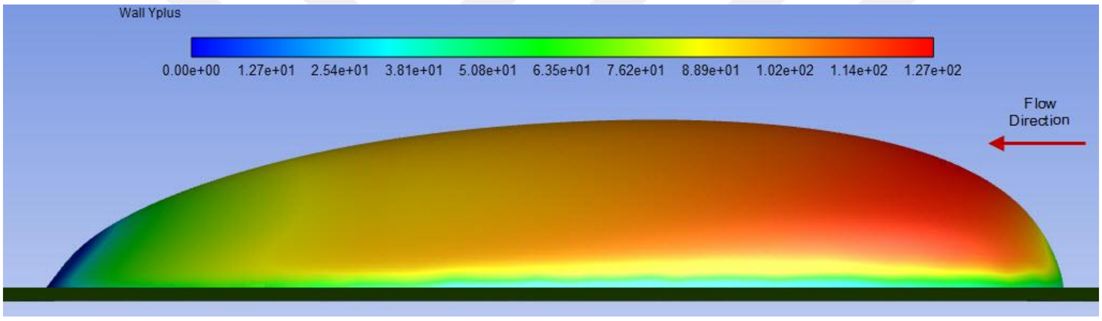

Figure 6.12 : L/D Maximization Case, Wall y^+ (Side).

The radome is strictly bound by the previously defined X and Z input sizes for the integration area. The initial bound is almost filled by the geometry, the L/D maximization case enables this situation. Also, the maximum Y is prohibited using the cylinder intersect element. Then geometry of it is shaped like an airfoil from looking at the side profile, and this geometry is formed as long as possible.

6.2 Convergence and Detailed Flowfield Results of the Lift and Drag Minimization Case

Objective function information belonging to this case, created for the radome optimization, is the search cluster that causes the least change in terms of both the effect on aerodynamic moments and the drag effect, as stated in Section 3. . When the fitness values of the solution belonging to this structure were examined in Figure 6.13 at the first stage, it was observed that the solution had a very good fitness value in the wide random range given at the beginning in the long iteration period. However, this value has been found to belong to a local solution. Then, after iteration 84, it was observed that the solution converged. Within the scope of this solution, 409 iterations were realized and optimization was completed after a 14-day analysis period. Here, unlike the 6.1 condition, due to the fact that the posterior part of the radome structure is shorter, the domains remain smaller, so the solution time is very short for each iteration. It is a convenient outcome, the nature of that genetic algorithm makes sense this explanation about it.

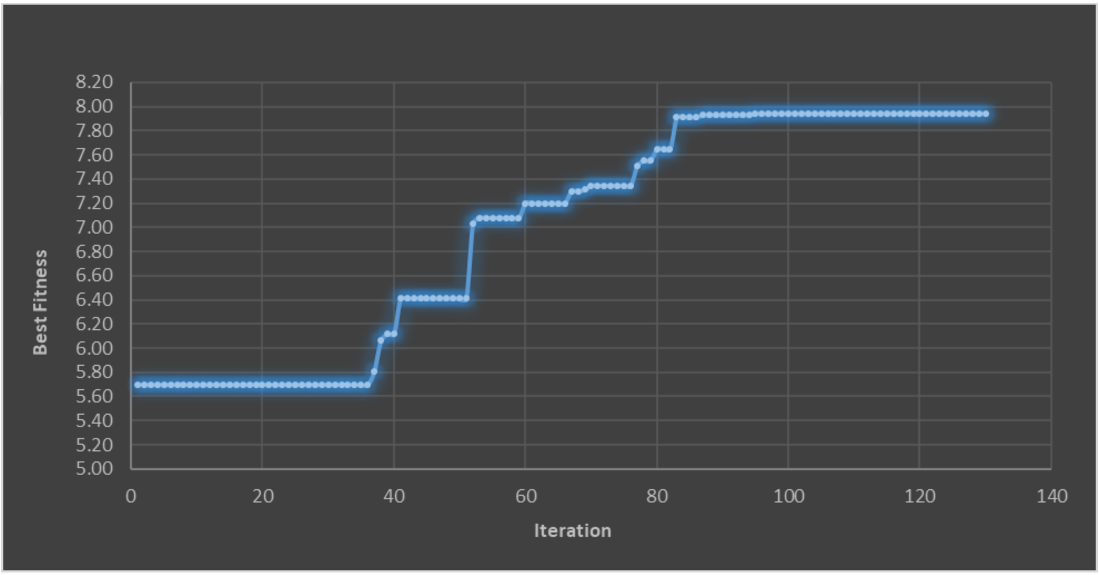

Figure 6.13 : Extracted Best Fitness Values for CL and CD Minimization Case.

While the first iteration of the 130-generation analysis group of the solution presented the 350-element radome alternatives for analysis and evaluation, the population number of the other iterations was limited to 70.

A good fitness value obtained from the population that was procured in the first stage and randomly formed within completely determined limits could not be produced successfully for 36 iterations and the solution was locally stuck. This is because there was only 1 radome solution above 5.6 fitness of the first random population. Due to the high difference between secondary elements during the crossover process, no new and better fitness value was found in these next 36 iterations. However, it took a shorter time for the solution to find the right globally, and the solution converged in iteration 84.

For the best and final analysis solution obtained after the 84th iteration, pressure coefficient, skin friction and wall y^+ graphics are given just like Section 6.1.

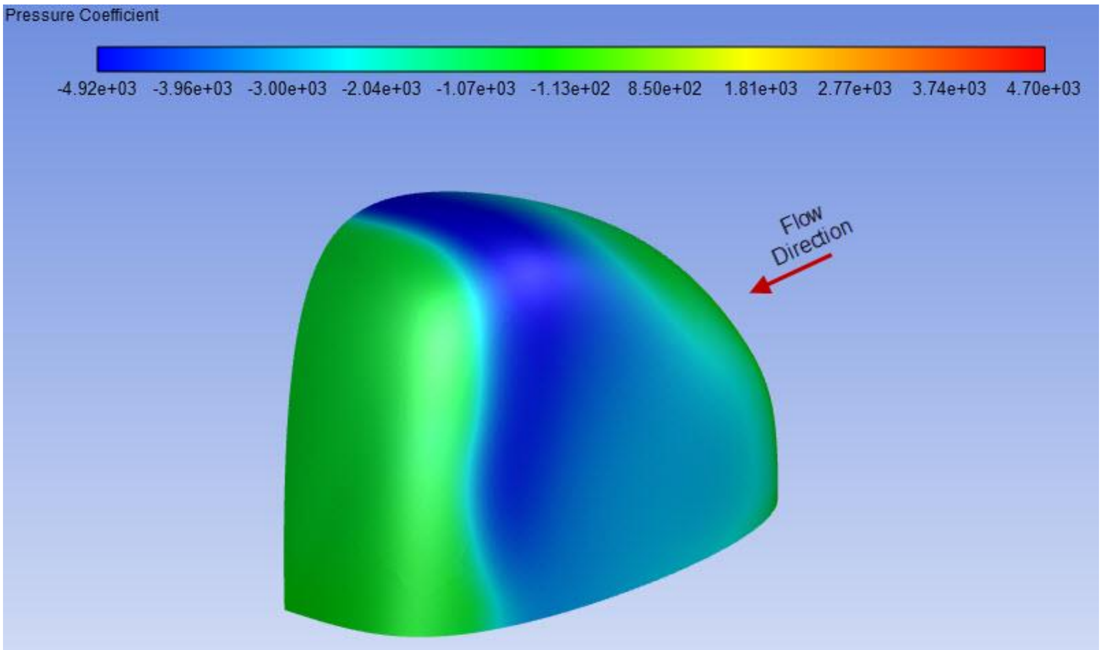

Figure 6.14 : L & D Minimization Case #1, Pressure Coefficient (Isometric-Aft).

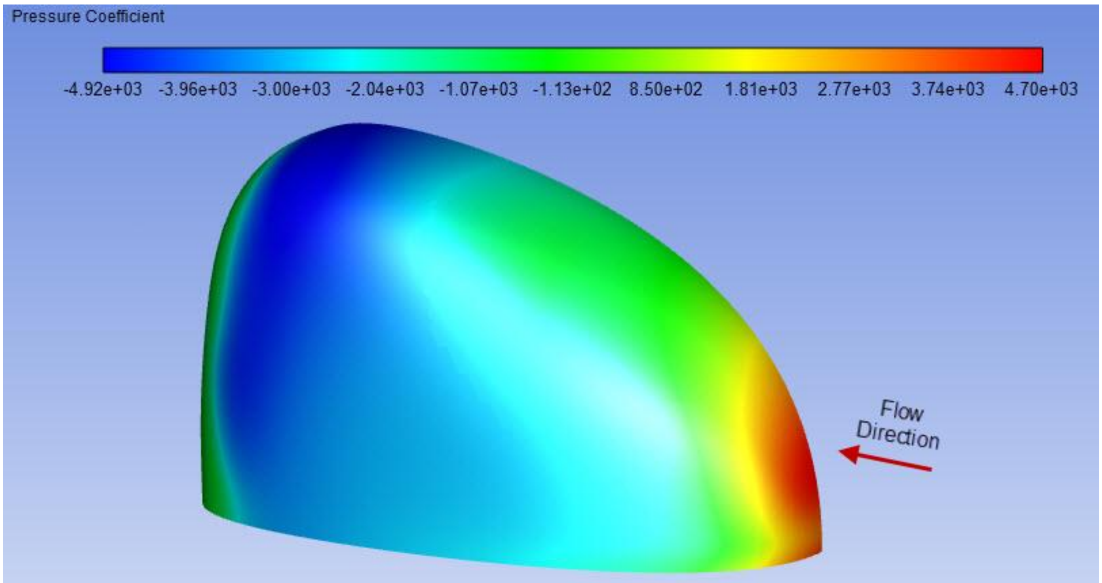

Figure 6.15 : L & D Minimization Case #1, Pressure Coefficient (Isometric-Front).

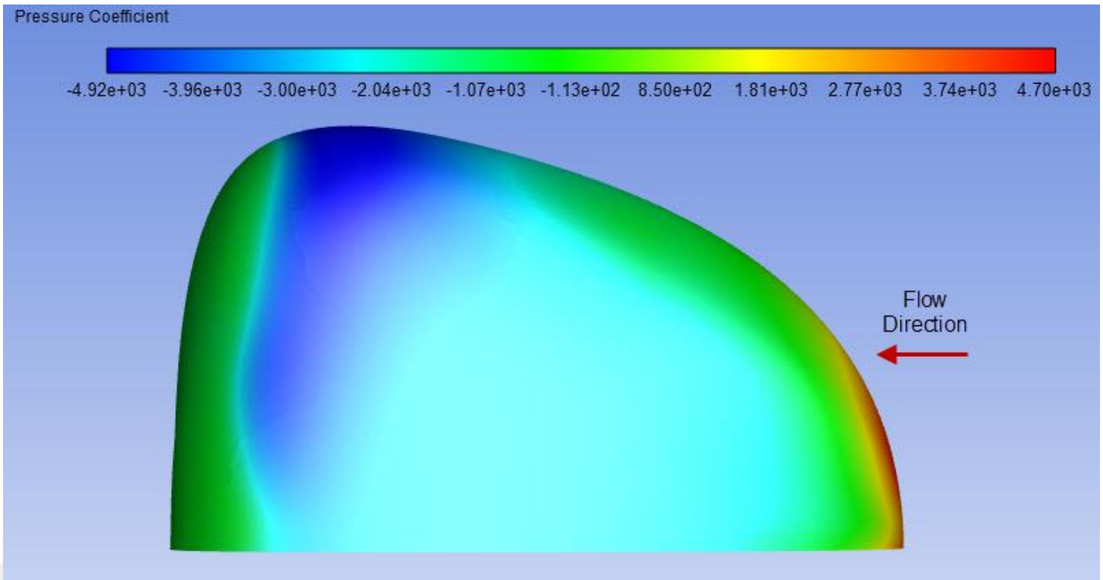

Figure 6.16 : L & D Minimization Case #1, Pressure Coefficient (Side).

The pressure coefficient plots of the best fitness result are given in Figure 6.14, Figure 6.15 and Figure 6.16. Then, the skin friction results of this solution are also transferred with the images in Figure 6.17, Figure 6.18, and Figure 6.19.

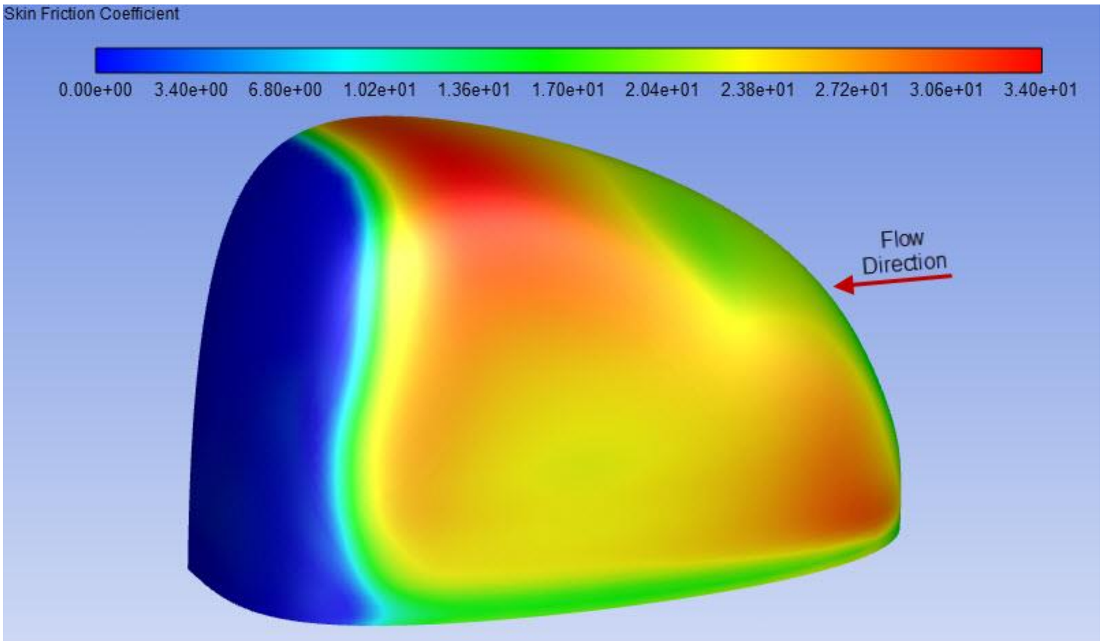

Figure 6.17 : L & D Minimization Case #1, Skin Friction Coefficient (Isometric-Aft).

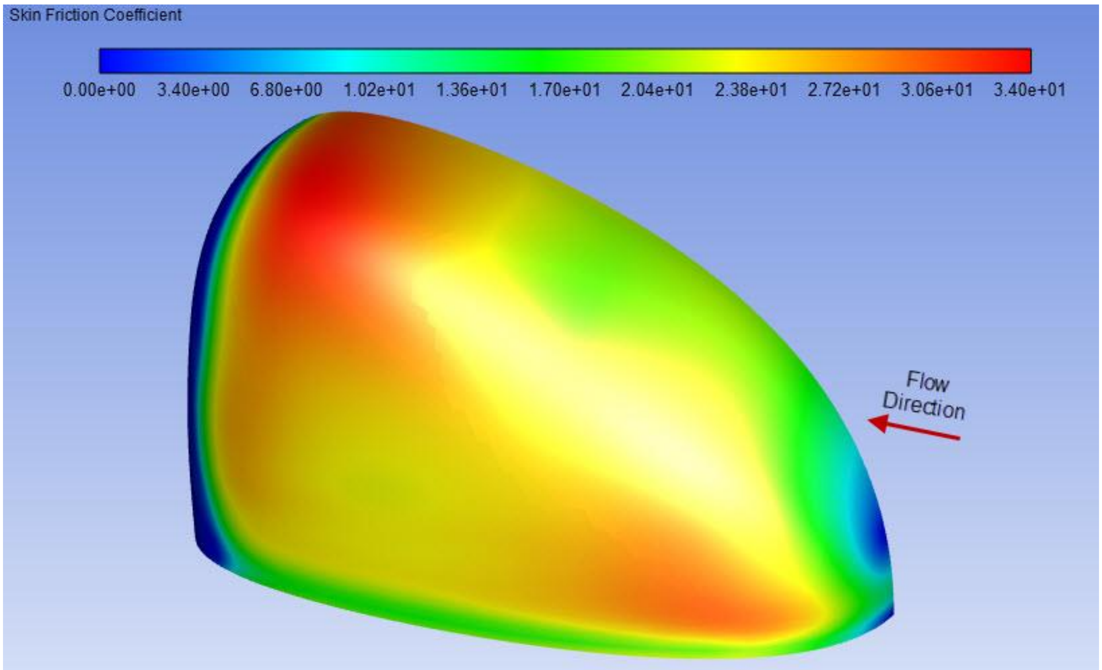

Figure 6.18 : L & D Minimization Case #1, Skin Friction Coefficient (Isometric-Front).

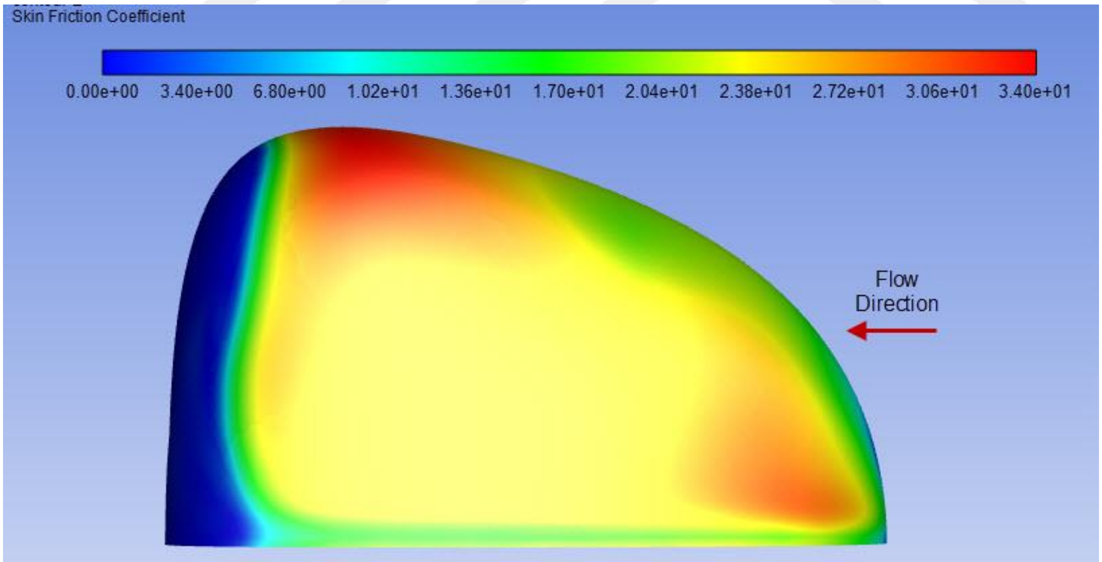

Figure 6.19 : L & D Minimization Case #1, Skin Friction Coefficient (Side).

When the skin friction results are evaluated carefully, the remaining blue regions are indicated as the separation area on the radome surface which has zero value. They take place less than 10% of the entire surface.

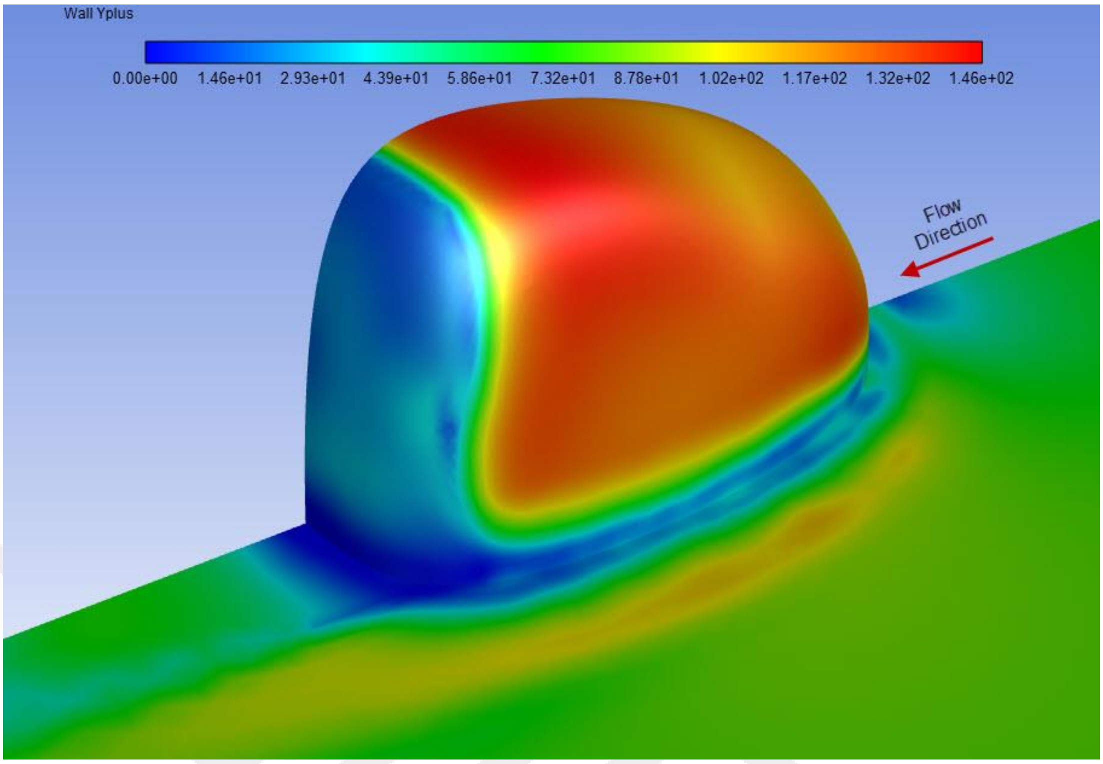

Figure 6.20 : L & D Minimization Case #1, Wall y^+ (Isometric-Aft).

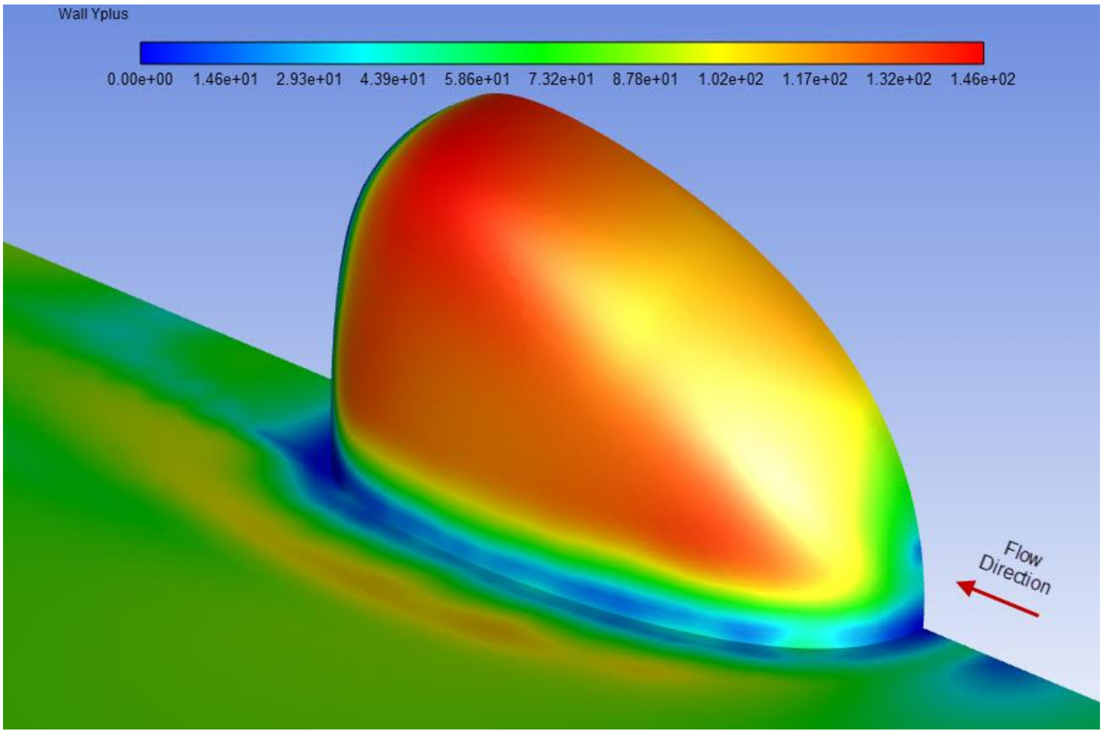

Figure 6.21 : L & D Minimization Case #1, Wall y^+ (Isometric-Front).

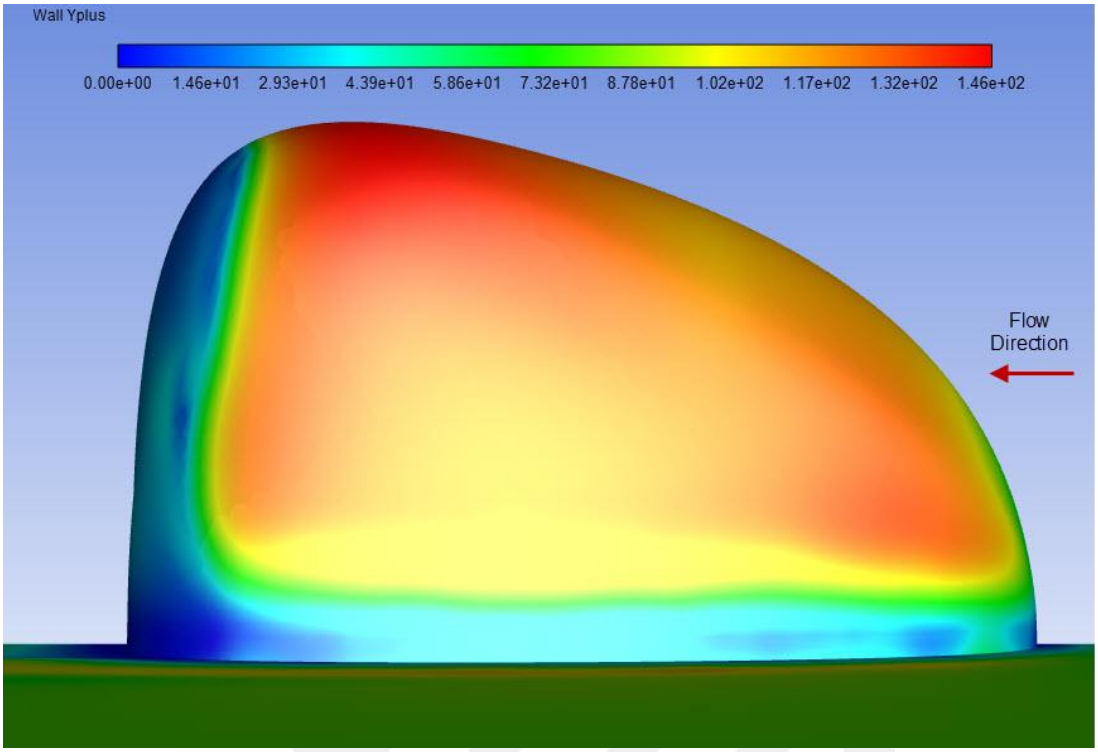

Figure 6.22 : L & D Minimization Case #1, Wall y^+ (Side).

Figure 6.20, Figure 6.21 and Figure 6.22 show us the wall y^+ distribution on the final surface. The range remains between 150 and 0. If the no separation regions are only considered, the turbulence model can be attributed as well-worked.

Results graphics of the second-highest fitness value are given in Appendix C. The fitness result of this value is 7.88. While the lift force value of the best fitness solution was 295.8N, the drag force value was 73.67N; The second fitness value had a lift force value of 304N and a drag force value of 68.5N.

7. FUTURE WORKS AND RECOMMENDATIONS

In the developing computational aerospace industry, revealing the practical solutions for the main engineering departments is observed as valuable. These engineering departments are pointed out as the outer surface design and aerodynamic evaluation areas.

There are plenty of ways to improve this study and these are belonging to the different study areas when looking back from the general view. For future studies, there are five different ways to enhance the main code structure lying on the basis of optimization method that utilizes an artificial intelligence algorithm; two of them are related to CFD works and others are divided under these optimization operations.

Getting more accurate results for the fitness values or coefficients are the most attractive way to evolve this study with also decreasing CFD solution efforts & time.

Three developing studies of the algorithm may be selected as a booster in assessment disciplines; more banausic approaches could be created to finding the fitness values and additional algorithm lines that create more successful domains.

On the optimization side, there is a way to increase evaluation areas or creating an environment of more diverse assessments to present a quick radome build-up process in the final. Algorithm speed has not many effects on the total solution time, so working with this could be selected as secondary.

The third item is a more specific working area for future studies. Because it only depends on the whole elimination algorithm that the working principle is expanded in Chapter 3.7.

In the final case, at the end of a specific evaluation (CFD-dependent or not) way to continue with one of these options, it will be possible to derive different shapes and geometries as well as the optimization of a radome shape automatically.

REFERENCES

Anderson, J. (1995). *Computational Fluid Dynamics, The Basics with Applications*. McGraw-Hill, Inc.

ANSYS. (2014). *Turbulence Modeling - Introduction to ANSYS Fluent*. ANSYS Confidential.

Bakker, A. (2006). *Lecture 5 - Solution Methods Applied Computational Fluid Dynamics*. http://www.bakker.org/dartmouth06/engs150/05-solv.pdf

Blazek, J. (2001). *Computational Fluid Dynamics*. Elsevier.

Casselman, B. (2008). *From Bézier to Bernstein*. http://www.ams.org/publicoutreach/feature-column/fcarc-bezier

Chakroun, W., Al-mesri, I., & Al-fahad, S. (2004). *Effect of Surface Roughness on the Aerodynamic Characteristics of a Symmetrical Airfoil Greek symbols : Subscript :* 547–564.

COESA. (1976). *U.S. Standard Atmosphere Table*. U.S. Government Printing Office.

Elham, A. (2013). *Weight Indexing for Multidisciplinary Design Optimization of Lifting Surfaces*.

Flight-Report. (2015). *Nose Cone Damage - Flight 336*. https://www.dailymail.co.uk/travel/travel_news/article-3070051/Incredible-photos-reveal-aircraft-s-nose-COLLAPSED-bird-flew-Turkish-Airlines-plane-carrying-125-passengers.html

Fuglsang, P., Antoniou, I., Dahl, K. S., & Madsen, H. A. (1998). *Wind Tunnel Tests of the FFA-W3-241 , FFA-W3-301 and NACA 63-430 Airfoils*.

Gabor, O. S., Koreanschi, A., & Botez, R. M. (2016). *A New Non-Linear Vortex Lattice Method: Applications to Wing Aerodynamic Optimizations*. https://doi.org/10.1016/j.cja.2016.08.001

Gardner, B. A., Selig, M. S., Gardner, B. A., & Selig, M. S. (2003). *Airfoil Design Using A Genetic Algorithm and An Inverse Method*. *January*.

Ghoreyshi, M., & Jenkins, K. (2019). *Computational Aerodynamic Modeling of Aerospace Vehicles*. Mdpi AG.

Hadjiev, J., & Panayotov, H. (2013). *Comparative Investigation of Vlm Codes For Joined-Wing Analysis*. 478–482.

Juan J. Alonso. (2000). *Hess-Smith Panel Method Lecture*.

Kanoglu, M. (2007). Chapter 7 : External Forced Convection. In *McGraw-Hill*.

Katz, J., & Plotkin, A. (2001). *Low-Speed Aerodynamics* (Second ed.). Cambridge University.

Kozakoff, D. J. (2010). *Analysis of Radome-Enclosed Antennas* (Second Ed.).

Artech House.

L3HARRIS. (n.d.). *Radomes*. https://www2.l3t.com/essco/radomes/index.htm

Laccarino, G. (n.d.). *Simulation of Turbulent Flows*. https://web.stanford.edu/class/me469b/handouts/turbulence.pdf

Lednicer, D. (1976). *U.S. Army Helicopter Design Datcom - Volume 1 - Airfoils*.

Loos, S., & Giragosian, P. A. (n.d.). *Aerodynamic Design Considerations for Aircraft Radomes*.

Maria. (2016). *High-Performance Composites in Aerospace Applications*. http://pefoamrecycling.over-blog.com/2016/10/high-performance-composites-in-aerospace-applications.html

NASA. (n.d.). *Earth Atmosphere Model (Metric Units)*. https://www.grc.nasa.gov/WWW/K-12/airplane/atmosmet.html

Nygren, C. K. P., & Schulz, M. R. R. (1996). *Breguet's Formulas for Aircraft Range & Endurance An Application of Integral Calculus*.

Obayashi, S., & Tsukahara, T. (1997). *Comparison of Optimization Algorithms for Aerodynamic Shape Design Shigeru*. *35*(8), 1413–1415.

Osaragi, T. (2017). *Classification Method by Information Loss Minimization for Visualizing Spatial Data*. 623–634. https://doi.org/10.1007/978-3-319-62407-5

Patil, S., & Bhende, M. (2014). *Comparison and Analysis of Different Mutation Strategies to improve the Performance of Genetic Algorithm*. *5*(3), 4669–4673.

Peerlings, B. (2018). *A Review of Aerodynamic and Their Applicability to Methods and Solvers – Flow Models, Solution Aircraft Conceptual Design*.

Peterman, L. (2011). *Calling All Engineers : Beyond Form , Fit and Function for Formulated Products*.

Plassard, F., & Abdulhamid, H. (2017). *Test and Simulation Approach Toward The Certification of An Aircraft Structure Subjected to A Bird Strike*. 1.

Rahimi, H., Medjroubi, W., Stoevesandt, B., & Peinke, J. (2014). *2D Numerical Investigation of the Laminar and Turbulent Flow Over Different Airfoils Using OpenFOAM*. https://doi.org/10.1088/1742-6596/555/1/012070

S.Ilavarasu, C.Niranjanappa, Singh, M., & Narayana, P. A. A. (2018). *An Approach to The Design of Composite Radome for Airborne Surveillance Application*. *9*(2), 36–48.

Sasaki, D., Obayashi, S., & Kim, H.-J. (2001). *Evolutionary Algorithm vs. Adjoint Method Applied to SST Shape Optimization*.

Schramm, M., Stoevesandt, B., & Peinke, J. (2018). *Optimization of Airfoils Using the Adjoint Approach and the Influence of Adjoint Turbulent Viscosity*. https://doi.org/10.3390/computation6010005

Schultz, M. P., Finlay, J. A., Callow, M. E., & Callow, J. A. (n.d.). *Three Models to Relate Detachment of Low Form Fouling at Laboratory and Ship Scale*. *19*(2003), 17–26. https://doi.org/10.1080/0892701031000089516

Shankar, M. R., Niranjanappa, A. C., & Dattaguru, B. (2020). *Aerodynamic Optimization of Airborne Radome for Maritime Patrol Radar*. *9*(3), 956–962.

https://doi.org/10.35940/ijeat.B3422.029320

Štorch, V., & Jiˇrí, N. (2017). *Verification and Possible Applications of New 3D Panel Method with Boundary Layer*.

Tannehill, J. C., Anderson, D. A., & Pletcher, R. H. (1997). *Computational Fluid Mechanics and Heat Transfer* (Second ed.). Taylo r& Francis.

Tashnizi, E. S., Taheri, A. A., & Hekmat, M. H. (2010). Investigation of The Adjoint Method In Aerodynamic Optimization Using Various Shape Parameterization Techniques. *Journal of the Brazilian Society of Mechanical Sciences and Engineering*, *32*(2), 176–186. https://doi.org/10.1590/S1678-58782010000200012

Tomac, M. (2011). *Adaptive-Fidelity CFD for Predicting Flying Qualities in Preliminary Aircraft Design*.

Whalen, E. (2018). *Aircraft Radome Characterization via Multiphysics Simulation*. https://insider.altairhyperworks.com/aircraft-radome-characterization-via-multiphysics-simulation/

Wilcox, D. C. (2006). *Turbulence Modeling for CFD* (Third Ed.). Dcw Industries.

Witherden, F. D., & Jameson, A. (2017). *Future Directions of Computational Fluid Dynamics*. *June*. https://doi.org/10.2514/6.2017-3791

APPENDICES

APPENDIX A: Optimization Techniques
APPENDIX B: Domain and Refinement Box with A Detail of Radome Dimensions
APPENDIX C: Flowfield Results of Second Scored Solutions

APPENDIX A

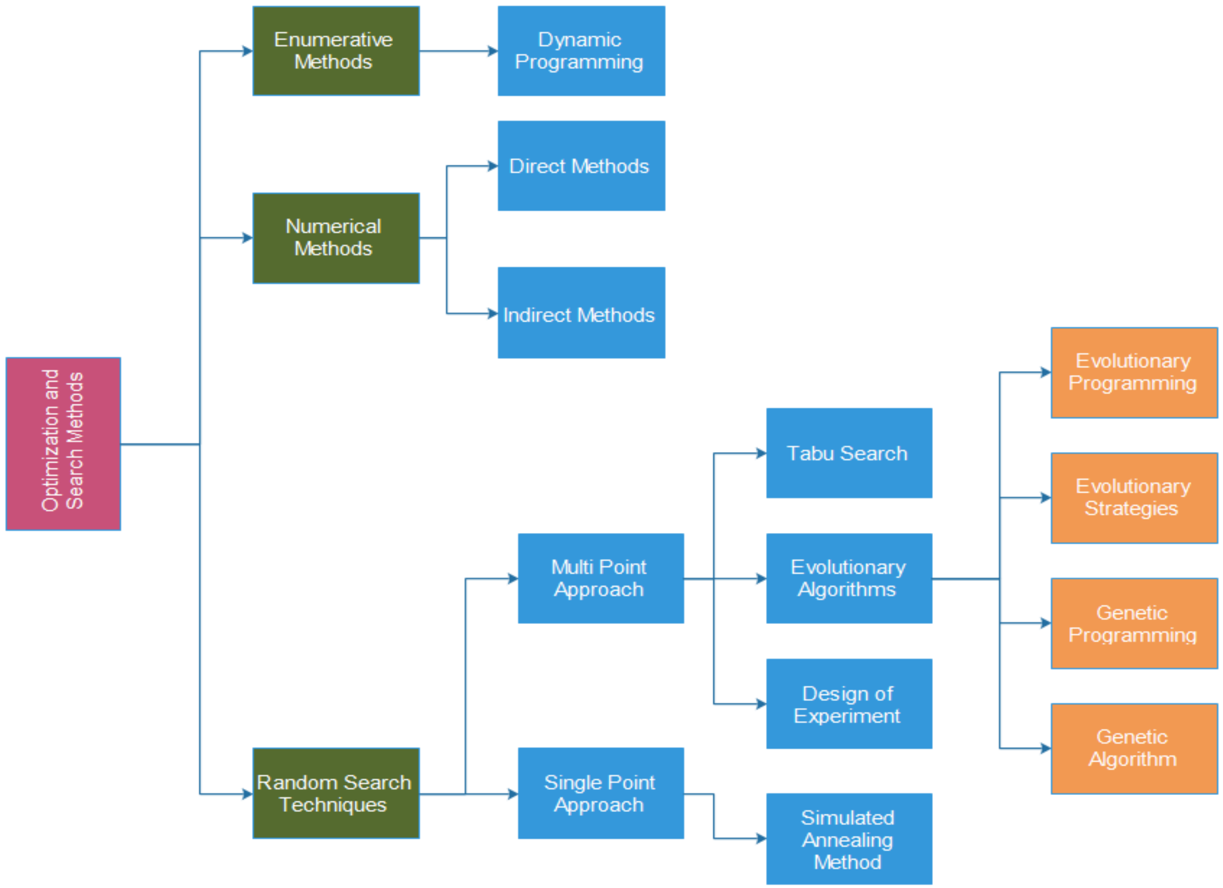

Figure A.1 : Optimization and Search Techniques.

APPENDIX B

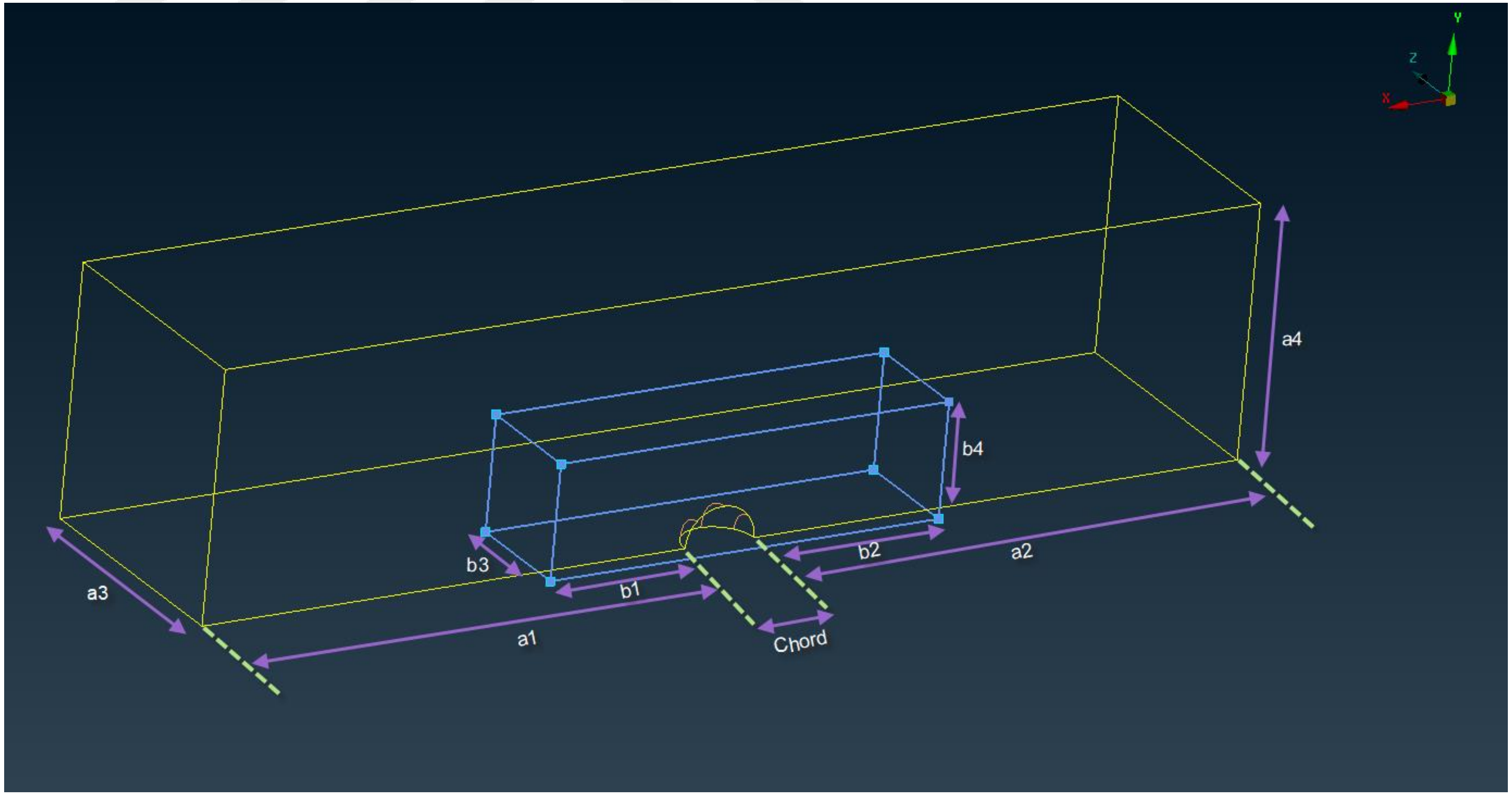

Figure B.1 : Edge Enumeration of Solution Domain (ANSA).

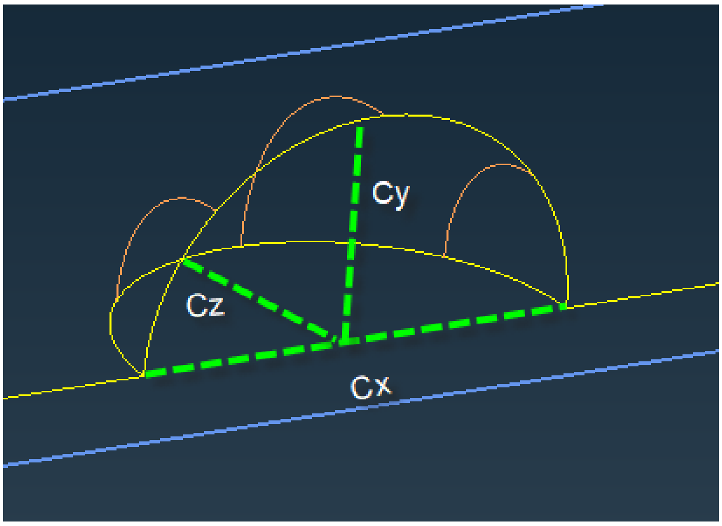

Figure B.2 : Representation of Radome Specific Dimensions (ANSA).

APPENDIX C

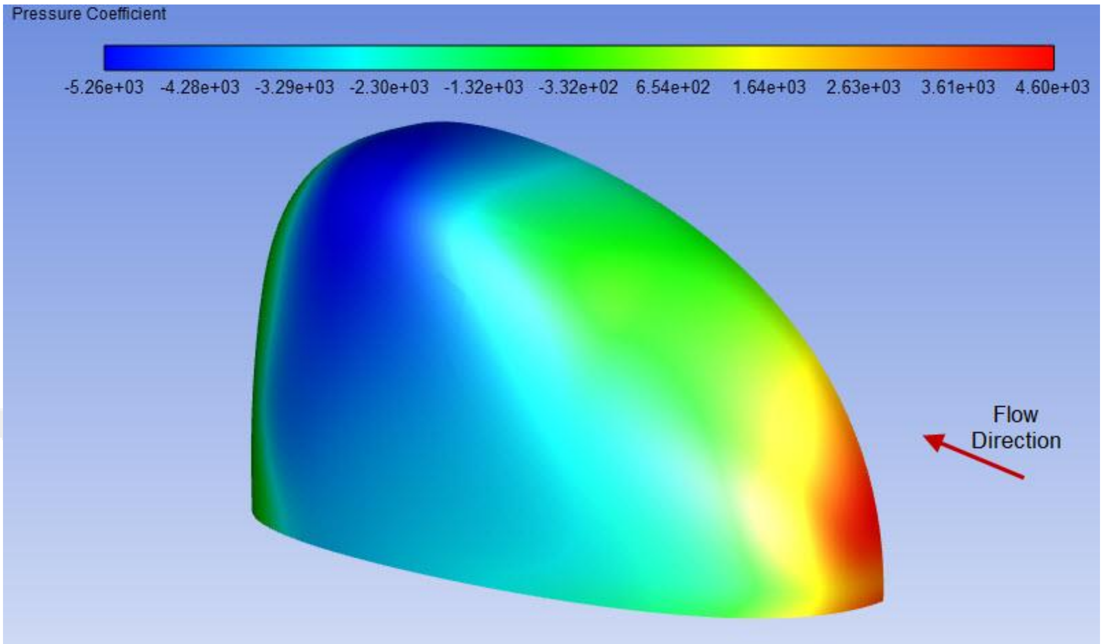

Figure C.1 : L & D Minimization Case #2, Pressure Coefficient (Isometric-Front).

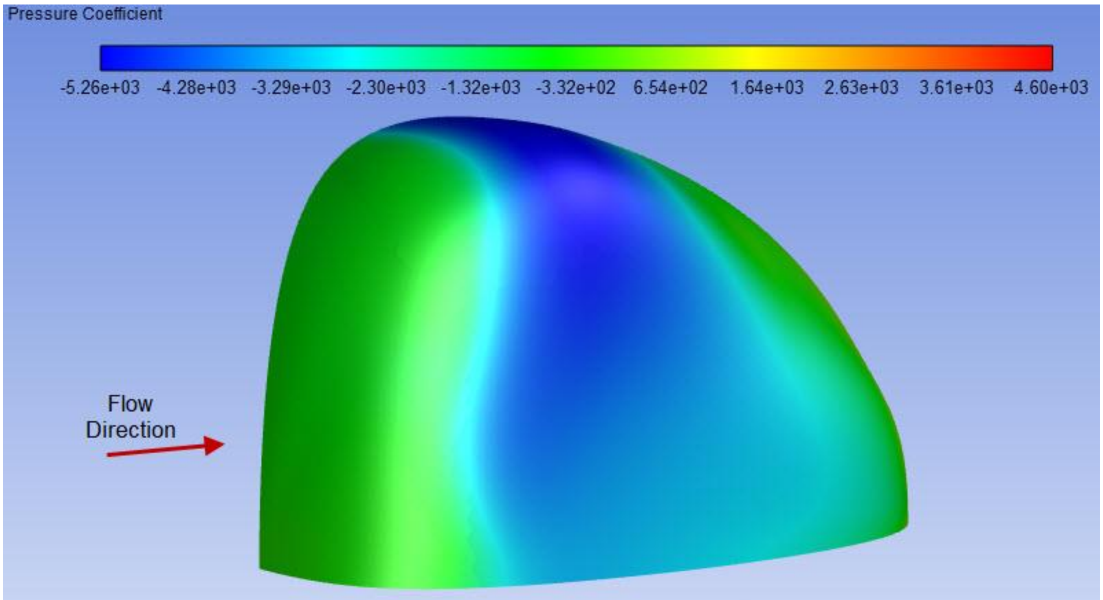

Figure C.2 : L & D Minimization Case #2, Pressure Coefficient (Isometric-Aft).

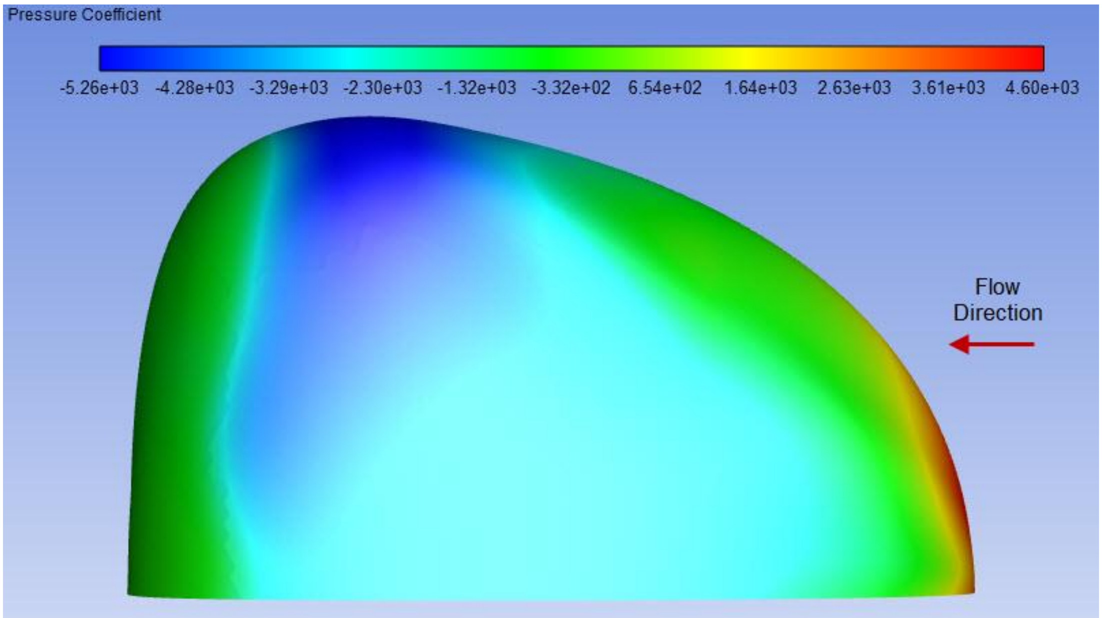

Figure C.3 : L & D Minimization Case #2, Pressure Coefficient (Side).

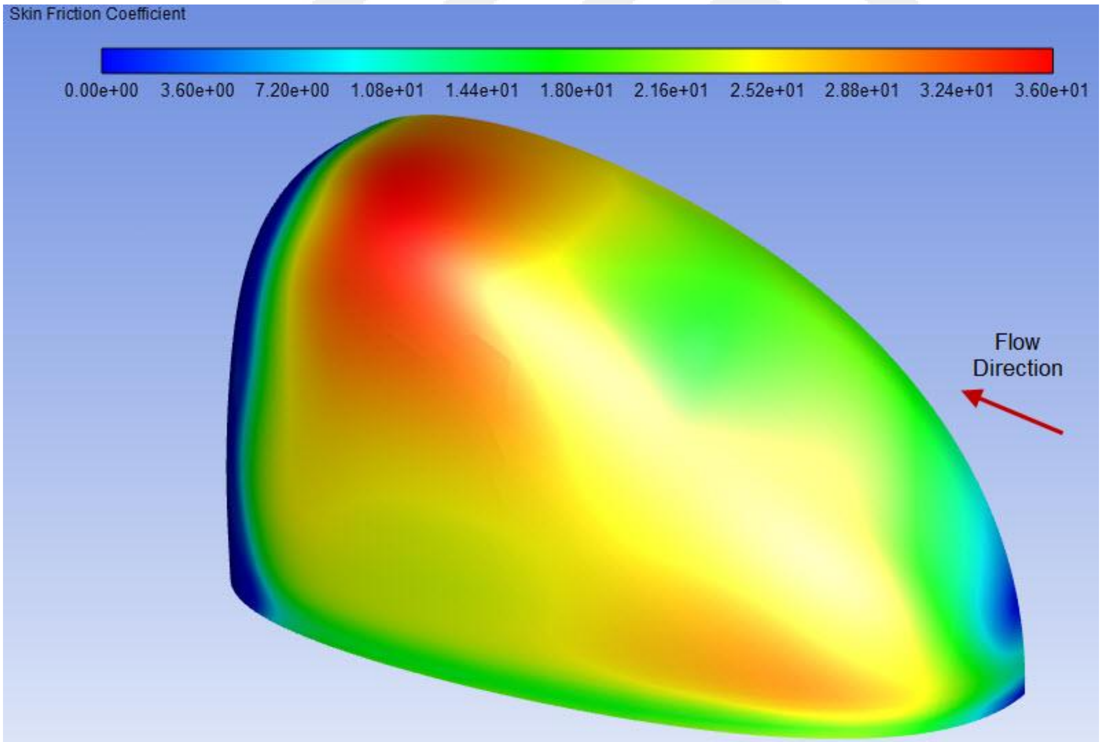

Figure C.4 : L & D Minimization Case #2, Skin Friction (Isometric-Front).

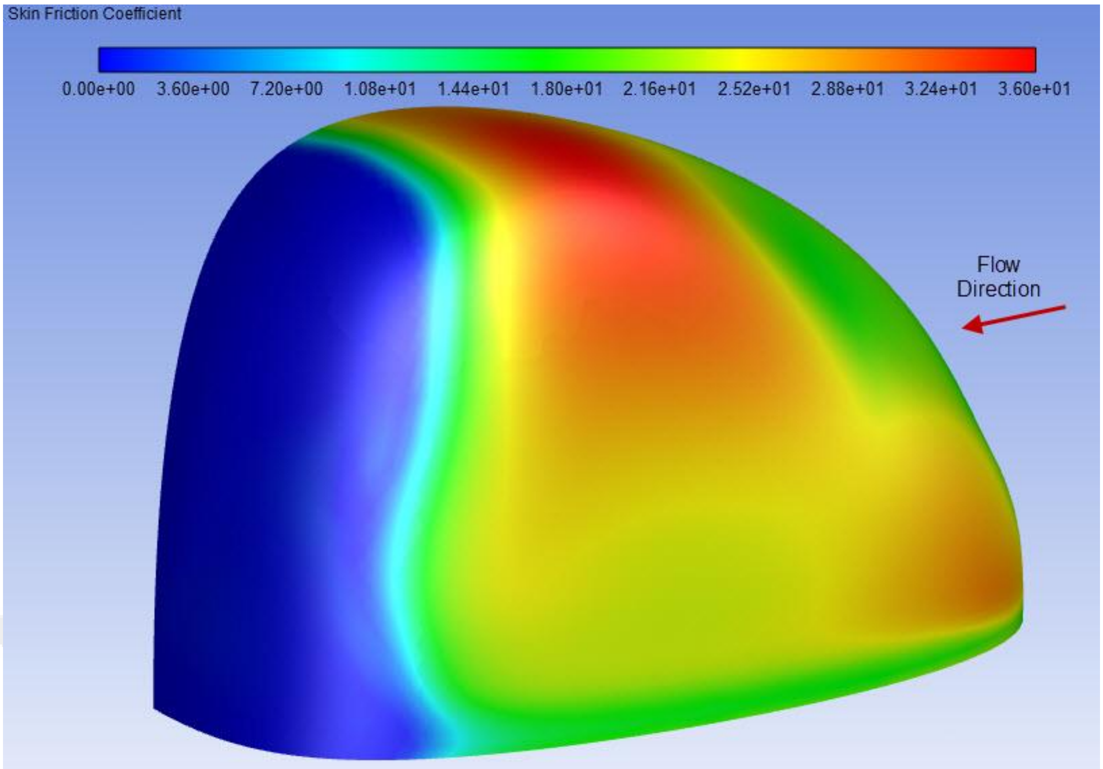

Figure C.5 : L & D Minimization Case #2, Skin Friction (Isometric-Aft).

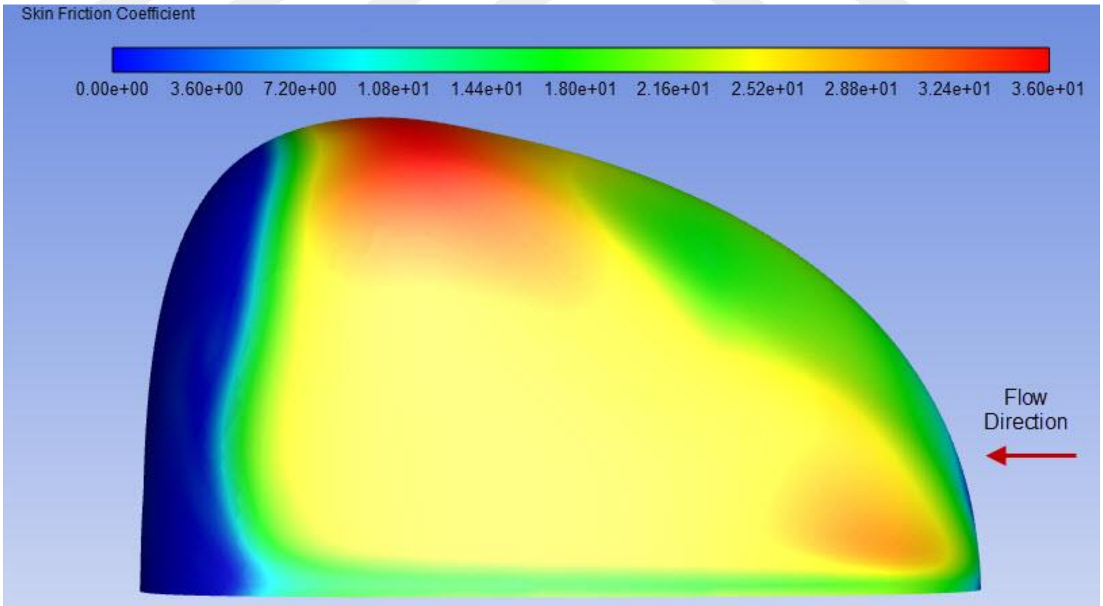

Figure C.6 : L & D Minimization Case #2, Skin Friction (Side).

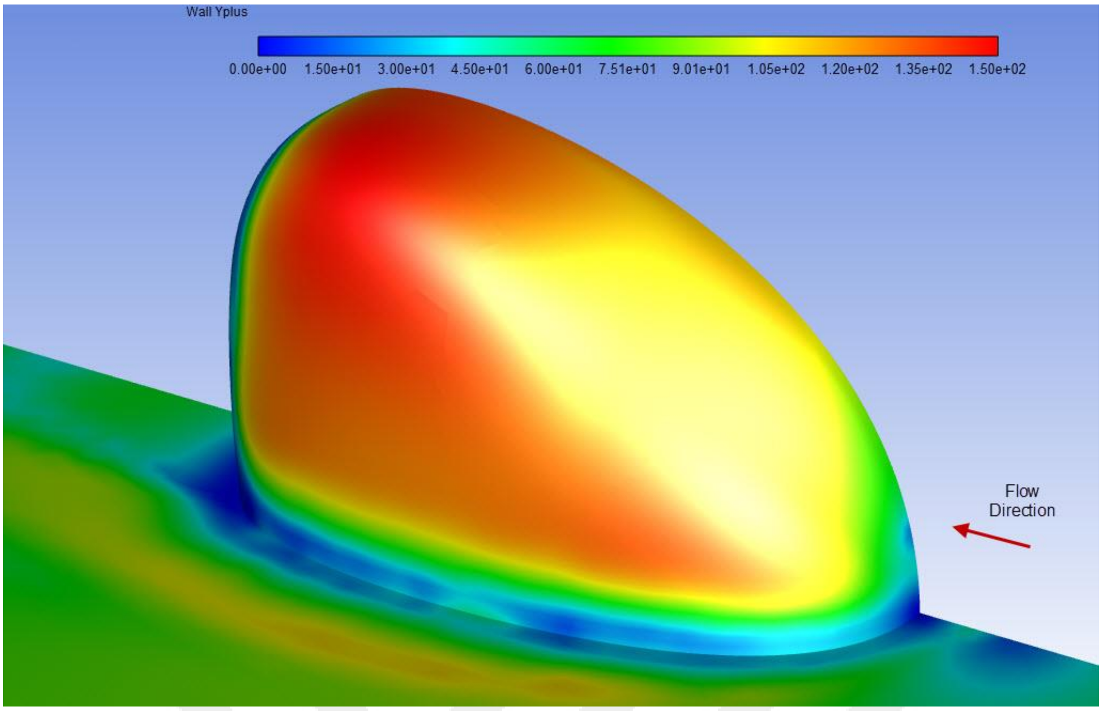

Figure C.7 : L & D Minimization Case #2, Wall y^+ (Isometric-Front).

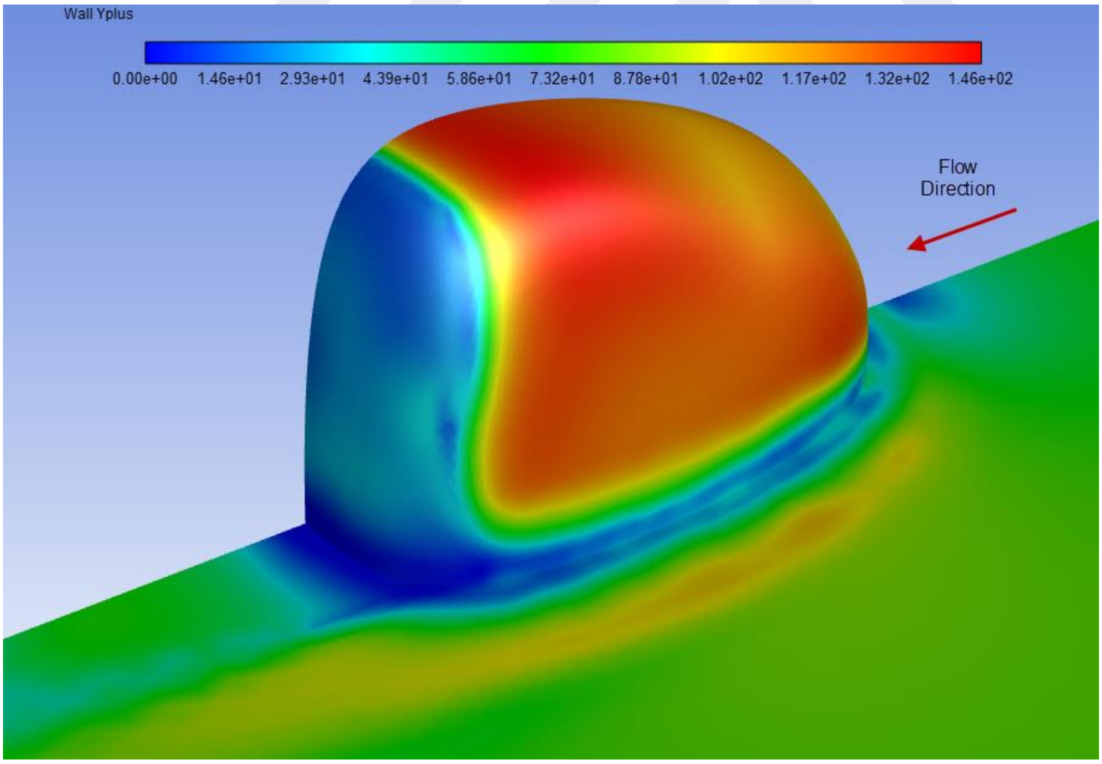

Figure C.8 : L & D Minimization Case #2, Wall y^+ (Isometric-Aft).

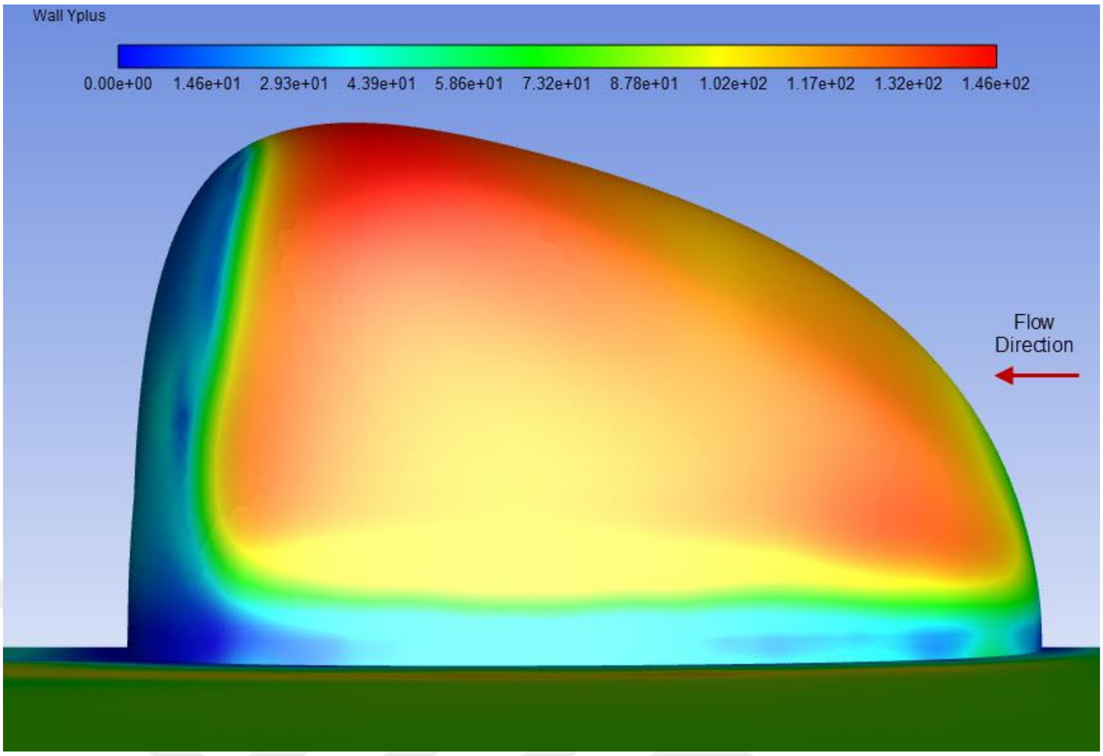

Figure C.9 : L & D Minimization Case #2, Wall y^+ (Side).

CURRICULUM VITAE

Name Surname : İlhanberk DAYLAN

Place and Date of Birth : Bursa/TURKEY 09.05.1994

E-Mail : ilhanberk94@hotmail.com

EDUCATION :

- **B.Sc.** : 2016, Istanbul Technical University, Aeronautical and Astronautical Engineering Faculty, Aeronautical Engineering Department

PROFESSIONAL EXPERIENCE AND REWARDS:

- 2016-2020 ASELSAN